# 論文要旨

近年の光ネットワークの消費電力の増加に伴い，ネットワークの省電力化が求められている．究極的に省電力な光ネットワークを実現するためには，光信号の 1bit を生成するのに必要な光子数を極限まで減らせば良い．また，少数な光子を信号として用いることのできる光ネットワークにおいては，量子暗号通信を初めとする光子の量子的な性質を応用した通信技術を利用することができるという新たなメリットも生じる．しかしながら現状の光ネットワークでは，光信号をスイッチする際に電気的な処理を介しているため，エネルギー的に非効率であると同時に量子的な情報が失われてしまう．このような背景から，電気的な処理を介さない低損失な光スイッチの実現を本研究の目的とした．

第 1 章では，現在までに提案されている光スイッチについて概観した後，微小光共振器を用いた光スイッチの優位性について説明する．その後，微小光共振器を用いた幾つかのスイッチと比較することにより，シリカトロイド微小光共振器をスイッチとして用いることの意義について強調する．

第 2 章では，本研究で用いるシリカトロイド微小光共振器について概観する．特に，作製法，共振器内の電磁界分布，内部で生じる非線形光学効果について説明する．

第 3 章では，シリカトロイド微小光共振器への光結合について説明する．本研究で用いたテーパファイバを用いる手法に着目し，実験データも踏まえながら光結合の方法について定量的/定性的な理解を与える．

第 4 章では，Side-couple 系における光スイッチの実験結果を示す．適切な時間幅を持ったポンプ光パルスを入力することにより，光 Kerr 効果のみを選択的に利用し，高速な光スイッチを実現した．

第 5 章では，Add-drop 系における光スイッチの実験結果を示す．曲げテーパファイバを用いた新たな Add-drop 系を構築することにより，光 Kerr 効果による経路切り替えスイッチを実現することに成功した．

第 6 章にて，本論文を総括し，結論及び今後の展望を述べる．

# Thesis Abstract

Considering the recent increase of power consumption in the optical network, it is required to make the network energy-efficient. For achieving “ultimate” energy efficiency, the number of photons which is required for generating optical one bit should be reduced to few-photons-level. In addition, under the optical network with few-photons, it can be expected that technology based on quantum nature of photons (e.g. quantum cryptography) can be employed. However, the electrical process is included in the optical switching in the current optical network; it is not energy-efficient and dissipates the quantum information of photons. Considering this problem, the objective of this study is to achieve optical switch which doesn’t contain any electrical processes and has extremely low loss.

In chapter 1, previously reported optical switches are over-viewed and the superiority of optical microcavity-based switch is explained. Then, the significance of silica toroid microcavity-based optical switch is clarified by comparing it with other microcavity-based switches.

In chapter 2, I provide brief introduction of a silica toroid microcavity, which is used in this study. Especially, I focus on the fabrication process, the distribution of whispering gallery modes in the cavity and the nonlinear optical effect in the cavity.

In chapter 3, coupling the light into a silica toroid microcavity is explained. In this chapter, I concentrate on the coupling method using an optical taper fiber and describe how to couple light into a silica toroid microcavity while showing the experimental data.

In chapter 4, the results of optical Kerr switch with a side-coupled system is shown. Thanks to the optimization of the pump pulse duration, I could selectively take advantage of Kerr effect and achieve fast optical switching operation.

In chapter 5, I show the results of optical switch with an add-drop system. By developing a novel add-drop system based on a bent optical taper fiber, I could observe the optical path switching induced by Kerr effect.

Finally, I summarize this thesis and mention the conclusion and the future outlook of this study in chapter 6.

# Contents


**1 Introduction** **9**
- 1.1 Motivation . . . 9
  - 1.1.1 Current optical telecommunication . . . 9
  - 1.1.2 Toward few-photons-based optical telecommunication . . . 10
  - 1.1.3 Directions . . . 11
- 1.2 Optical switches . . . 11
  - 1.2.1 Definition of optical switch . . . 11
  - 1.2.2 Category of optical switches . . . 11
  - 1.2.3 Categorization based on "principle" . . . 11
  - 1.2.4 Categorization based on "material" . . . 13
  - 1.2.5 Requirements for optical switches . . . 14
- 1.3 Microcavity-based optical switches . . . 14
  - 1.3.1 Optical microcavities . . . 14
  - 1.3.2 Principle of optical microcavity-based switch . . . 17
  - 1.3.3 Various optical microcavity-based switches . . . 20
- 1.4 Position of this study . . . 21
  - 1.4.1 Previous studies . . . 22
  - 1.4.2 Objective of this study . . . 23
- 1.5 Chapter overview . . . 27

**2 Silica toroid microcavity** **29**
- 2.1 Fabrication . . . 29
- 2.2 WGM modes in a silica toroid microcavity . . . 30
  - 2.2.1 WG modes in a microsphere cavity . . . 31
  - 2.2.2 WG modes in toroid microcavity . . . 35
- 2.3 Nonlinear refractive index change in a silica toroid microcavity . . . 37

**3 Coupling light into an optical microcavity** **41**
- 3.1 Coupled mode theory . . . 41
  - 3.1.1 Side-coupled system . . . 42
  - 3.1.2 Add-drop system . . . 44
- 3.2 Method to couple light into WGM cavity . . . 46
- 3.3 Fabrication of taper fiber . . . 49
- 3.4 Measurement of a silica toroid microcavity . . . 50
  - 3.4.1 Measurement system . . . 50

3.4.2 Characterization of $Q$ factor . . . 51
3.4.3 Optimization of coupling . . . 53

**4 Optical Kerr switch in a side-coupled system 57**
4.1 Principle of microcavity-based switch - "two-wavelength" scheme . . . 57
4.1.1 Qualitative understanding . . . 57
4.1.2 Quantitative understanding . . . 58
4.2 Optical TO switch . . . 61
4.2.1 Experimental setup . . . 61
4.2.2 Switching operation . . . 62
4.3 Optical Kerr switch . . . 64
4.3.1 Observation of Kerr effect . . . 64
4.3.2 Switching operation . . . 66
4.3.3 Discussions . . . 69
4.4 Summary . . . 74

**5 Optical Kerr switch in an add-drop system 75**
5.1 Development of an add-drop system . . . 75
5.1.1 Design and strategy . . . 75
5.1.2 Fabrication of a bent taper fiber . . . 77
5.1.3 Development of stage system for a drop fiber . . . 79
5.2 Switching operation in an add-drop system . . . 80
5.2.1 Signal transmission of an add-drop system . . . 80
5.2.2 Switching operation in an add-drop system . . . 83
5.3 Summary . . . 86

**6 Conclusion 87**

**A Equipments and instruments used for experiments 89**

**B Calculation model of optical Kerr switch 91**

**C Optomechanically-induced oscillation 93**

**D Experimental estimation of an absorption coefficient 97**

# Chapter 1

# Introduction

In this chapter, the motivation and position of this study is shown. First, the need of optical switch is explained by clarifying the problem in the current optical network and by discussing the perspective for the future optical network. Next, the key technology "optical microcavity" of this paper is described and optical switches based on various optical microcavities are introduced. Then the position of my study is is explained by analyzing previous studies, and finally the objective is shown.

## 1.1 Motivation

### 1.1.1 Current optical telecommunication

To the present, telecommunication technologies brought huge benefit to us. Particular, internet-related technologies gave a great impact on our lives, and internet is now considered as one of the "necessities" in our daily lives. However, current telecommunication network will face (are facing) severe "energy" problem.

In the early days in 21st century, internet network was used to exchange information mainly composed of "text" data. In general, text-based information is limited, so the network can deal them without any problems. However, recent network exchanges not only text-based information but also multimedia data such as pictures, sounds and movies, sizes of which are much larger than text-based data. In addition, the number of internet users has been drastically increased. The number of internet user in Japan was 56 million in 2001, but it increased to 96 million in 2011.[1] Due to these two reasons, the internet traffic has been explosively increased, and hence a large power consumption related to telecommunication network are becoming a serious problem. For example, according to R. S. Tucker,[2] the power consumption in telecommunication network will continue to increase and it will reach 10% of the total power consumption of the world. So, power consumption problem in telecommunication network is severe that we will face in the future.

One of the reasons why telecommunication network consumes a large amount of power is that it consists of a lot of inefficient optical/electrical/optical (OEO) conver-

sions[*a] in the network nodes. Core network is currently composed of optical fibers and network nodes. Optical fiber transmit optical signals between network nodes, and the network node distributes optical signal form optical fiber to the another optical fibers. Optical fiber is an ideal medium which has very small propagating loss,[3] so we can obtain energy-efficient telecommunication network if we can have energy-efficient network nodes. However, in reality, there are too many inefficient OEO converters in a network node. In general, OEO conversion is not energy-efficient and use of electrical signal in electrical circuit generates Joule heat, which is usually regarded as power loss. So, the existence of OEO converters in network nodes is one of the main causes of large power consumption in telecommunication network. Taking the discussion into consideration, we can solve the power consumption problems in telecommunication network if we have "all-optical" telecommunication network where there is no OEO converters.

### 1.1.2 Toward few-photons-based optical telecommunication

In the previous section, the benefit of an all-optical network was described in terms of reduction of power loss due to OEO convertor and Joule heat. However, I believe that an ultimate goal of the all-optical telecommunication is not limited to eliminate OEO converters; it is "a few-photons-based" optical telecommunication. In the current optical telecommunication, "bunch of photons" is employed as one bit of optical signal. This means that large energy corresponding to bunch of photons is necessary for generating an optical bit. On the other hand, if we can use "few photons" as a bit of optical signal, we can generate a optical bit with a ultimately small energy corresponding to few photons. This means that ultimately energy-efficiency is obtained in a few-photons-based optical telecommunication. Therefore, I believe that the ultimate goal of the all-optical telecommunication is a construction of a few-photons-based optical telecommunication.

In addition, a few-photons-based optical telecommunication can give us additional benefits; the ability to utilize quantum nature of photons. It is well-known that optical signal, whose energy is a few-photons level, behaves not only like a "wave" but also like a "particle." This means that we must treat it as "quantum optics" light. A Japanese research group showed that theoretical limitation of classical telecommunication capacity could be exceeded by taking advantage of quantum nature of photons.[4] In addition, such as quantum cryptography,[5] which ensures perfect security of telecommunication, and quantum computing,[6] which provides ultrafast parallel computation, are intensively studied as quantum optics. Therefore, if a few-photons-based optical telecommunication is implemented, we can utilize these quantum applications in addition to the ultimate energy-efficiency.

A few-photons-based optical telecommunication will bring a lot of benefits to us. However, it should be noted that a few-photons-based telecommunication is still in labs[*b].

[*a] In the present, we do not have technologies to switch light signal at network nodes. Thus, optical signal is temporarily converted into electric signal, and then is switched. After switching process, electric signal is reconverted into light signal. This is OEO conversion process.

[*b] On the other hand, as for quantum cryptography, field trials are now being conducted.[7] Thus it might not be far from practical use.

So, our mission is to explore such fundamental but important studies and paves the way to the realization of practical quantum network.

### 1.1.3 Directions

As mentioned in the previous two subsections, all-optical telecommunication is very important. Therefore, many researchers have studied "all-optical" network nodes which include no OEO conversion. It is well-known that various optical components such as optical switches, optical memories (buffers), optical labeling system the building blocks for constructing all-optical nodes. Of these, optical switch is the key to build all-optical network node and has been intensively studied by researchers all over the world. Hence, in this study I focus on an optical switch. In the following, I survey optical switches which have been proposed to the date, and systematically categorize them as to "physics" and "material."

## 1.2 Optical switches

Until today many kinds of optical switches have been proposed. To show the progress of this research field, I categorize the switches in terms of physics and material.

### 1.2.1 Definition of optical switch

Before starting the categorization, I define the term "optical switch." Figure 1.1 shows the schematic of optical switch. I define "optical switch" as a device that turns the probe ON and OFF by applying "external modulation" as shown in Fig. 1.1. Optical switch must be able to switch probe light without converting it into electric signal. On the other hand, we can use "control" light, carrier injection, electric field, heat flow or something else as an external modulation; external modulation is not limited to the light in contrast to the probe light. This is the definition of the "optical switch" I use in this thesis.

### 1.2.2 Category of optical switches

As mentioned above, optical switch is a vital component to construct all-optical node (router), thus, many researchers proposed various kinds of optical switches in the past. Configurations of them are in various way and this makes it difficult to categorize optical switches. Here I focus on "physics" (what type of physics/principle is used) and "material" (what material is used). Figure. 1.2 shows the category of various optical switches. The horizontal and vertical axes represent the principle and material, respectively. In the next subsection, I explain briefly on each.

### 1.2.3 Categorization based on "principle"

"Principle" class can be divided into four category such as gain & absorption modulation, wavelength conversion, refractive index modulation and mechanical motion as shown in

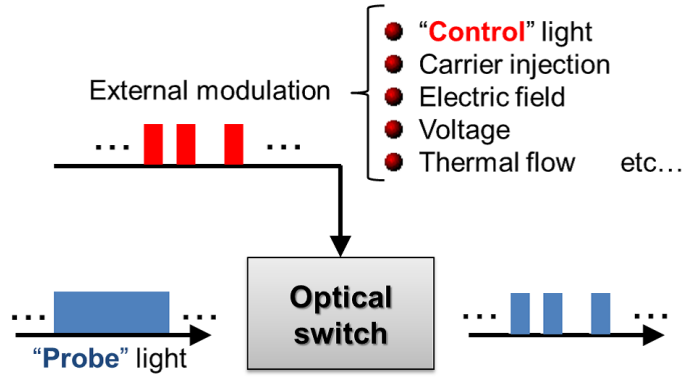


Fig. 1.1: Definition of an optical switch that is used in this thesis.

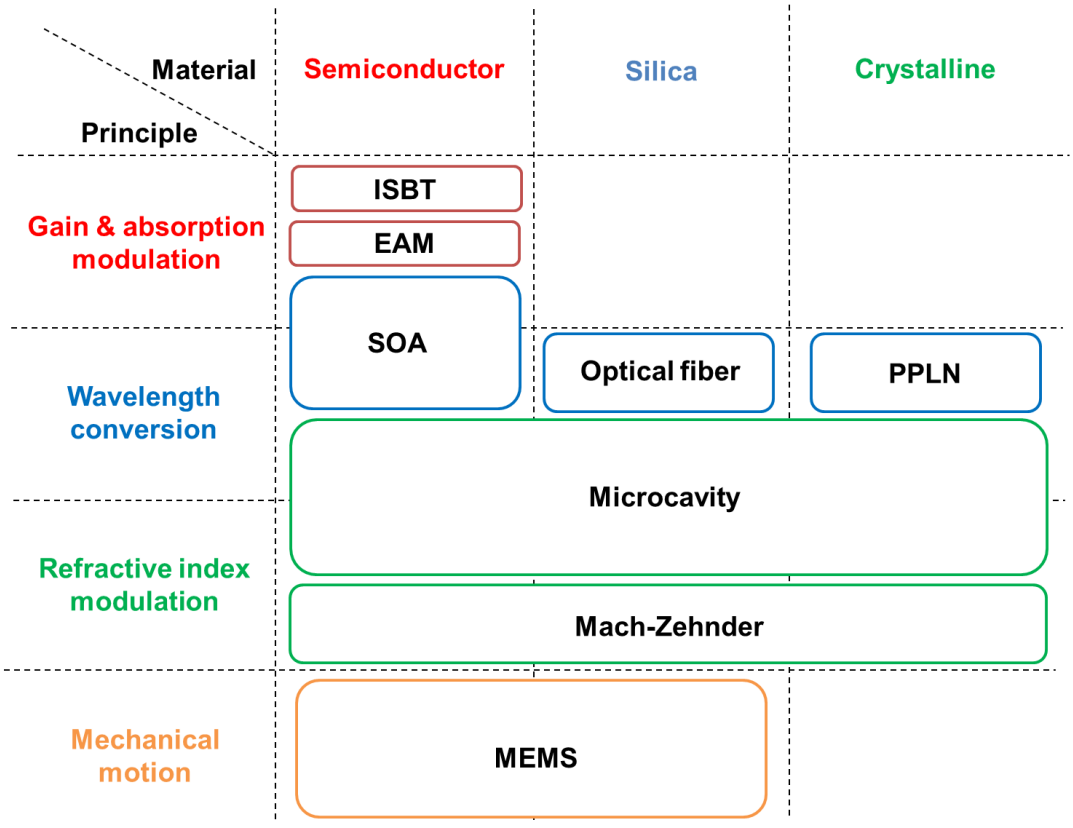


Fig. 1.2: Category of various optical switches.

the vertical axis in Fig. 1.2.

"Gain & absorption modulation" category includes, for example, intersubband transition (ISBT) switch,[8] electro-absorption modulation (EAM) switch[9] and semiconductor optical amplifier (SOA) switch using cross gain modulation (XGM).[10] In this category, absorption or gain for signal light is modulated by control light via a gain saturation of SOA (i.e. XGM) or electro-absorption effect (i.e. EAM). When gain is large (or absorption is small), the probe light can transmit optical signal ("ON"). On the other hand, when gain is small (or absorption is large), the probe light cannot transmit optical signal ("OFF"). This kind of switches take advantage of gain and absorption, thus it can switch the light regardless of the polarization of the input light.

"Wavelength conversion" category includes, for example, SOA switch using four wave mixing (FWM),[11] fiber-based switch,[12] and periodically poled lithium niobate (PPLN) switch.[13] In this category, nonlinear wavelength conversions (i.e. second harmonic generation (SHG), optical parametric oscillation (OPO), and FMW) are used to convert signal wavelength into an another wavelength. When control light is inputted, the wavelength of probe light is converted via above nonlinear wavelength conversion process. If a filter that passes only the converted wavelength is placed at the output of the device, the probe light can be outputted only when control light is inputted.. Hence, probe light is switched by control light.

"Refractive index change" category includes Mach-Zehnder switches[14,15] and microcavity-based switches.[16,17,18] Thermal flow, external electric field, carrier injection and "control" light induce refractive index change, are used to modulate the probe light[*c]. For example, destructive or constructive interference of signals between the upper and the lower arms is changed in Mach-Zehnder switch depending on the relative phase between two signals. This relative phase depends on the refractive index of the arms, thus, switching is controlled by changing the refractive index of the arms.

"Mechanical motion" class contains, for example, micro electro mechanical systems (MEMS) switches.[19] In this scheme, optical path is mechanically controlled due to, for example, the motion of mirror. The advantage of this kind of switches is the scalability. In fact, large scale matrix switch was demonstrated by using this scheme. On the other hand, fabrication of this kind of switches are difficult because structure is often complex. In addition, switching speed of them is not fast in general because they require mechanical motion to switch light. Mechanical motion is usually controlled by external voltage.

### 1.2.4 Categorization based on "material"

I divide "Material" into three categories such as semiconductor (e.g. Si, GaAs, and InGaAsP), silica ($SiO_2$) and crystalline (e.g. $CaF_2$, $Al_2O_3$, and $LiNbO_3$).

Semiconductor is highly nonlinear and it allows CMOS-compatible fabrication process. In comparison with other materials, for instance, Si has large nonlinearity.[20] Hence we can achieve switching operation with relatively low input power in semiconductor. In addition, we have sophisticated fabrication process of semiconductors thanks to progress of COMS technology, so optical switches in this category is easily and inexpensively

[*c] These will be explained later.

fabricated unlike those made of other materials. These characteristics of semiconductor have attracted many researchers, and a lot of different kinds of optical switches were proposed with semiconductor to the present.[16,17,11,21]

Silica is well-known as the material of optical fiber. Optical fiber has extremely low propagating loss of 0.2 dB/km[3,22] thus silica is regarded as a prominent platform for loss-sensitive applications for example quantum information processing.[23,24,25] Therefore, by utilizing this extremely low loss nature, we can build "transparent"(having negligible loss) optical switches. In addition, silica ($SiO_2$) has high compatibility with Si because it can be easily fabricated on Si by thermal oxidation. Such characteristics allow silica-based optical switches have a potential to be integrated on a Si chip.

At the same time crystalline material is regarded as extremely low propagating loss material. According to Savchenko *et al.*,[22] $CaF_2$ has 50 times smaller loss than silica. In addition to this extremely low loss nature, some crystalline materials have finite second-order electric susceptibility $\chi^{(2)}$ because they have no rotational symmetry in their crystal structure.[26] $\chi^{(2)}$-based nonlinearlity is known as the origin of second harmonic generation (SHG), electro-optic (EO) effect, sum-frequency generation and so on. $\chi^{(2)}$ in crystalline material is much larger than $\chi^{(3)}$ that is present in all materials, thus we can utilize nonlinearity more efficiently by using $\chi^{(2)}$ than $\chi^{(3)}$.

### 1.2.5 Requirements for optical switches

As described above, there are many different kinds of optical switches. By taking this situation into account, the question here is "which optical switches should be used." There are many requirements for optical switch such as low switching energy, low insertion loss, high switching speed, and small foot print. Of these, I focus especially on "low switching energy" and "low insertion loss."The former is a required characteristic to reduce the energy consumption of telecommunication network, which is the motivation of this study. In addition, the latter is the key for dealing with a few-photons because photons are very sensitive to loss.

To satisfy the former point, microcavity[27]-based optical switches are attractive because the light density is enhanced in optical microcavity. Thanks to this characteristic, switching operation can be achieved with small input control power in the microcavity. Considering this point, optical microcavity-based switch is introduced in the next section. We will discuss the method lowering insertion loss later.

## 1.3 Microcavity-based optical switches

### 1.3.1 Optical microcavities

Optical microcavity[27] is a micro-size container which can cage photons. To the present various optical microcavities have been proposed. Of these, the most popular optical cavity[*d] is the Fabry-Perot cavity, thus the basics of optical cavity is explained with a

[*d] "optical micro cavity" and "optical cavity" have almost the same functions and meanings. The difference between them is just the size.

Fabry-Perot cavity.

### Photon lifetime

Fabry-Perot cavity is composed of two mirrors as shown in Fig. 1.3(a). The light inputted through the left mirror reflects at the right mirrors and go backward and forward again and again. As a result, the light is captured and confined in this Fabry-Perot cavity.

However, of course, light cannot be captured in the cavity forever. Due to the losses originating from the imperfection of mirror surface and the absorption of medium with which the cavity is filled, the light intensity in the cavity gradually decays. Light intensity can be written by a very simple differential equation, given as,

$$\frac{\mathrm{d}I(t)}{\mathrm{d}t} = -\alpha I(t), \tag{1.1}$$

where $I$ and $\alpha$ are the light intensity in the cavity and decaying rate in the cavity, respectively. The solution of Eq. (1.1) is simply obtained, as,

$$I(t) = I_0 \exp(-\alpha t) = I_0 \exp(-t/\tau_{\mathrm{load}}), \tag{1.2}$$

where $I_0$ and $\tau_{\mathrm{load}} = 1/\alpha$ are the light intensity at $t = 0$ and the loaded photon lifetime. It is clear that photon lifetime gives the time until the intensity $I(t)$ become $I_0/e$. Therefore $\tau_{\mathrm{load}}$ can be used as an indicator that how long time the light is captured inside the cavity. This value is very important for evaluating the performance of the cavity.

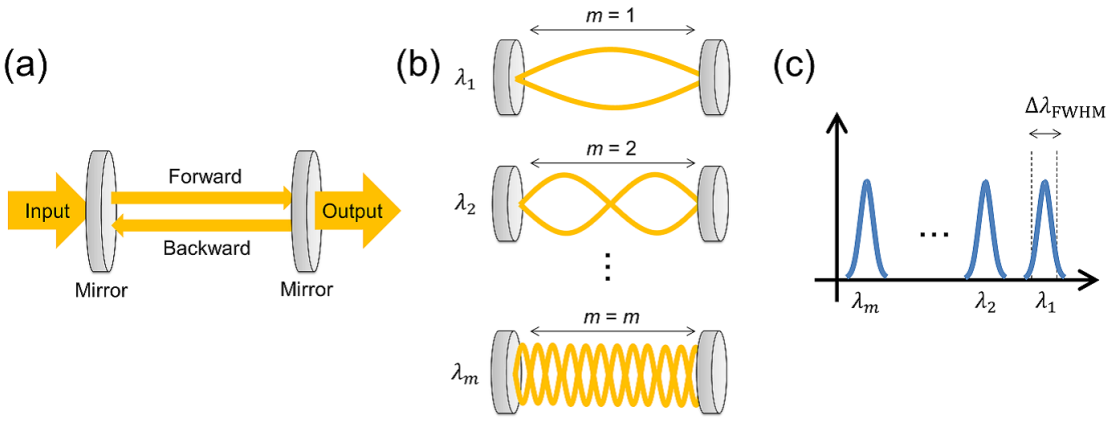


Fig. 1.3: (a) Schematic illustration of Fabry-Perot cavity. (b) Modes excited in a Fabry-Perot cavity. $m$ indicates an integer mode number. (c) Schematic illustration of resonant spectra of a Fabry-Perot cavity.

### Resonant characteristic

As discussed previously, an optical cavity is regarded as a container that can confine the light. However, this understanding is not enough to completely understand an optical cavity. The nature of resonance of an optical microcavity must be considered.

The light inside a cavity go backward and forward by being reflected on the mirrors. If backward and forward pathways of the light are identical, light interferes each other. In the situation where phase are aligned between pathways, "resonance" occurs and the constructive interference is generated. To achieve this situation, the equation below has to be satisfied;

$$m\lambda_m = 2nL, \tag{1.3}$$

where $\lambda_m$, $n$, $L$ and $m$ are the resonant wavelength, refractive index, the cavity length (distance between two mirror) and a mode number (integer), respectively. Equation (1.3) shows an optical path length of a cavity $2nL$ has to be equal to $m\lambda_m$ (Fig. 1.3(b)) to obtain the resonance. If Eq. (1.3) is not satisfied, destructive interference occur and the light cannot in the cavity. Therefore, the transmission spectra of the Fabry-Perot cavity is obtained as Fig. 1.3(c), where only the wavelength that is equal to the resonance can transmit. Quantitatively, the transmittance $Tr_{\mathrm{Fabry}}$ is written, as,

$$Tr_{\mathrm{Fabry}}(\lambda) = \frac{(1-R)^2 G}{(1-GR)^2 + 4GR\sin^2(\delta/2)}, \tag{1.4}$$

$$G = \exp(-\alpha L), \qquad \delta = \frac{4\pi n L}{\lambda}, \tag{1.5}$$

where $R$ is the power reflectance of the mirrors.

### Quality factor

Here, quality factor $Q$, which is one of the most important measures of an optical cavity, is defined. Quality factor shows the strength and the duration of light can be confined in the cavity. In general, $Q$ is defined as

$$Q = \omega_0 \times \frac{\text{Stored light energy [J]}}{\text{Output power [W]}}, \tag{1.6}$$

where $\omega_0$ is the angular frequency of the light in the cavity. On the other hand, quality factor $Q$ is written in other expressions by using $\tau_{\mathrm{load}}$ and $\Delta\lambda_{\mathrm{FWHM}}$, as

$$Q = \omega_0 \tau_{\mathrm{load}} \tag{1.7}$$

$$Q = \frac{\lambda_0}{\Delta\lambda_{\mathrm{FWHM}}}. \tag{1.8}$$

Higher-$Q$ is preferred in most of applications of optical cavity,. For example, we can have very narrow bandpass filters[28] by using high-$Q$ cavity according to Eq. (1.8). In addition, according to Eq. (1.6), if we have high-$Q$ cavity we obtain large energy in the cavity with small input power. This is advantageous for achieving energy-efficient optical switches,[16] as well as optical memories,[29] lasers.[30,31,32] And this is the reason why the optical microcavity-based switches are superior to other optical switches in terms of energy-efficiency.

Table. 1.1: The comparison between various optical switches. Reprinted with permission from [K. Nozaki, T. Tanabe, A. Shinya, S. Matsuo, T. Sato, H. Taniyama, and M. Notomi, "Sub-femtojoule all-optical switching using a photonic-crystal nanocavity," Nat. Photonics **4**, 477-483 (2010)]. ©2010, Nature Publishing Group.

| Device | Switching energy (fJ) | Switching frequency (Gbps) | Size (um$^3$) |
|---|---|---|---|
| FWM waveguide | 1070 | >1000 | 550 |
| ISBT waveguide | 6800 | >1000 | 240 |
| Mach-Zhender | 100 | 70 | 45 |
| PhC cavity-based switch | 0.42 | 20 – 40 | 0.025 |

### Energy required for microcavity-based switch

As described previously, optical microcavity-based switch is superior to other switches in terms of energy-efficiency. The comparison between various switches is shown in Table 1.1 (referred to Nozaki *et al.*[16]). Table 1.1 shows that a photonic crystal cavity based optical switch consumes much smaller energy than other optical switches[*e]. As a result, microcavity-based optical switch is extremely energy-efficient. More quantitatively, required energy for switching in microcavity-based optical switch is written as,[33]

$$U_{\text{switch}} = \frac{\varepsilon_0 \varepsilon n_0}{2n_2} \frac{V_{\text{cavity}}}{Q_{\text{load}}}, \tag{1.9}$$

where $U_{\text{switch}}$, $n_0$, $\varepsilon_0$, $\varepsilon$, $V_{\text{cavity}}$ and $Q_{\text{load}}$ are the required energy for switching, the refractive index of the medium, the permittivity in the vacuum, the relative permittivity of the vacuum, the cavity mode volume and the loaded $Q$, respectively. In this equation, $U_{\text{switch}}$ is in proportion to $V_{\text{cavity}}$ and is inversely proportional to $Q_{\text{load}}$. Thus both small $V_{\text{cavity}}$ and high $Q$ are necessary to achieve energy-efficient optical switch. Therefore optical microcavity is an excellent candidate to construct an optical switch because it has high quality factor and small size ($\mu$m).

## 1.3.2 Principle of optical microcavity-based switch

In the previous subsection, an energy-efficiency of microcavity-based switch is described. Here, I explain the basic principle of optical switch based on optical microcavity. First, I show that the shift of resonant wavelength is the key for achieving a microcavity-based switch. Next, I describe how I change the refractive index to shift resonant wavelength.

### Resonant wavelength shift

Fabry-Perot cavity has a transmission spectra as shown in Fig. 1.3(c). Figure 1.4 shows the schematic of the principle of microcavity-based optical switch. In Fig. 1.4(a), light power transmitted through an optical microcavity is high because input wavelength $\lambda_{\text{input}}$

[*e] Photonic crystal cavity is a kind of microcavities, which is described in 1.3.3

is set equally at the cavity resonant wavelength $\lambda_{\text{cavity}}$. This condition is the "ON" state of a microcavity-based optical switch. On the other hand, in Fig. 1.4(b), transmitted power is low because $\lambda_{\text{cavity}}$ is detuned far from $\lambda_{\text{input}}$. Because the output is very low, thus this situation is "OFF" state of the switch. Hence, if we can shift the cavity resonant wavelength $\lambda_{\text{cavity}}$, switching operation is achieved.

As described in Eq. (1.3), cavity resonant wavelength is in proportion to cavity length $L$ and refractive index $n$. This allows us to control the output power from the cavity. Some commercial wavelength tunable lasers use this tuning principle. They control the output wavelength by mechanically changing the cavity length $L$. However, in general, mechanical movement requires relatively long time, thus it is not suitable for an optical switch that requires very fast switching speed. Considering this fact, microcavity-based optical switches are commonly driven by changing refractive index $n$ of the optical microcavity.

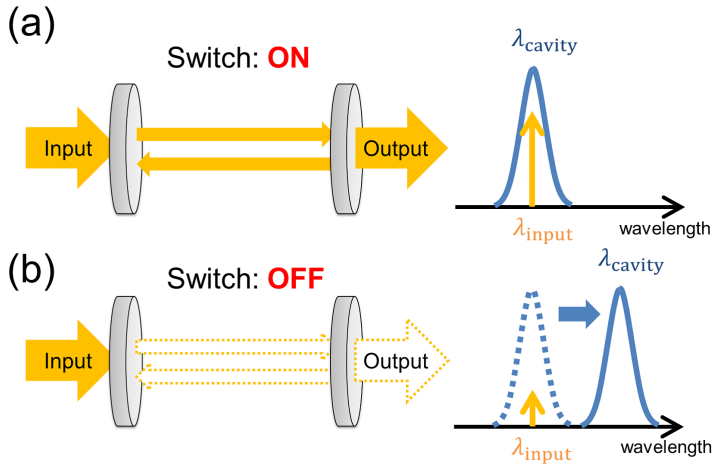


Fig. 1.4: Schematic illustration of the principle of a microcavity-based optical switch.

### Effects inducing refractive index change

To use an optical microcavity as an optical switch, a method to change the refractive index of the microcavity is necessary. For this, in general, mainly four effects which are electro-optic (EO) effect, thermo-optic (TO) effect, carrier-plasma effect and Kerr effect are used. Brief explanations about them are provided in the following.

EO effect is usually known as one of second-order nonlinear optical effect. By applying external electric field to the medium the refractive index is changed. When $LiNbO_3$ is used and an electric field $E$ is applied along the $x$ axis, refractive index change induced

by EO effect is written as,[34]

$$\begin{aligned} \Delta n_x &= -\frac{1}{2}n^3 r_{41} E \\ \Delta n_y &= \frac{1}{2}n^3 r_{41} E \\ \Delta n_z &= 0, \end{aligned} \tag{1.10}$$

where $\Delta n_i$ $(i = x, y, z)$ and $r_{41}$ are the refractive index change along each the axis and the EO coefficient of $LiNbO_3$. This effect is commonly utilized for commercial modulator in an telecommunication network. However, only the materials that have no rotational symmetry exhibit EO effect[*f]. In addition, induced refractive index change has an axial dependency. Hence, optical switches utilizing EO effect are often bulky and have complex configuration.

TO effect is based on the temperature-dependency of refractive index of the material. The refractive index change induced by TO effect is written as,[35]

$$\Delta n_{\mathrm{TO}} = n\xi\Delta T, \tag{1.11}$$

where $\Delta n_{\mathrm{TO}}$, $\xi = (1/n) \cdot (\mathrm{d}n/\mathrm{d}T)$ and $\Delta T$ are the refractive index change induced by TO effect, the TO coefficient and the temperature change, respectively. In general, the temperature of microcavity is controlled by applying heat to an external metal heater deposited near the microcavity[36] or by the absorption of the light in the cavity.[17] However TO effect-based optical switches are suffering from slow thermal diffusion time, thus fast switching time is difficult to achieve with this effect.

Carrier-plasma effect is origination from the dependency of the plasma frequency on carrier concentration of the microcavity. It is well know that permittivity of a material depends on the plasma frequency. In addition, the plasma frequency has a dependency of the carrier concentration. The permittivity (i.e. refractive index) is changed by modulating carrier concentration. The refractive index change induced by carrier plasma effect is written by the following equation:[37]

$$\Delta n_{\mathrm{carrier}} = -\frac{e^2\alpha\tau_{\mathrm{R}}}{2\varepsilon_{\mathrm{b}} n_0 m_{\mathrm{c}} \hbar\omega^3} I, \tag{1.12}$$

where $e$, $\tau_{\mathrm{R}}$, $\varepsilon_{\mathrm{b}}$, $m_{\mathrm{c}}$ and $\hbar$ are the unit charge, the carrier-hole recombination time, the contribution to the permittivity from bound change, the carrier mass and the Plank constant over $2\pi$, respectively. Carrier injection or two-photon absorption process induced by control light is generally used to increase carrier density in the microcavity, . Carrier plasma effect is usually much faster than TO effect, but its response time is limited to the carrier-hole recombination time $\tau_{\mathrm{R}}$.

Kerr effect is one of third-order nonlinear optical effects[*g]. It is well-known as the origin of self phase modulation (SPM) and cross phase modulation (XPM) in a optical fiber. The refractive index change induced by Kerr effect is given as,[38]

$$\Delta n_{\mathrm{Kerr}} = n_2 I, \tag{1.13}$$

[*f] Crystalline material such as $LiNbO_3$ and $KH_2PO_4$(KDP) are the examples which exhibit EO effect.

[*g] Kerr effect is the core of this paper, so the detailed explanation will be provided in 2.3.

where $I$ is the power density in the cavity. This effect is instantaneous thus switching speed of optical switch based on Kerr effect is much faster than other effect. In addition, Kerr effect consumes very little energy[35] because it can change the refractive index without any absorption. However, the refractive index modulation is very small,[39] thus it can be easily overwhelmed by other effects. In contrast to EO effect, Kerr effect is obtained in any material regardless of the symmetry of the crystal.

### 1.3.3 Various optical microcavity-based switches

I will describe various optical microcavities that are used for optical switch in this subsection.

#### Microring cavity

Microring cavity is the monolithic ring-shaped cavity that is fabricated on a chip as shown in Fig.1.5(a). Its simple ring shape makes the fabrication process easy and inexpensive. Thus it is widely used for various applications such as optical switch,[17,40] memory,[41,42] delay line,[43] frequency comb source,[44] spectrometer[45] and sensor.[46] In addition, due to its simple shape, this kind of cavity is fabricated on various platforms such as Si,[17] GaAs/AlGaAs,[47] $Si_3N_4$[44] and polymer.[48] To the best of my knowledge, $Q$ factor of a ring cavity is up to $7 \times 10^6$ which was recorded with $Si_3N_4$ microring.[49] However the $Q$ of this kind of cavity is in general limited by the following two factors; surface roughness originating from the fabrication and the material absorption. In addition, to avoid to the radiation loss, diameter of the ring has to be larger than few-$\mu$m.

Switching is usually induced by using carrier-plasma effect[40] and TO effect.[17] Due to the large thermal conductivity, V. Almeida *et al.*[17] demonstrated switching with time of ns in a silicon microring even though TO effect was utilized. They are fabricated on a chip, thus it is easily integrated. This is an excellent feature of the microring cavity. On the other hand, it suffered from large coupling loss between the chip and optical fibers due to the large mode mismatch and the propagation loss of the on-chip waveguide. On-chip spot converters were proposed[50,51] to reduce the coupling loss,. However, net insertion loss reached 3.5 dB, even though a spot size converter is employed.[51]

#### Photonic crystal cavity

Photonic crystal (PhC) cavity now attracts wide attention due to its physically interesting natures, for example slow light,[52] super prism effect,[53] negative refraction.[54] PhC cavity is fabricated by periodically making holes (diameter of which is around a few hundreds nm) on a semiconductor chip as shown in Fig. 1.5(b). These holes behave as "Bragg reflector", thus designed wavelength is selectively prohibited to propagate in a PhC; this wavelength band is called "photonic bandgap." The light cannot propagate if we input the light at a wavelength that is inside a photonic bandgap. PhC is used with various applications such as optical switch,[16,21] optical memory,[29] laser,[32] optical spectrometer[55] and a platform of cavity quantum electrodymanics (QED).[56]

The $Q$ factor of a PhC nanocavity exceeds $10^6$ and its mode volume is extremely small. For example, K. Nozaki *et al.*[16] reported mode volume of 0.025 $\mu m^3$. This small mode volume allows this swith to be driven with switching energy of sub-fJ. Switching in PhC cavity is generally achieved by using carrier-induced effect.[16] Thanks to its small mode volume, carriers generated by control light relax quickly, thus it can exhibit ultra fast switching time of 20 ps. However, similar to the microring cavity, PhC cavity also suffers from large coupling loss. In addition, fabrication is much more difficult than that of microring because it requires us to make large number of air-holes on a chip to fabricate PhC.

#### Whispering-gallery mode cavity

Whispering gallery mode (WGM) cavity is usually sphere- or toroidal-shaped. In such microcavities, the light propagates along its spherical surface like a sound wave that propagates along "Whispering Gallery" in St. Paul's Cathedral in London[57*h], as shown in Fig. 1.5(c). The representatives of this kind of optical microcavity are a microsphere cavity,[58,59] a silica bottle microcavity[18] and a silica toroidal microcavity.[60] These cavities are characterized having an ultimate high $Q$, which typically exceed $10^8$. This is due to smooth surface formed by thermal melting and because they are fabricated by using low-absorption material such as silica and crystalline materials. To fully take advantage of ultra high-$Q$, WGM cavity is usually employed for cavity QED,[61] optomechanics,[62] low-threshold laser,[30] frequency comb source[63] and ultra-sensitive sensor.[64]

Switching in a WGM was achieved by using Kerr effect.[18,59] Due to its ultra high-$Q$, the switching control power of 50 $\mu$W, which is the smallest switching power via Kerr effect.[18] Besides Kerr effect, EO effect was used to modulate the signal in a $LiNbO_3$ microsphere.[26] Thanks to its high $Q$ factor, nonlinear effect is efficiently induced in such cavities. On the other hand, switching speed is limited to its long photon life time, thus it is difficult to achieve fast optical switch.

## 1.4 Position of this study

In 1.3.3, I introduced various kinds of optical microcavity-based switches. As described in 1.1.2, ultimate goal of all-optical telecommunication is the realization of a few-photon-level telecommunication. Telecommunication will be ultimately energy-efficient and we will be fully utilizing quantum nature of photons. For this it is desired to use microcavity that allows easy coupling with (without coupling loss) an optical fiber and is fabricated by low-loss materials such as silica and crystals. This is because photons are very sensitive to loss. Considering the discussions above, in this section, the objective of this thesis is explained. First, I review some previous studies that satisfy the above requirements for clarifying position of my study. After that, the objective of this paper is shown and superiorities are emphasized.

[*h] This will be explained in detail in 2.2

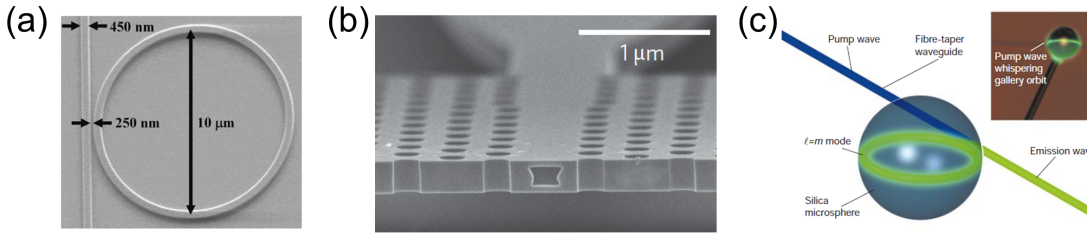


Fig. 1.5: (a) Scanning electron microscope (SEM) image of a silicon microring cavity. [Reprinted with permission from V. Almeida, C. Barrios, R. Panepucci, M. Lipson, M. Foster, D. Ouzounov, and A. Gaeta, "All-optical switching on a silicon chip," Opt. Lett. **29**, 2867-2869 (2004). ©2004, Optical Society of America.] (b) SEM image of a PhC cavity. [Reprinted with permission from K. Nozaki, A. Shinya, S. Matsuo, Y. Suzaki, T. Segawa, T. Sato, Y. Kawaguchi, R. Takahashi, and M. Notomi, "Ultralow-power all-optical RAM based on nanocavities." Nat. Photonics **6**, 248-252 (2012). ©2012, Nature Publishing Group.] (c) Schematic image of a microsphere cavity. [Reprinted with permission from K. Vahala, "Optical microcavities," Nature **424**, 839.846 (2003). ©2003, Nature Publishing Group.]

### 1.4.1 Previous studies

#### Optical Kerr switch using silica bottle microcavity

M. Pöllinger and A. Rauschenbeutel[18] demonstrated optical Kerr switch and memory using a silica bottle cavity. As shown in 1.3.3, a silica bottle microcavity (Fig. 1.6(a)) is one of the WGM cavities which has a $Q$ of over $10^8$. This microcavity is fabricated by silica, thus it has extremely low material loss. In addition, as shown in Fig. 1.6(a), this microcavity can be efficiently coupled to optical fiber. Therefore, a silica bottle microcavity satisfies the two requirements I described above. Furthermore, an add-drop configuration is demonstrated as shown in Fig. 1.6(b) where two optical fibers are coupled to a microcavity[*i].

#### Optical Kerr switch using hydrogenated amorphous silicon microcylindrical resonators

Very recently, in October 2013, N. Vukovic *et al.*[65] demonstrated an optical Kerr switch in a hydrogenated amorphous silicon (a-Si:H) microcylindrical resonator[66] as shown in Fig. 1.7(a). It is difficult to employ Kerr effect in a crystalline Si because carrier-related refractive index change generally dominates Kerr effect. However, according to the authors, a-Si:H has twice larger nonlinear refractive index $n_2$ than crystalline Si. Therefore, Kerr effect can be employed in an a-Si:H microcylindrical resonator[*j].

[*i] The theory which can describe an add-drop system will be provided in 3.1.2.

[*j] a-Si:H might be now intensively studied. Recently Kerr switching using a-Si:H microring cavity was also demonstrated.[67]

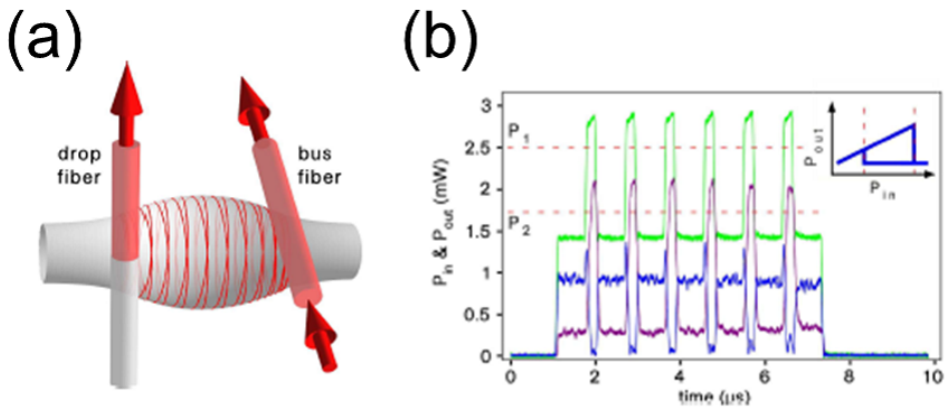


Fig. 1.6: (a) Schematic of a silica bottle microcavity and (b) optical Kerr switching operation. [Reprinted with permission from M. Pöllinger and A. Rauschenbeutel, "All-optical signal processing at ultra-low powers in bottle microresonators using the Kerr effect," Opt. Express **18**, 17764-17775 (2010). ©2010, Optical Society of America.]

As same as a silica bottle microcavity, this microcavity is efficiently coupled to an optical fiber. In addition, thanks to the high nonlinearity of a-Si:H, threshold control power of 5 $\mu$W was demonstrated; this is the lowest input power required for achieving optical Kerr switching to my knowledge.

#### Fiber-based optical parametric oscillation switch

It is intuitive that fiber-based optical switches introduce any coupling loss because it directly connects to optical fibers. There are a variety of different fiber-based optical switches, but of these, I focus on P. Andrekson *et al.*[12] The experimental setup is shown in Fig. 1.8. A strong CW signal light and weak control pulses are inputted into a highly nonlinear fiber. Then, strong probe signal is converted to control pulses via four wave mixing (FWM) process in a fiber. Hence, modulated switch signal is obtained by filtering control light using band pass filter (BPF) at the output of the fiber,

In this scheme, strong CW probe signal (1.6 W) is switched by very weak (corresponding to 150 photons/pulse) control pulses. In addition, FWM is an instantaneous effect, thus switching with time of shorter than 10 ps is demonstrated.

### 1.4.2 Objective of this study

#### Analysis on previous studies

As introduced in previous subsections, precedence studies are present. However, they have some points that should be improved. (1) For optical Kerr switch using silica bottle microcavity, it is fabricated on optical fiber by using laser heating. So, it is difficult to

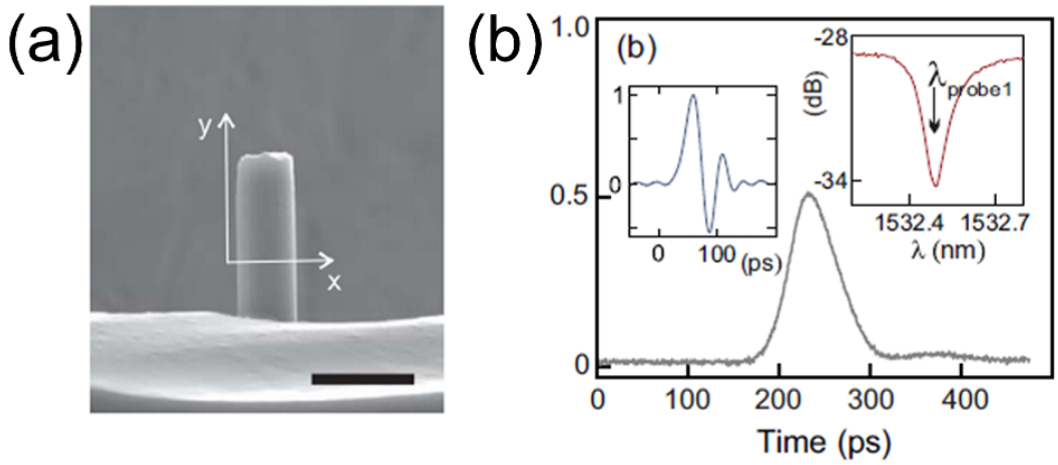


Fig. 1.7: (a) SEM image of hydrogenated amorphous silicon microcylindrical resonator. [Reprinted with permission from N. Vukovic, N. Healy, P. Horak, J. R. Sparks, P. J. A. Sazio, J. V. Badding, and A. C. Peacock, "Ultra-smooth microcylindrical resonators fabricated from the silicon optical fiber platform," Appl. Phys. Lett. **99**, 031117 (2011). ©2011, American Institute of Physics.] and (b) optical Kerr switching operation. [Reprinted from N. Vukovic, N. Healy, F. H. Suhailin, P. Mehta, T. D. Day, J. V. Badding, and A. C. Peacock, "Ultrafast optical control using the Kerr nonlinearity in hydrogenated amorphous silicon microcylindrical resonators," Sci. Rep. **3**, 2885 (2013). ©2013, Nature Publishing Group.]

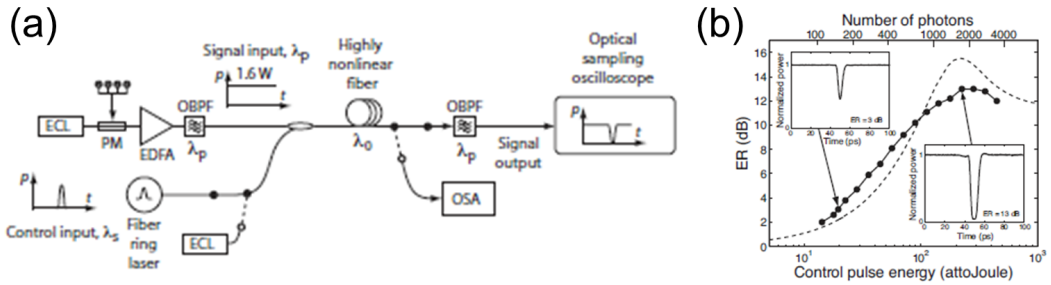


Fig. 1.8: (a) Schematic illustration of the experimental setup. (b) Optical Kerr switching operation [Reprinted from P. A. Andrekson, H. Sunnerud, S. Oda, T. Nishitani, and J. Yang, "Ultrafast, atto-joule switch using fiber-optic parametric amplifier operated in saturation," Opt. Express **16**, 10956-10961 (2008). ©2008, Optical Society of America.]

integrate on a chip. (2) For optical Kerr switch using a-Si:H microcylindrical resonators, it has a clear advantage in terms of switching control energy in comparison with the switch using in a silica bottle microcavity. However, it is made from an a-Si:H rod, thus it cannot be fabricated on a chip. (3) For fiber-based switch, it is not fabricated on a chip and its size is large (500 m). Moreover, it is built with one long optical fiber, thus it is difficult to demonstrate optical path switching, which was demonstrated in a silica bottle microcavity. Furthermore, it requires strong probe light, thus it is not suitable for achieving a few-photon-level switch where probe light is very weak.

To solve these problems, I decided to use a silica toroid microcavity[60] which is one of WGM microcavities. Detailed description of silica toroid microcavity is provided in the next sub-subsection.

#### Silica toroid microcavity

A silica toroid microcavity was fabricated by D. Armani *et al.*[60] in 2003 for the first time. Silica toroid microcavity is composed of a toroidal-shaped silica disk and a silicon pillar as shown in Fig.1.9(a). The light in a silica toroid microcavity propagates along the wall of a silica toroidal structure (Fig. 1.9(b)). Thus it is regarded as one of the WGM microcavities. In addition, it is the on-chip microcavity which has $Q$ larger than $10^8$. Before the development of a silica toroid microcavity, there was no microcavities with $Q > 10^8$ which can be fabricated on a chip[*k].

There are a lot of applications of a silica toroid microcavity. One of the attractive application is the optomechanics.[62] Due to its high $Q$ factor, the photon density is increased in a silica toroid microcavity. This high photon density makes the radiation pressure of the light observable. The radiation pressure deforms the cavity shape, and then vibration due to radiation pressure of the light is observed. In addition, a silica toroid microcavities are employed for investigating cavity QEDs. High $Q$ means that photons can be stored for a long time. This allows the light in the microcavity to interact with an atom many times with in the long cavity photon lifetime. The strong coupling was observed[61] by employing a silica toroid microcavity. Moreover, a photon turnstile was also demonstrated.[24] Besides optomechanics and cavity QED, there are a lot of different applications such as frequency comb source,[63] low threshold wavelength conversion,[69,31] lasers[30,70] and sensors.[71,72,64] They are taking advantage of the high-$Q$ of a toroid microcavity.

Here, I emphasize the merits obtained by using a silica toroid microcavity as platform for optical switch. It is well-known that silica toroid microcavity can be coupled to an optical fiber very efficiently.[73] Thus there is negligible loss when the light is coupled into a silica toroid microcavity from an optical fiber. Moreover, it can be fabricated on a chip, which is the most important advantage of a silica toroid microcavity. This feature has not been satisfied by previous studies described in 1.4.1, but it is important for the integration of optical switches. Furthermore, it was shown that an add-drop filter[28] is obtainable by using silica toroid microcavity[*l]. Therefore, considering these features, I

[*k] Recently, chemically-etched wedge-cavity was developed.[68] This microcavity is also on-chip microcavity which has $Q$ exceeding $10^8$.

[*l] It should be note it showed only "filter." Switching operation was not demonstrated in a silica

believe that silica toroid microcavity can improve the point that has not been achieved by the previous studies.

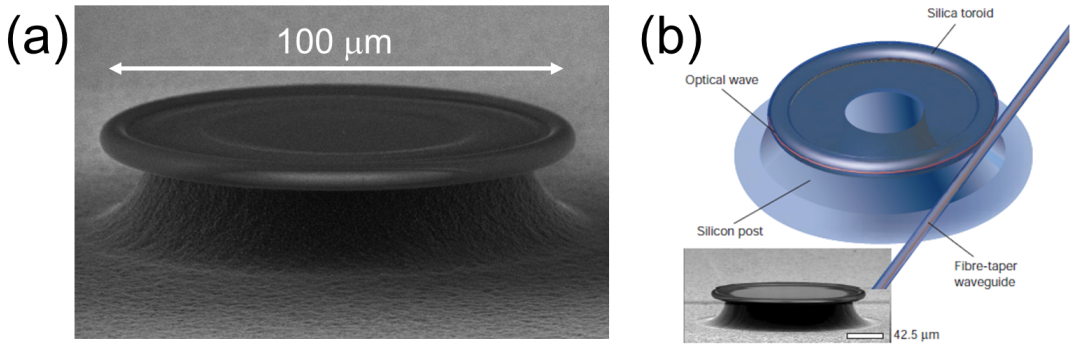


Fig. 1.9: SEM image of a silica toroid microcavity fabricated by our group. (b) Schematic of a silica toroid microcavity. [Reprinted with permission from K. Vahala, "Optical microcavities," Nature **424**, 839-846 (2003). ©2003, Nature Publishing Group.]

### Refractive index change in a silica toroid microcavity

We have to modulate refractive index of optical microcavity to obtain switching operation in a silica toroid microcavity. EO effect, TO effect, carrier-plasma effect and Kerr effect are generally used for this purpose as mentioned in 1.3.2. However, silica has a large bandgap (corresponding to $\lambda = 140$ nm). Hence, it is impossible to utilize carrier-plasma effect in a silica toroid microcavity when telecommunication wavelength (1550 nmm) is used. In addition, silica has a rotational symmetry, which indicate that EO effect cannot be employed. Therefore, there are two remaining choices for achieving optical switch such as TO effect and Kerr effect.

H. Rokhsari and K. Vahala*et al.*[74] experimentally revealed that there are both TO and Kerr effects in a silica toroid microcavity. And they also demonstrated that Kerr effect is much faster than TO effect. More qualitatively speaking, TO effect could follow the modulation frequency of up to 25 kHz while Kerr effect could follow the modulation frequency of higher than 10 MHz[*m]. This result shows that the use of Kerr effect is preferred in terms of switching speed. As a result, the use of Kerr effect for achieving fast switching is the key of my study in addition to the use of a silica toroid microcavity.

### Add-drop configuration

In general, microcavity-based optical switches are based on a side-coupled system[75] which consists of a microcavity and one waveguide (Fig. 1.10(a)). Optical switch with a side-

toroid microcavity with an add-drop system.

[*m]Kerr effect can follow much higher modulation frequency. However response time was limited up to ≈ 20 MHz due to the cavity photon lifetime in this experiments.

coupled system provides controllability on ON and OFF of the probe light, because there is only one set of input and output ports. However, it is desired to an optical switch to be able to switch the optical path for practical use in telecommunication network. We have to demonstrate microcavity switch with an add-drop system[76,28,18,77] that consists of a microcavity and two waveguide (Fig. 1.10(b)) to allow optical path switching.

Add-drop filter using a WGM microcavity is suitable for wavelength division multiplexing (WDM) system because a WGM microcavity has a narrow transmission band (i.e. high $Q$ factor). Indeed, an add-drop filter was developed by using a silica toroid microcavity.[28,77] However, they showed no active operation, such as optical path switching. So, achieving optical path switching in an silica toroid microcavity is not only new but also challenging.

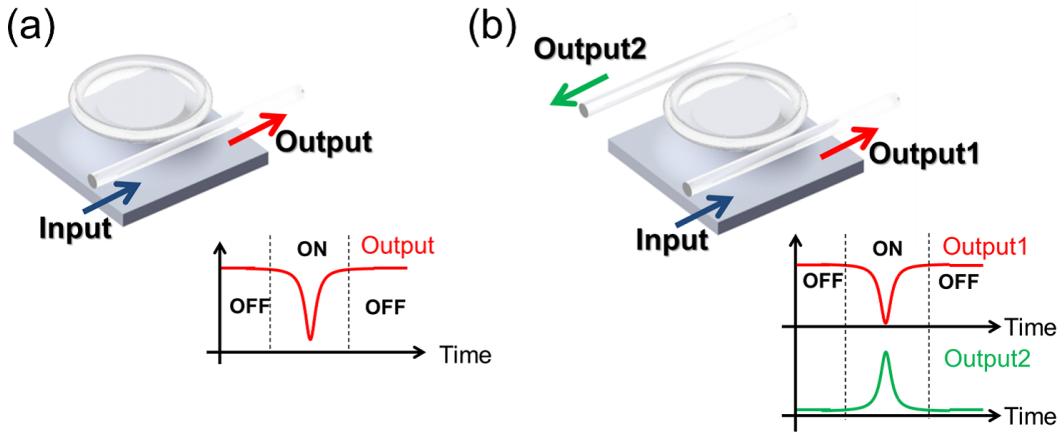


Fig. 1.10: Schematic illustration of image of a silica toroid microcavity based optical switch with (a) a side-coupled system and (b) an add-drop system.

### Objective of this study

The objective of this study is to demonstrate optical switch using Kerr effect in a silica toroid microcavity. By using a silica toroid microcavity, it is expected that microcavity-based switch with extremely low insertion loss is achieved. In addition, fast optical switching will be obtained by employing Kerr effect. In addition to the demonstration of an optical switch in a side-coupled system, I try to develop an add-drop system to demonstrate optical path switching.

## 1.5 Chapter overview

This thesis is composed of the following chapters. In chapter 2, theories that are related to silica toroid microcavity are briefly overviewed. In addition, fabrication process,

expressions of WGMs and Kerr effect in a silica toroid microcavity are described. In chapter 3, basics of the coupling between a waveguide and a microcavity are explained. I also introduce coupled mode theory to model the behavior of the light in a microcavity, coupling method, fabrication process of taper fiber and measurement procedure. In chapter 4, results on optical switch in a side-coupled system is shown. This chapter includes results of optical switches based on TO and Kerr effects. In chapter 5, result of optical switch in an add-drop system is shown. First, I describe an add-drop system composed of stages and a bent taper fiber. And then, experimental result with an add-drop system is shown. Finally, I conclude this thesis in chapter 6.

# Chapter 2

# Silica toroid microcavity

In this section, basics of silica toroid microcavity, which is used as a platform for optical switch in this thesis, are explained. First, I briefly introduce how I fabricated a silica toroid microcavity. Second, model of WGM is described by comparing cases of a microsphere and a silica toroid microcavity. Finally, I explain the origin of nonlinear refractive index change induced in a silica toroid microcavity.

## 2.1 Fabrication

In this section, fabrication process of a silica toroid microcavity is described. Fabrication of silica toroid microcavity can be devided into three parts, such as (1) photolithography (2) $SiO_2$ etching (3) $XeF_2$ dry etching (4) laser reflow[*a], as shown in Fig. 2.1. Here the overall fabrication process is overviewed. First, a silicon substrate with a thin layer of silica is prepared. The thickness of the silica layer is typically $1 - 3$ $\mu$m. Second, (1) photolithography process is performed. In this process, the circular resist pattern, of which diameter is $50 - 200$ $\mu$m, is developed on the substrate. Third, (2) $SiO_2$ etching is performed. The silica under the resist is protected from being damaged during this etching process. As a result, only silica that was protected by resist remains on a Si substrate after etching process. The circular patterns of resist is transferred into silica, thus disk-shaped silica is formed as shown in Fig. 2.1. Next, (3) $XeF_2$ dry etching is conducted on a patterned silicon wafer. $XeF_2$ selectively removes Si, thus silica disk is undercutted and disk-shaped silica on a silicon pillar is fabricated as shown in Fig. 2.1. This structure is used as a microcavity, but it cannot exhibit high-$Q$ because its surface is rough due to the dry etching. Therefore, for achieving high $Q$ factor, additional treatment is necessary.

Finally, (4) laser reflow process is conducted on a silica disk on a Si pillar. In a laser reflow process, the outer edge of silica disk is heated and melted, and finally it shrinks. As a result of the shrinkage, toroidal shape is formed as shown in Fig. 2.1. $CO_2$ laser is empolyed to melt the silica disk because absorption coefficinet of silica is

[*a]Photolighgraphy process and $SiO_2$ process were developed by the author's colleague T. Tetsumoto. $XeF_2$ dry etching process was optimized by the author's colleagues T. Kato and R. Suzuki. Laser reflow process was developed by the author and his colleague K. Ishikawa

very large at $CO_2$ laser wavelength (10.6 $\mu$m). This allows the light from $CO_2$ laser to be efficiently absorbed in the silica disk. The absorption of the light generates heat in the silica disk. Heat generated near the contract between silica disk and silicon pillar rapidly flows out to the chip thanks to the large thermal conuctivity of Si. On the other hand, heat generated at the outer edge of silica disk cannot dissipate because of small thermal conductivity of silica and surrounding air. Therefore, heat accumulates only at the outer edge of silica disk, and this allows to form toroidal shape. The most important outcome of this laser reflow process is that it can make the cavity surface very smooth. In general, microcavities fabricated on a Si chip, for example microring cavity, has large surface roughness originating from imperfect fabrication process. Such surface roughness results significant reduction of $Q$, thus microcavities without laser reflow process cannot have a high-$Q$ factor. On the other hand, laser reflow can form toroidal shape by taking advantage of surface tension. Thus very smooth surface can be obtained. This reduce surfaces scattering loss; thus high-$Q$ factor of $> 10^8$ can be achieved in a silica toroid microcavity.

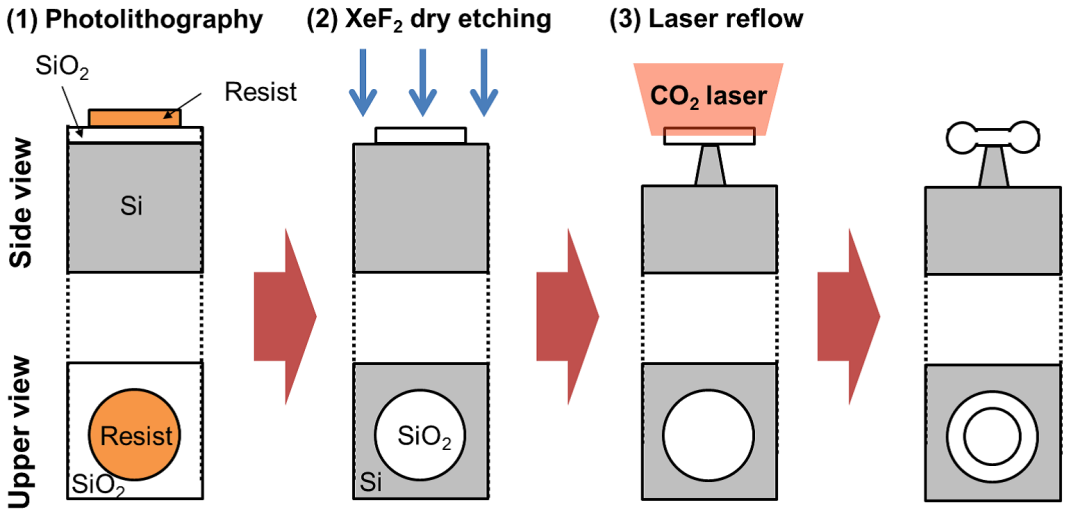


Fig. 2.1: Schematic illustration of fabrication process of a silica toroid microcavity.

## 2.2 WGM modes in a silica toroid microcavity

In this section, the electric field distribution in a WGM cavity (e.g. silica toroid microcavity, microshere cavity and so on) is described. The name Whispering Gallery was named after Whispering Gallery of St. Paul's Cathedral in London[78,57]. This gallery has a smooth ring-shaped sidewall. When someone whispers along the sidewall, this person's whisper propagates along the wall, and then, this person will hear the whisper from this person's back. WGM is anologous to this phenomena. When light is inputted

into a WGM cavity, light propagates along the inner surface of cavity by total internal reflection, and then it returns to the position where the light is inputted. If the phase of returned light is the same as that of input light, then a resonance occurs. This is the qualitative understanding of WGM.

In this section, rigorous analytical solutions of the WG modes in a microshepere is described in the begining. After that, I move to the expalanation of WG modes in a silica toroid microcavity, of which mode cannot be described analytically.

### 2.2.1 WG modes in a microsphere cavity

#### Derivating the equations of WGMs

Here, I derive the anaytical expression of WGMs in a microsphere cavity. To obtain WGMs, we start from the following Maxwell equations[79].

$$\nabla \times \mathbf{H} = \varepsilon \frac{\partial \mathbf{E}}{\partial t} \tag{2.1}$$

$$\nabla \times \mathbf{E} = -\mu \frac{\partial \mathbf{H}}{\partial t} \tag{2.2}$$

$$\nabla \cdot \mathbf{E} = 0 \tag{2.3}$$

$$\nabla \cdot \mathbf{H} = 0 \tag{2.4}$$

Where $\mathbf{E}$ and $\mathbf{H}$ are the electric and magnetic fields. $\varepsilon$ and $\mu$ are the permittivity and permeability of the cavity, respectively. Note that there are no carrier and no current in the cavity. Here I assume that permittivity and permeability are uniform in the cavity and electric field has time-dependency as $\propto \exp(j\omega t)$. Then, Eqs. (2.1) - (2.4) can be rewritten, as,

$$\left(\nabla^2 + \frac{\omega^2 n^2}{c^2}\right)\mathbf{E} = 0. \tag{2.5}$$

Where $c$ and $n$ are the light velocity and refractive index, respectively. Note that this equation is also valid for magnetic field $\mathbf{H}$.

Microsphere cavity is sphere-shaped, so it is reasonable to use spherical coordinate system for analyzing the modes in such a cavity. The schematic illustration of the spherical coordinate system is shown in Fig. 2.2. Cartesian coordinate can be translated into spherical coordinate system by employing the following relations as $x = r\sin\theta\cos\phi$, $y = r\sin\theta\sin\phi$, $z = r\cos\theta$. Thus the wave equation in spherical coordinate can be written, as

$$\left[\frac{1}{r^2}\frac{\partial}{\partial r}\left(r^2\frac{\partial}{\partial r}\right) + \frac{1}{r^2\sin\theta}\frac{\partial}{\partial\theta}\left(\sin\theta\frac{\partial}{\partial\theta}\right)\frac{1}{r^2\sin\theta}^{\,2}\frac{\partial^2}{\partial\phi^2}\frac{\omega^2 n^2}{c^2}\right]\mathbf{E}(r,\theta,\phi) = 0. \tag{2.6}$$

Next, I consider the polarization of the light that propagates inside a microsphere. Similar as the light in a slab waveguide, it can be divided into two modes: a TE-like mode and a TM-like mode[78,80]. For a TE-like mode $E_r = E_\phi = 0$ because the electric field is parallel to the surface of microsphere. In like manner, $H_r = H_\phi = 0$ for TM-like mode. In addition, we can use scalar $E$ instead of vector $\mathbf{E}$ in (2.6) because the

polarization barely changes during propagation inside the cavity. I can calculate electric field in all the other directions by using $E_\phi$ for TM-like mode and $H_\phi$ for TE-like mode. Thus Eq. (2.6) is written by using only $E_\phi$ for the TM-like mode, as,

$$\left[\frac{1}{r^2}\frac{\partial}{\partial r}\left(r^2\frac{\partial}{\partial r}\right)+\frac{1}{r^2\sin\theta}\frac{\partial}{\partial\theta}\left(\sin\theta\frac{\partial}{\partial\theta}\right)+\frac{1}{r^2\sin\theta}^{2}\frac{\partial^2}{\partial\phi^2}\frac{\omega^2n^2}{c^2}\right]E_\phi=0. \tag{2.7}$$

This is the equation that I must solve for obtaining rigorous analytic solution of WGM distribution.

To solve Eq. (2.7), $E_\phi$ is separated as $E_\phi=\psi_r(r)\psi_\theta(\theta)\psi_\phi(\phi)$[*b]. Then, by substituting it into Eq. (2.7), I obtain the following equation.

$$\frac{1}{\psi}\frac{\partial}{\partial r}\left(r^2\frac{\partial\psi_r}{\partial r}\right)+\frac{1}{\psi_\theta\sin\theta}\frac{\partial}{\partial\theta}\left(\sin\theta\frac{\partial\psi_\theta}{\partial\theta}\right)+\frac{1}{\psi_\phi\sin\theta^2}\frac{\partial^2\psi_\phi}{\partial\phi^2}+\frac{n^2\omega^2}{c^2}r^2=0. \tag{2.8}$$

This is the equation that describes WGMs in a microsphere. Next I show the method to solve Eq. (2.8). By assuming the resonance in the direction of $\phi$ ($\psi_\phi=\frac{1}{\sqrt{2\pi}}\exp(\pm jm\phi)$), we obtain

$$\frac{1}{\psi_\phi}\frac{\partial^2\psi_\phi}{\partial\phi^2}=-m^2. \tag{2.9}$$

Then, I substitute Eq. (2.9) into Eq. (2.8) and deform it, the equation which is independent on $\phi$ is calculated, as

$$\frac{1}{\psi}\frac{\partial}{\partial r}\left(r^2\frac{\partial\psi_r}{\partial r}\right)+\frac{n^2\omega^2}{c^2}=-\frac{1}{\psi_\theta\sin\theta}\frac{\partial}{\partial\theta}\left(\sin\theta\frac{\partial\psi_\theta}{\partial\theta}\right)+\frac{m^2}{\sin\theta^2}. \tag{2.10}$$

When I assume that both righthand and lefthand sides of Eq. (2.10) is equal to $\lambda$, we can divide Eq. (2.10) into two independent equations, as,

$$\frac{1}{\sin\theta}\frac{\partial}{\partial\theta}\left(\sin\theta\frac{\partial\psi_\theta}{\partial\theta}\right)+\left(\lambda-\frac{m^2}{\sin\theta^2}\right)\psi_\theta=0 \tag{2.11}$$

$$\frac{\partial}{\partial r}\left(r^2\frac{\partial\psi_r}{\partial r}\right)+\left(k^2r^2-\lambda\right)\psi_r=0. \tag{2.12}$$

These two equations are the basic formulas of WGMs. Thus, by solving these two equations, I am able to obtain $E_\phi=\psi_r(r)\psi_\theta(\theta)\psi_\phi(\phi)$.

First, I solve Eq. (2.11). By assuming $x=\cos\theta$, Eq. (2.11) is rewritten, as,

$$\frac{\partial}{\partial x}\left[(1-x^2)\frac{\partial\psi_\theta}{\partial x}\right]+\left[\lambda-\frac{m^2}{1-x^2}\right]\psi_\theta=0. \tag{2.13}$$

When $\lambda=l(l+1)$ is assumed, Eq. (2.13) turns out as associated Legendre polynomials. Hence, the solution of the equation is found to be the 1st class associated Legendre function expressed by $P_l^m(x=\cos\theta)$.

[*b] In silica toroid microcavity, this "variable separation method" cannot be applied. This is the reason why there is no analytical solution for WGM in a silica toroid microcavity. Detailed discussion about this points will be provided in the later.

As for Eq. (2.12), by employing the conversion of $r' = kr$, it can be deformed into spherical Bessel differential equation, as,

$$\frac{\partial^2 \psi_r}{\partial r'^2} + \frac{2}{r}\frac{\partial \psi_r}{\partial r} + \left[1 - \frac{l(l+1)}{r'^2}\right]\psi_r = 0. \tag{2.14}$$

It is well-known that such a equation has Bessel function $J_l(kr)$ and Hankel function $H_l(kr)$ as solutions. However Hankel function is not suitable for expressing electromagnetic wave inside of microsphere because it diverges at $r = 0$. Therefore, WGM inside of microsphere is expressed by Bessel function. On the other hand, Hankel function converges in zero at $r = \infty$, thus it can write decaying wave outside of the microsphere. In summary, as for $\psi_r$, it have to be expressed by Bessel function inside of microsphere and by Hankel function outside of microsphere. Note that it is necessary to adjust $\Psi_r$ for making $E_\phi$ continuity on the boundary of microsphere.

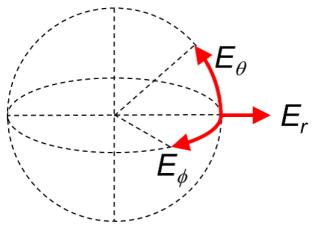


Fig. 2.2: Schematic illustration of the spherical coordinate system.

### Calculation of WGMs

According to B. Little *et al.*,[81] the equations of WGMs shown above is simplified by employing the following two approximations;

1. Focusing on near the cavity surface ($(r - R_0)/R_0 << 1$), where $R_0$ is the radius of microsphere.

2. Focusing on near the cavity equator ($\theta << 1$).

Under such approximations, I obtain an analytical solution $\Psi_{l,m,n}(r, \theta, \phi)$ of WGMs, as,

$$\Psi_{l,m,n}(r, \theta, \phi) = N_s \psi_r(r)\psi_\theta(\theta)\psi_\phi(\phi), \tag{2.15}$$

$$\psi_\phi = \exp\left[\pm jm\phi\right], \tag{2.16}$$

$$\psi_\theta = \exp\left[-\frac{m}{2}\theta^2\right] H_N(\sqrt{m}\theta), \tag{2.17}$$

$$\psi_r = \begin{cases} j_l(kn_s r), & r \le R_0 \\ j_l(kn_s R_0)\exp\left[-\alpha_s(r - R_0)\right], & r \ge R_0 \end{cases} \tag{2.18}$$

where the coefficients are defined, as,

$$N_s = \left\{ \sqrt{\frac{\pi}{m}} 2^{N-1} N! R_0^2 \left[ \left( 1 + \frac{1}{\alpha_s R_0} \right) j_l^2(k n_s R_0) \right. \right. \\ \left. \left. - j_{l-1}(k n_s R_0) j_{l+1}(k n_s R_0) \right] \right\}^{-1/2}, \tag{2.19}$$

$$\alpha_s = \sqrt{\beta_l^2 - k^2 n_0^2}, \tag{2.20}$$

$$\beta_l = \frac{\sqrt{l(l+1)}}{R_0}, \tag{2.21}$$

$$N = l - m, \tag{2.22}$$

where $N_s$, $n_s$,$n_0$,$\alpha_s$,$\beta_l$ and $H_N$ are the normalization factor, the refractive index of microsphere and surroundings, the decaying rate of WGM in the direction of $r$, the propagation constant of $l$-th mode and Hermite polynomials, respectively. Eqs. (2.15) - (2.22) are the complete sets of solutions of WGMs. However, in these equations, there is no dependency on radial mode number $n$. This is because the dependency on $n$ is included in the choice of wavevector $k$. $\lambda(= 2\pi/k)$ must be equal to the resonant wavelength of a WGM to excite a WGM in a microsphere, . Hence, $k$ is allowed to take particular values in a microsphere. The equation that determine constraint on $k$ is given, as,[81]

$$\left( \eta_s \alpha_s + \frac{l}{R_0} \right) j_l(k n_s R_0) = k n_s j_{l+1}(k n_s R_0). \tag{2.23}$$

$$\eta_s = \begin{cases} 1, & \text{TE modes} \\ \frac{n_s^2}{n_0^2}, & \text{TM modes} \end{cases}$$

Note that Eq. (2.23) is derived from condition of continuity of **E** and **H** on a boundary of a microsphere. There are several $k$s that satisfy Eq. (2.23) and each $k$ corresponds each radial mode number $n$. Here, for instance, WGMs with different $l$ and $m$ in microsphere with diameter of 25 $\mu$m are shown in Fig. 2.3(a)-(d). Fig. 2.3(a) shows a fundamental WGM with $l = m = 66$ and it indicates that there is only one peak both in the directions of $r$ and $\theta$. On the other hand, Figs. 2.3(b)-(d) demonstrate higher-order WGMs with $(l, m, n) = (66, 65, 1)$, $(66, 64, 1)$ and $(66, 66, 2)$. Form Figs. 2.3(a)-(d), the number of peaks in the directions of $r$ and $\theta$ are found to be characterized by $n$ and $l - m + 1$.

Here, intuitive understanding of each WGM is described. Pathways of modes with different $l$ and $m$ values are shown in Figs. 2.3(e). Fundamental mode ($l = m$) propagates near the equator of a microsphere (the red solid line in Fig. 2.3(e)). On the other hand, higher-order modes ($m \neq l$) propagate along "zig-zag path" around an equatorial plane.[81] When $m$ is decreased for fixed $l$ number, a mode has larger inclination (the blue and green solid lines in Fig. 2.3(e)). Finally inclination becomes 90 deg. when $m = 0$. It should be noted that WGMs with same $l$ and different $m$ has same resonant wavelength nevertheless they have different optical pathways[*c]. Although a mode with $m < l$ seems to have longer pathway than a mode with $l = m$, the radius of circumference is smaller when latitude is higher. This make pathway of WGMs with $m < l$ shorter than it looks. Hence,

[*c]It is called "degeneration."

resonant wavelength of WGMs which have different $m$ numbers are matched. However, in practice, it is difficult to fabricate perfect microsphere, and fabricated microsphere has slight distortion. This distortion breaks degeneration of WGMs with same $l$ and create frequency separation between modes, as

$$\delta f_{l,m}/f_{l,m} = e\{1/3 - (l - |m|)/l\}, \tag{2.24}$$

where $\delta f_{l,m}$, $f_{l,m}$ and $e$ are frequency shift and frequency of mode with $l$ and $m$ and ellipticity, respectively.[82] Likely to resonant wavelength, propagation constants of WGM is determined depending on $l$ as $\beta_l = \sqrt{l(l-1)}/R_0$. However, WGMs with different $m$ propagate in different inclinations, thus propagation constants projected on equatorial plane depend on $m$, as $\beta_m = m/R_0$. Note that $\beta_l$ becomes nearly equal to $\beta_m$ in the regime where $m = l$ because mode with $m = l$ propagates along the equatorial plane. Therefore, as discussed later, I can excite a desired WGM by carefully adjusting the propagation constant of input waveguide mode.[83]

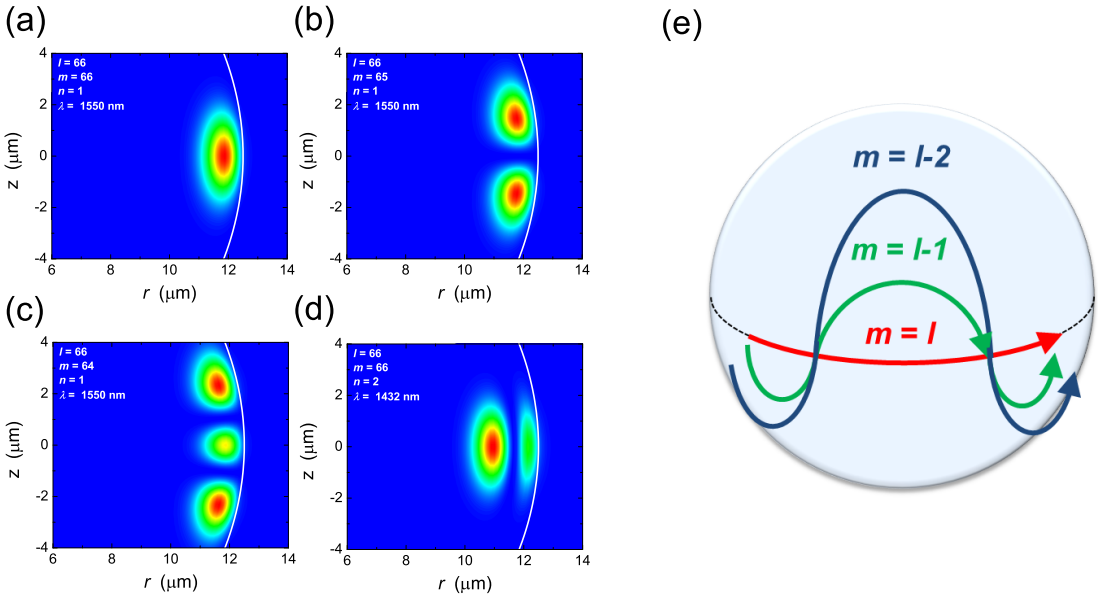


Fig. 2.3: (a)-(d) Calculated WGMs in a microsphere with diameter of 25 $\mu$m. They were obtained by plotting the Eqs. (2.15) - (2.22) by using MATLAB. (e) Interpretation of modes with $l = m$ and $l \neq m$.

### 2.2.2 WG modes in toroid microcavity

As for WGMs in a silica toroid microcavity, there is no exact analytic solution because variable separation method cannot be applied for WGMs in a toroid microcavity. Thus, approximate solution is obtained by using perturbative method.[84] In this section, this approximation method is overviewed for giving qualitative understanding of WGMs in a toroid microcavity. B. Min *et al.*[84] gave approximate analytic solution for WGMs in

a toroid microcavity. For modeling the toroidal structure, the wave equation is turned into a cylindrical coordinate system, as,

$$\left\{ \frac{\partial^2}{\partial R^2} + \frac{1}{R}\frac{\partial}{\partial R} + \frac{1}{R^2}\frac{\partial^2}{\partial \theta^2} + \frac{\partial^2}{\partial z^2} + k^2 n^2 \right\} E_z = 0, \tag{2.25}$$

where $E_z$, $k$ and $n$ are the electric field in the $z$ direction, the wave vector and refractive index change in the cavity, respectively. Cylindrical coordinate system ($R$, $\theta$, $z$) is shown in Fig. 2.4(a). It should be noted that Eq. (2.25) assumes that electric field is dominated by $E_z$ (quasi-TE mode) and electric field in the $\theta$ direction is negligible to treat electric field as scalar wave. Under the condition where aspect ratio $\delta = r_0/R_0$ is larger than 0.1, that assumption is no longer valid. Where $r_0$ and $R_0$ are minor and major radius of a silica toroid microcavity as shown in Fig. 2.4(a) Here, for more intuitively modeling the toroidal structure, the local toroidal coordinate system is introduced, as,[85]

$$\begin{cases} R = R_0 + r\cos\phi \\ \theta = z/R_0 \\ z = r\sin\theta \end{cases} \tag{2.26}$$

where ($r$, $\phi$, $\theta$) are the coordinates in the local toroidal coordinate system shown in Fig. 2.4(a). Under such coordinate system, both Eq. (2.25) and electric field in $z$ direction $E_z$ is rewritten, as,

$$\begin{aligned} &\left\{ \frac{\partial^2}{\partial r^2} + \frac{1}{r}\frac{\partial}{\partial r}\frac{1}{r^2}\frac{\partial^2}{\partial \phi^2} + k^2 n^2 \right\} \Psi(r,\phi) \\ &\qquad + \left(1 + \delta\frac{r}{r_0}\cos\phi\right)^{-2} \left(\frac{1}{4R_0^2} - \beta^2\right) \Phi(r,\phi) = 0, \end{aligned} \tag{2.27}$$

$$E_z = N(1 + r/r_0\cos\phi)^{-1/2}\Phi(r,\phi)e^{-jm\theta}, \tag{2.28}$$

where $N$ and $\Phi(r,\phi)$ are the normalization constant and the wave function in a toroid microcavity, respectively.

To solve the wave equation shown above, perturbative method[84] is employed. First the wave function $\Psi$ is expressed by the perturbation expansion, as,

$$\Psi = \sum_i \delta^i \Psi^{(i)} \tag{2.29}$$

where $\Psi^{(i)}$ is the $i$-th order perturbation expansion. By substituting Eq. (2.29) into Eqs. (2.27) and (2.28), I obtain the following three equations:

$$D\Psi^{(0)}(r,\phi) = 0, \tag{2.30}$$

$$D\Psi^{(1)}(r,\phi) = -2\beta^2 \left(\frac{r}{r_0}\right)\cos\phi\Psi^{(0)}(r,\phi), \tag{2.31}$$

$$\begin{aligned} D\Psi^{(2)}(r,\phi) = &-2\beta^2 \left(\frac{r}{r_0}\right)\cos\phi\Psi^{(1)}(r,\phi) \\ &+ \left[3\beta^2\left(\frac{r}{r_0}\right)^2\cos^2\phi - \frac{1}{4r_0^2}\right]\Psi^{(0)}(r,\phi), \end{aligned} \tag{2.32}$$

$$D \equiv \left[\frac{\partial^2}{\partial r^2} + \frac{1}{r}\frac{\partial}{\partial r} + \frac{1}{r^2}\frac{\partial^2}{\partial \phi^2} + (k^2 n^2 - \beta)\right]. \tag{2.33}$$

It should be noted that $\Psi(r, \phi)$ is obtained by calculating Eqs. (2.30)-(2.32) in turns. Finally, by considering the boundary condition, we obtain a complete solutions for Eq. (2.27). Calculated WGMs in a toroid microcavity is shown in Fig. 2.4(b). Similar to the case of WGMs in a microsphere, $l$ and $m$ are the polar and the azimuthal mode numbers, respectively, but their interpretation is slightly different.[84] In the case of microsphere, fundamental mode is characterized by $n = 1$ and $l = m$. On the other hand, in the case of toroid microcavity, fundamental mode is characterized by $q = l = 0$. In addition, azimuthal mode number $m$ is decoupled.

The solutions obtained from this method will give quick understanding of WGMs in a toroid microcavity. However, the accuracy of this method decreases under the condition where $\delta > 0.1$. Therefore, for an accurate calculation, it is necessary to rely on numerical methods. To numerically calculate the WGMs in a toroid microcavity, finite element method (FEM) is very useful. Especially, M. Oxborrow[86] provides the method on the way to use the commercial FEM solver "COMSOL muiltiphysics" for calculating the WGMs in a silica toroid microcavity.

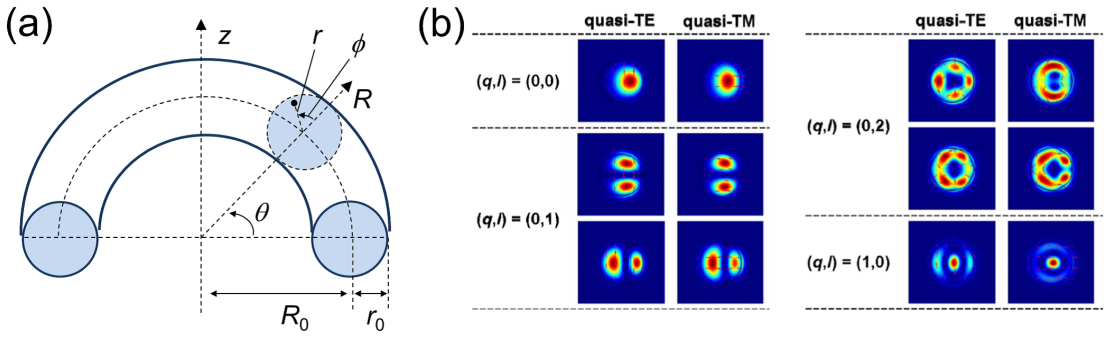


Fig. 2.4: (a) The local toroidal coordinate system.[84] (b) WGMs with $m = 163$ in a toroid cavity calculated by using analytic perturbative theory. A toroid cavity with a major and minor diameters of 60 $\mu$m and 3 $\mu$m is assumed. [Reprinted from B. Min, L. Yang, and K. Vahala, "Perturbative analytic theory of an ultrahigh-Q toroidal microcavity," Phys. Rev. A **76** (2007). ©2007, American Physical Society.]

## 2.3 Nonlinear refractive index change in a silica toroid microcavity

In this section, nonlinear optical process in a silica toroid microcavity is described. In particular, I focus on the Kerr effect, which is the one of the keys of this study. When a weak electric field is applied to a dielectric, polarization is induced as shown in the following equation, as,

$$P = \varepsilon_0 \chi E, \tag{2.34}$$

where $\chi$ is the electric susceptibility. Note that scalar electric field $E$ and polarization $P$ are assumed. However, it is well known that nonlinear polarization become obvious when applied electric field is strong, like,

$$P = \varepsilon_0 \chi^{(1)} E + \chi^{(2)} E^2 + \chi^{(3)} E^3 + \cdots \tag{2.35}$$

where $\chi^{(2)}$ and $\chi^{(3)}$ are the second- and third-order electric susceptibility. Usually 2nd- and 3rd-order nonlinear polarization is very small, thus polarization is approximated as Eq. (2.34). However, as shown in Eq. (2.35), they are in proportion to $E^2$ and $E^3$. Hence, they become obvious when the applied electric filed is very strong. As described before, the light energy density is enhanced in the microcavity due to its high $Q$ factor and small mode volume. Therefore, such nonlinear polarizations can be efficiently induced in a microcavity.

For characterizing the effect of the nonlinear polarizations, here I assume that the following electric field is applied:

$$E = \mathrm{Re}\left[E_1 \exp\left(j\omega_1 t\right) + E_2 \exp\left(j\omega_2 t\right)\right]. \tag{2.36}$$

Then, by substituting Eq. (2.36) into Eq. (2.35) and assuming the use of a silica toroid microcavity ($\chi^{(2)} = 0$), I obtain a polarization, given as,

$$\begin{aligned} P &= \varepsilon_0 \chi^{(1)} \mathrm{Re}\left[E_1 \exp\left(j\omega_1 t\right) + E_1 \exp\left(j\omega_2 t\right)\right] \\ &+ \chi^{(3)} \mathrm{Re}\left[(3|E_1|^2 + 6|E_2|^2) E_1 \exp\left(j\omega_1 t\right) + (6|E_1|^2 + 3|E_2|^2) E_2 \exp\left(j\omega_2 t\right)\right. \\ &\quad + 3|E_1|^2 E_2 \exp\left\{j(2\omega_1 - \omega_2)t\right\} + 3E_1 |E_2|^2 \exp\left\{j(2\omega_2 - \omega_1)t\right\} \\ &\quad \left. + |E_1|^2 E_1 \exp\left(j3\omega_1 t\right) + |E_2|^2 E_2 \exp\left(j3\omega_2 t\right)\right]. \end{aligned} \tag{2.37}$$

It should be noted that there are polarizations that have different frequencies from $\omega_1$ and $\omega_2$ although input light has only two frequency of $\omega_1$ and $\omega_2$, and they are the origins of nonlinear wavelength conversion. For example, the third term in the right hand of Eq. (2.37) ($\omega = 2\omega_1 - \omega_2$ or $2\omega_2 - \omega_1$) is the FWM.[31] On the other hand, the fourth term ($\omega = 3\omega_1$ or $3\omega_2$) is the third-harmonic generation.[69] However, here I focus on the second term ($\omega = \omega_1$ or $\omega_2$) that is the Kerr effect. For simplicity, I extract polarization that has a frequency of $\omega_1$ from Eq. (2.37), as,

$$P_{\omega_1} = \varepsilon_0 \left(\chi^{(1)} + 3\chi^{(3)} \frac{E_1^2 + 2E_2^2}{\varepsilon_0}\right) \mathrm{Re}\left[E_1 \exp\left(j\omega_1 t\right)\right] \tag{2.38}$$

I find an additional term of $3\chi^{(3)} \frac{E_1^2 + 2E_2^2}{\varepsilon}$ in (2.38) by comparing Eqs. (2.38) with (2.34). This is equivalent to that susceptibility is changed from $\chi^{(1)}$ to $\left(\chi^{(1)} + 3\chi^{(3)} \frac{E_1^2 + 2E_2^2}{\varepsilon_0}\right)$ due to induced nonlinear polarization shown in Eq. (2.37). Here I define $\Delta\chi$, as,

$$\Delta\chi = 3\chi^{(3)} \frac{E_1^2 + 2E_2^2}{\varepsilon} = \frac{6\chi^{(3)}}{\varepsilon}(I_1 + 2I_2). \tag{2.39}$$

Note that relations $I_1 = |E_1|^2/2\eta$, $I_2 = |E_2|^2/2\eta$ and $\eta = \sqrt{\mu_0/\varepsilon}$ were used. Here I try to connect refractive index change $\Delta n$ with the electric susceptibility change $\Delta\chi$. In

general, refractive index $n$ is expressed by using $\chi$, as $n = \sqrt{1+\chi}$. Hence, I obtain the equation by differentiating this relation, given as,

$$\frac{\mathrm{d}\chi}{\mathrm{d}n} = \frac{1}{2}(1+\chi)^{-\frac{1}{2}} = \frac{1}{2n}. \tag{2.40}$$

By using Eq. (2.40), I obtain the following important equation, as,

$$\Delta n = \frac{\mathrm{d}n}{\mathrm{d}\chi}\Delta\chi = \frac{3\chi^{(3)}\eta}{\varepsilon n}(I_1 + 2I_2) = n_2(I_1 + 2I_2), \tag{2.41}$$
$$n_2 = \frac{3\chi^{(3)}\eta}{\epsilon n}.$$

This equation shows that refractive index is changed according to the intensity of the light $I_1$ and $I_2$. This is the Kerr effect. It should be noted that refractive index change caused by $n_2 I_1$ is known as self-phase modulation (SPF); The light with frequency $\omega_1$ is affected by the light that has the same frequency of $\omega_1$. On the other hand, refractive index change caused by $n_2 I_2$ is known as cross-phase modulation (XPM); The light with frequency $\omega_1$ is affected by the light which has the different frequency $\omega_2$. SPM and XPM have been intensively studied in the field of "fiber optics"[87] and they are usually regarded as obstacle to submit the correct optical signal in an optical fiber for a long distance. However, for achieving optical switch, XPM is essential. The method on using XPM for optical switch will be clarified in 4.1.

# Chapter 3

# Coupling light into an optical microcavity

WGM cavity is attractive for a large number of applications such as quantum optics, optomechanics, high sensitive sensors, optical memories and optical switches due to its high quality factor and small mode volume. For taking advantage of such cavity, it is necessary to couple light into and out of the cavity. In this chapter, I discuss method on coupling the light into WGM cavity. First, I introduce coupled mode theory which is a simple but powerful tool for analyzing the light behavior in the system composed of a cavity and waveguides. Next, I explain several coupling method, in particular taper fiber method. Then, fabrication process of a taper fiber used in our group is described. Finally, the method on the coupling and characterizing a silica toroid microcavity is explained with some experimental data.

## 3.1 Coupled mode theory

Coupled mode theory (CMT)[88] is a powerful method which allows us to model the behavior of light in various structures. Other methods, for example, finite-difference time-domain (FDTD) method directly solve the Maxwell equations for obtaining the behavior of the light. On the other hand, CMT focuses only on amplitudes of " modes " in a structure, thus it can simply model the behavior of the light. CMT has been used to model the interaction between adjacent waveguides.[89] However, recently it is also employed for designing optical circuit which contains optical microcavities.[90,75] In this section, first I model a side-coupled system (a cavity with a one waveguide) for simplicity. I provide basic understanding of a coupling behavior of the microcavity by using the model. Next, I model an add-drop system (a cavity with two waveguides). In this thesis I use a silica toroid microcavity, which is one of the ring-shaped microcavities. Hence, a ring cavity (which is analogous to a silica toroid microcavity) is assumed in this section.

### 3.1.1 Side-coupled system

I start from the following master equation based on CMT[*a], as,

$$\frac{\mathrm{d}a}{\mathrm{d}t} = \left(j\omega_0 - \frac{1}{2\tau_{\mathrm{load}}}\right)a + \sqrt{\frac{1}{\tau_{\mathrm{coup}}}}\exp\left(j\theta\right)s_{\mathrm{in}}, \tag{3.1}$$

where $a$ and $s_{\mathrm{in}}$ are the electromagnetic waves in the microcavity and input waveguide, respectively. It should be noted that the light energy $U_{\mathrm{cavity}}$ and the input power $P_{\mathrm{in}}$ are given by $|a|^2 = aa^*$ and $|s|^2 = s_{\mathrm{in}}s_{\mathrm{in}}^*$. $\omega_0$ and $\theta$ are the resonant angular frequency of the cavity and the relative phase between $a$ and $s_{\mathrm{in}}$, respectively. And loaded photon lifetime $\tau_{\mathrm{load}}$ is written by $\tau_{\mathrm{load}} = (\tau_{\mathrm{int}}^{-1} + \tau_{\mathrm{coup}}^{-1})^{-1}$, where $\tau_{\mathrm{int}}$ and $\tau_{\mathrm{coup}}$ are the intrinsic photon lifetime and the photon lifetime related to the coupling between the cavity and the waveguide, respectively (Fig. 3.1). The second term in the right hand side of Eq. (3.1) indicates that decay of the cavity mode $a$. The last term in the right hand side shows that the input power $s_{\mathrm{in}}$ couples into the cavity at a rate of $\sqrt{\frac{1}{\tau_{\mathrm{coup}}}}$. The input wave $s_{\mathrm{in}}$ excites $a$ that propagates in counterclockwise (CCW) direction as shown in Fig. 3.1. There is coupling between CCW and clockwise (CW) modes in a ultra-high $Q$ cavity due to the Rayleigh scattering resulted by the surface inhomogeneities and density fluctuation.[91] However, for simplicity, I assume an ideal cavity where only a CCW mode is excited.

Output mode amplitude $s_{\mathrm{out}}$ is written, as,

$$s_{\mathrm{out}} = \exp\left(-j\beta d\right)\left[s_{\mathrm{in}} - \sqrt{\frac{1}{\tau_{\mathrm{coup}}}}\exp\left(-j\theta\right)a\right], \tag{3.2}$$

where $\beta$ and $d$ are the propagation constant and the length of the waveguide, respectively. As can be seen in Eq. (3.2), the output mode $s_{\mathrm{out}}$ is determined by the interference between the cavity mode $a$ and input mode $s_{\mathrm{in}}$. This complicated physics enables the output mode to destructively interfere when cavity is on resonance as described later. Note that this is the clear advantage of a side-coupled cavity system[75] than a direct cavity system[92] because it allows microcavity-based switch exhibit large contrast between ON and OFF at the output.

Here transmission characteristics of a side-coupled microcavity system is obtained by employing CMT. When we assume a static condition ($a \propto \exp\left(j\omega t\right)$), the relation between $a$ and $s_{\mathrm{in}}$ is given, as,

$$a = \frac{\sqrt{\frac{1}{\tau_{\mathrm{coup}}}}\exp\left(j\theta\right)}{j(\omega-\omega_0) + \frac{1}{2\tau_{\mathrm{load}}}}s_{\mathrm{in}}. \tag{3.3}$$

By substituting Eq. (3.3) into Eq. (3.2), the relation between $s_{\mathrm{out}}$ and $s_{\mathrm{in}}$ is obtained, as,

$$\begin{aligned} s_{\mathrm{out}} &= \exp\left(j\beta d\right)\left[\frac{j(\omega-\omega_0) + \frac{1}{2\tau_{\mathrm{load}}} - \frac{1}{\tau_{\mathrm{coup}}}}{j(\omega-\omega_0) + \frac{1}{\tau_{2\mathrm{load}}}}\right]s_{\mathrm{in}} \\ &= \exp\left(j\beta d\right)\left[\frac{j(\omega-\omega_0) + \frac{1}{2}\left(\frac{1}{\tau_{\mathrm{int}}} - \frac{1}{\tau_{\mathrm{coup}}}\right)}{j(\omega-\omega_0) + \frac{1}{2}\left(\frac{1}{\tau_{\mathrm{int}}} + \frac{1}{\tau_{\mathrm{coup}}}\right)}\right]s_{\mathrm{in}}. \end{aligned} \tag{3.4}$$

[*a] A large part of this section refer to C. Manolatou *et al.*[88]

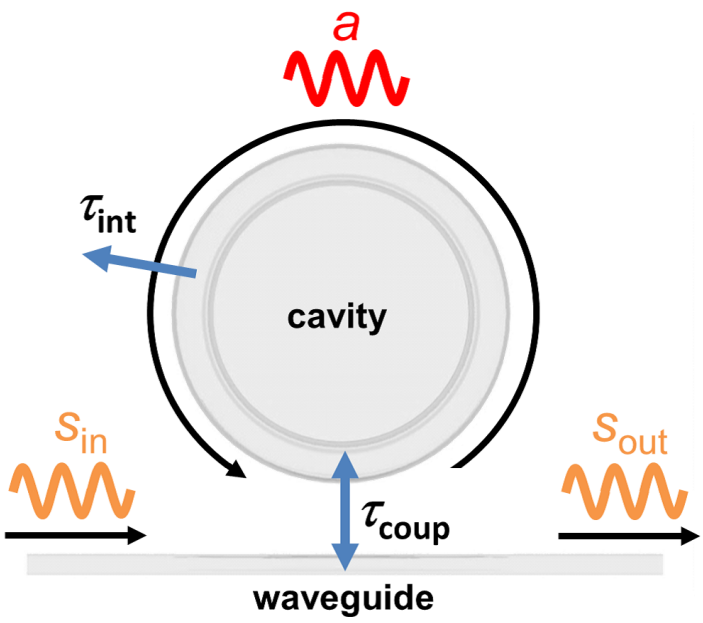


Fig. 3.1: Schematic of CMT model with a side-coupled ring cavity.

Note that $\tau_{\text{load}}^{-1} = \tau_{\text{int}}^{-1} + \tau_{\text{coup}}^{-1}$ is used. Transmittance $Tr$ is defined as $Tr = P_{\text{out}}/P_{\text{in}} = |(s_{\text{out}}/s_{\text{in}})|^2$, thus,

$$\begin{aligned} Tr &= \frac{(\omega-\omega_0)^2 + \frac{1}{4}\left(\frac{1}{\tau_{\text{int}}} - \frac{1}{\tau_{\text{coup}}}\right)^2}{(\omega-\omega_0)^2 + \frac{1}{4}\left(\frac{1}{\tau_{\text{int}}} + \frac{1}{\tau_{\text{coup}}}\right)^2} \\ &= \frac{4\pi^2c^2(\frac{1}{\lambda} - \frac{1}{\lambda_0})^2 + \frac{1}{4}\left(\frac{1}{\tau_{\text{int}}} - \frac{1}{\tau_{\text{coup}}}\right)^2}{4\pi^2c^2(\frac{1}{\lambda} - \frac{1}{\lambda_0})^2 + \frac{1}{4}\left(\frac{1}{\tau_{\text{int}}} + \frac{1}{\tau_{\text{coup}}}\right)^2}. \end{aligned} \tag{3.5}$$

Figure 3.2(a) shows the transmission spectrum obtained by Eq. (3.5). This graph clearly shows that transmittance is the minimum when the input wavelength is matched to the resonant wavelength ($\delta\lambda/\Delta\lambda_{\text{FWHM}} = 0$). This is because the phase of input wave and wave outputted from the cavity has a difference of $\pi$, and hence a destructive interference occurs when cavity is on resonance. In this graph, transmittance drops to zero when $\delta\lambda/\Delta\lambda_{\text{FWHM}} = 0$ because critical coupling condition ($\tau_{\text{int}} = \tau_{\text{coup}}$)[93] is satisfied. In this condition, the amplitude of mode transmitted from fiber is same as the amplitude mode coupled from the cavity, thus the output wave is completely canceled out. Obviously, minimum transmittance changes as described in Eq. (3.5) when coupling condition is changed.

To understand the impact of the change of coupling condition, I calculated transmittance on resonance for different $\tau_{\text{coup}}/\tau_{\text{int}}$ values as shown in Fig. 3.2(b). In this graph, minimum transmittance $Tr_{\text{min}}$ (i.e. transmittance on resonance) is increased when $\tau_{\text{coup}}$

is larger than $\tau_{\mathrm{int}}$. This is because the amplitude of the mode transmitted from fiber is larger than the amplitude mode coupled from the cavity due to weak coupling between the waveguide and the cavity. This condition is know as "under-coupling condition." On the other hand, minimum transmittance $Tr_{\mathrm{min}}$ is also increased when $\tau_{\mathrm{coup}}$ is smaller than $\tau_{\mathrm{int}}$. This is because the amplitude of the mode coupled from the cavity is larger than the amplitude of the mode transmitted from fiber due to strong coupling between the waveguide and the cavity. This condition is known as "over-coupling condition." Considering discussion here, different transmission spectra is obtained depending on the coupling condition. This fact indicates that it is necessary to carefully adjust the coupling condition when we conduct measurement is conducted.

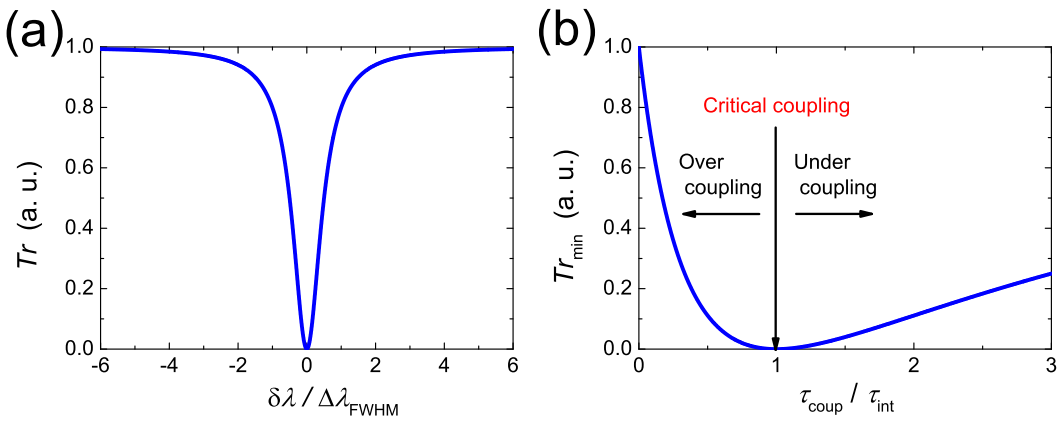


Fig. 3.2: (a) Transmission spectrum of a side-coupled cavity calculated by CMT. Critical coupling condition is assumed. (b) Minimum transmittance for different coupling strength.

### 3.1.2 Add-drop system

Here the model for a side-coupled cavity is applied to an add-drop system. The CMT model for an add-drop system is shown in Fig. 3.3. Note that photon lifetime related to the coupling to drop waveguide $\tau_{\mathrm{drop}}$ is added, and $\tau_{\mathrm{coup}}$ is replaced with $\tau_{\mathrm{bus}}$ (photon lifetime related to the coupling to bus waveguide). For the model in Fig. 3.3, the master equation of CMT for an add-drop system is simply written, as,

$$\frac{\mathrm{d}a}{\mathrm{d}t} = \left(j\omega_0 - \frac{1}{2\tau_{\mathrm{load}}}\right) a + \sqrt{\frac{1}{\tau_{\mathrm{coup}}}} \exp\left(j\theta\right) s_{\mathrm{in}}, \tag{3.6}$$

Note that $\tau_{\mathrm{load}} = (\tau_{\mathrm{int}}^{-1} + \tau_{\mathrm{bus}}^{-1} + \tau_{\mathrm{drop}}^{-1})^{-1}$. In this case output from the drop waveguide $s_{\mathrm{out,drop}}$ is given, as,

$$s_{\mathrm{out,drop}} = \sqrt{\frac{1}{\tau_{\mathrm{drop}}}} \exp(-j\beta d) a \tag{3.7}$$

In contrast to the output from the bus waveguide, there is no input wave in drop-port that interfere with the wave coupled from the cavity. I can simply model $s_{\mathrm{out,drop}}$ by using only the cavity mode $a$ as shown in Eq. (3.7). Here, by employing Eqs. (3.4), (3.6) and (3.7), the transmission of bus and drop waveguides ($Tr_{\mathrm{bus}}$, $Tr_{\mathrm{drop}}$) are obtained, as,

$$Tr_{\mathrm{bus}} = \frac{4\pi^2c^2(\frac{1}{\lambda}-\frac{1}{\lambda_0})^2+\frac{1}{4}\left(\frac{1}{\tau_{\mathrm{int}}}-\frac{1}{\tau_{\mathrm{coup}}}\right)^2}{4\pi^2c^2(\frac{1}{\lambda}-\frac{1}{\lambda_0})^2+\frac{1}{4\tau_{\mathrm{load}}^2}}, \tag{3.8}$$

$$Tr_{\mathrm{drop}} = \frac{\frac{1}{\tau_{\mathrm{bus}}\tau_{\mathrm{drop}}}}{4\pi^2c^2(\frac{1}{\lambda}-\frac{1}{\lambda_0})^2+\frac{1}{4\tau_{\mathrm{load}}^2}}. \tag{3.9}$$

Figure 3.3(b) shows the typical transmittance of bus and drop waveguides as a function of $\delta\lambda/\Delta\lambda_{\mathrm{FWHM}}$. $Q_{\mathrm{int}} = Q_{\mathrm{bus}} = Q_{\mathrm{drop}} = 10^7$ is assumed. The shape of transmission spectrum of a drop waveguide is inverted in Fig. 3.3(b), because there is no input wave in a drop waveguide. Thus destructive interference does not occur unlike a bus waveguide. In addition, the dip in $Tr_{\mathrm{bus}}$ cannot drop to zero while the peak in $Tr_{\mathrm{drop}}$ cannot reach to 1. Under this situation, power inputted into a bus waveguide cannot completely transfer to a drop waveguide; this may be obstacle for achieving high transmittance between bus and drop waveguides. Thus, I analyzed the transmission for different $Q_{\mathrm{bus}}$ and $Q_{\mathrm{drop}}$ values in detail to maximize the transmittance.

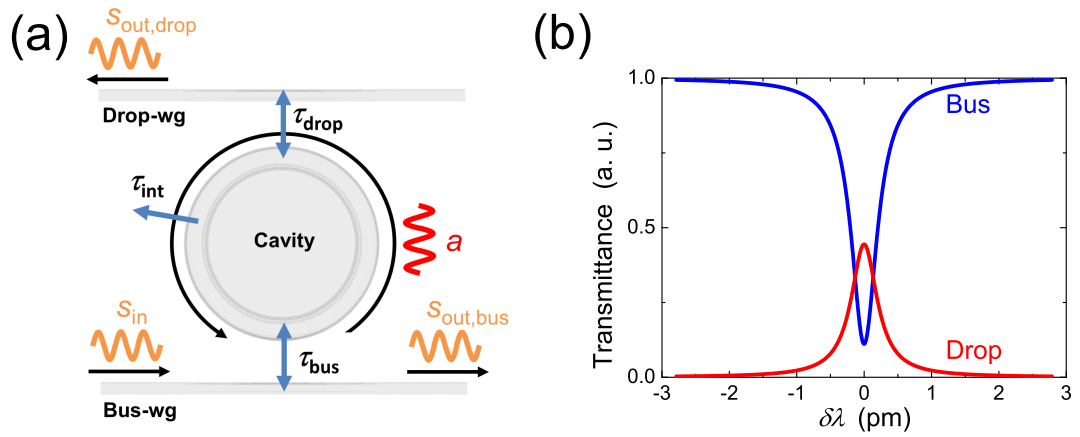


Fig. 3.3: (a) Schematic illustration of the CMT model for an add-drop system. (b) Transmittance of bus and drop waveguides when $Q_{\mathrm{int}} = Q_{\mathrm{bus}} = Q_{\mathrm{drop}} = 10^7$. Blue and red solid lines represent transmittance of bus and drop waveguides, respectively.

Figures 3.4(a) and (b) are the transmittance of the bus and the drop waveguides on resonance. Figure 3.4(c) is the $Q_{\mathrm{load}}$ of the cavity. They are mapped in respect to different $Q_{\mathrm{bus}}$ and $Q_{\mathrm{drop}}$ values. For a side-coupled (an add-drop) system, the transmittance should have small (large) value because the dip (peak) in the spectrum should be deep (high) to obtain high contrast switching.[35] Considering this understanding, it is clear that the condition where $Q_{\mathrm{bus}} \approx Q_{\mathrm{bus}}$, especially $Q_{\mathrm{bus}} = Q_{\mathrm{drop}} \approx 10^5$ is preferred to be used

because transmittance is small for a side-coupled system and is large for an add-drop system as shown in Fig. 3.4(a) and (b). However, it should be noted that low $Q_{\mathrm{bus}}$ and $Q_{\mathrm{drop}}$ results in low $Q_{\mathrm{load}}$ even if $Q_{\mathrm{int}}$ is high as shown in Fig. 3.4(c). Nonlinear effect is difficult to occur when $Q_{\mathrm{load}}$ is low; thus this condition is not suitable for achieving optical switch. There is trade-off between the size of dip/peak and $Q_{\mathrm{laod}}$. This fact must be considered for achieving optical switch in an add-drop system.

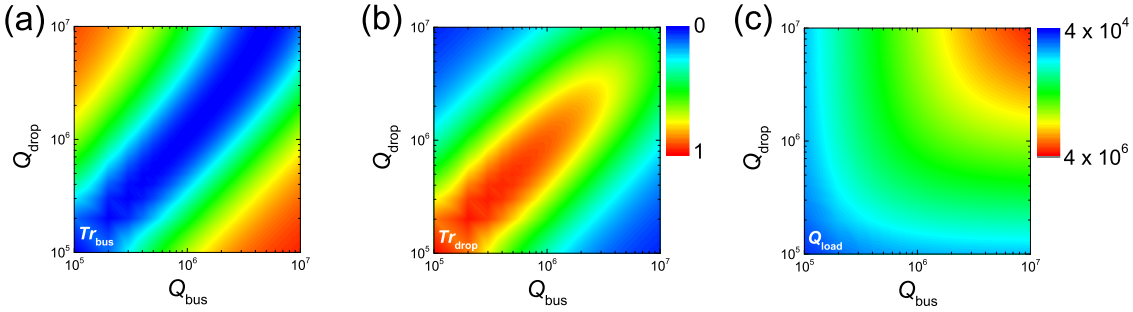


Fig. 3.4: Transmittance of bus (a) and drop (b) waveguides and $Q_{\mathrm{load}}$ for different $Q_{\mathrm{bus}}$ and $Q_{\mathrm{drop}}$ values. Note that $Q_{\mathrm{int}} = 10^7$.

## 3.2 Method to couple light into WGM cavity

To the present, method on coupling the light into microcavity has been intensively studied by many researchers and various methods were proposed.[94,95,83] In this section, I briefly overview some of the several well-known coupling methods. In particular, we will focus on the method based on taper fiber because it is the simplest and the most commonly used method.

The following two points have to be satisfied to couple the light into an optical microcavity: (1) Sufficient overlap and (2) phase-matching of an input wave mode and a cavity mode.[96] Overlap has been considered not only for coupling to WGM cavity but also a conventional directional coupler which consists of two adjacent waveguides.[89] For obtaining sufficient coupling between two waveguides, it is necessary to place these waveguides adjacent. So, (1) is a very straightforward way to couple the light into a WGM cavity. However, in the case of WGM cavity, point (2) is also very important. As mentioned in 2.2, there are large number of modes that have different propagation constants in WGM cavity unlike a single mode waveguide. In this situation, I have to pay attention to propagation constant of input mode[83,81] to excite desired WGM mode (usually fundamental mode). This is because only WGMs with propagation constants close to that of input mode are excited. When I employ a input wave with different propagation constant from that of a fundamental WGM, I cannot excite it. Hence, appropriate control of the propagation constant of the input wave are important for coupling light to WGM cavity. Considering this situation, we explain three methods such as prism coupling method, side-polished fiber method and taper fiber method.

## Prism coupling

Prism coupling method was firstly employed to excite WGMs in microsphere microcavity,.[97] In this scheme, a prism that has higher index than microsphere is placed near a microsphere to excite WGM as shown in Fig. 3.5(a). When the light is reflected on the prism surface with an angle of $\Phi < \sin^{-1}(n_{\mathrm{r}}/n_{\mathrm{p}})$ evanescent wave is generated on the prism surface. Where $n_{\mathrm{c}}$ and $n_{\mathrm{p}}$ are the refractive index of a microsphere cavity and a prism. If propagation constants at the surface is precisely matched to that of a WGM, WGM is efficiently excited. An advantage of this method is the controllability of propagation constant of input wave.[83] It is obvious that the propagation constant can be controlled by adjusting incident angle of the input beam on the prism surface. This advantage is very useful for exciting a desired WGM. On the other hand, there is problems in this scheme that prism is bulky and precise alignment of input beam is required.

## Side-polished fiber

It is clear that optical fiber should be used for easily coupling light into an optical microcavity. However, commercial single mode fiber has a cladding layer, and there is no evanescent field on the surface of the fiber. To use the evanescent field of an optical fiber, side-polished fiber method was proposed by N. Dubreuil *et al*.[95] In this scheme, the clad is mechanically eroded ("side-polishing") and the core is exposed as shown in Fig. 3.5(b). As a result, evanescent field on the surface of the core is able to be used. This method is superior to the prism coupling method in terms of controllability. On the other hand, side-polished fiber has a core with fixed diameter ($3-5$ $\mu$m), thus propagation constants of input mode cannot be controlled.[83] This means that it is difficult to selectively excite a desired WGM mode by using side-polished fiber.

## Taper fiber

Currently taper-fiber coupling method is widely used, which was originally developed by J. Knight *et al*.[83] By heating and stretching a commercial single mode fiber, optical fiber with a thin waist (diameter of $< 1$ $\mu$m) can be easily obtained. Nearly no additional loss is induced after tapering if adiabatic condition is satisfied during tapering process.[98] In the tapered region, evanescent wave is excited due to its thin diameter. Thus WGMs is excited by using taper-fiber. The advantage of this method is the tunability of propagation contrast of input mode. In comparison with the side-polished fiber method which has a fixed diameter, we can control diameter of the tapered region by adjusting tapering condition[*b]. Therefore, propagation constant of taper-fiber can be tuned. Considering this excellent advantage, we decided to use taper-fiber coupling method to excite WGM.

[*b] Practically propagation constant of taper fiber is controlled by the position of taper fiber where WGM cavity couples. Taper fiber has gradually changing diameter along with its axis. This indicates that we can control propagation constant of input mode by adjusting coupling position.

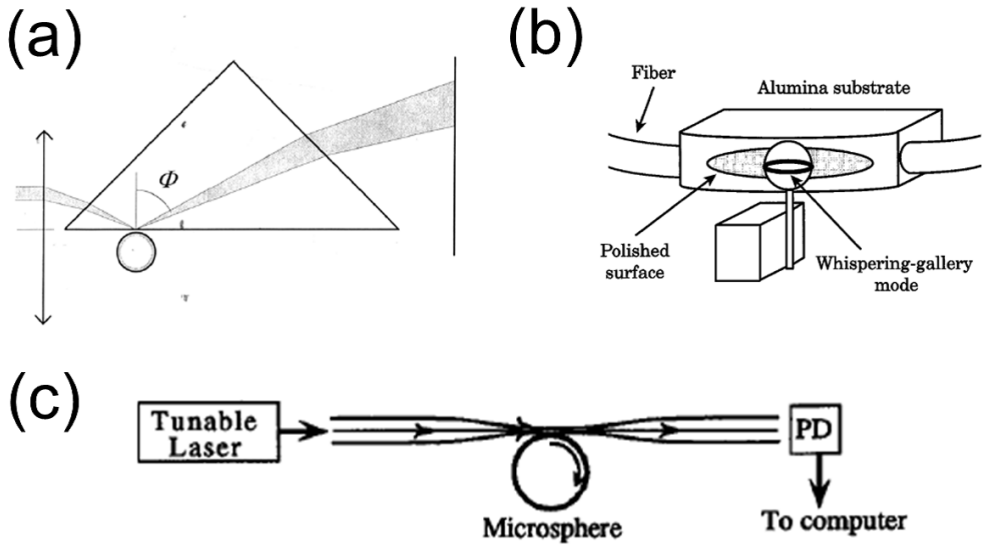


Fig. 3.5: Schematic illustrations of (a) prism coupling [Reprinted with permission from M. Gorodetsky and V. Ilchenko, " High-Q optical whispering-gallery microresonators - precession approach for spherical mode analysis and emission patterns with prism couplers, " Opt. Commun. **113**, 133-143 (1994). ©1994 Elsevier.], (b) side-polished coupling [Reprinted with permission from N. Dubreuil, J. Knight, D. Leventhal, V. Sandoghdar, J. Hare, and V. Lefevre, "Eroded monomode optical-fiber for whispering-gallery made excitation in fusedsilica microspheres," Opt. Lett. **20**, 813-815 (1995). ©1995 Optical Society of America.] and (c) taper-fiber coupling methods [Reprinted with permission from J. Knight, G. Cheung, F. Jacques, and T. Birks, " Phase-matched excitation of whispering-gallery-mode resonances by a fiber taper, " Opt. Lett. **22**, 1129-1131 (1997). ©1997 Optical Society of America.].

## 3.3 Fabrication of taper fiber

In this section, the fabrication of an optical taper fiber is described[*c]. First, commercial single mode fiber is cut off by about 1.5 m. Covering of center region of optical fiber is removed by a stripper and carefully cleaned by Acetone. It become a main cause of rupture of taper fiber during tapering process if there are contaminants remain on the surface of bare optical fiber. This area will be heated and tapered. Before starting tapering process, couplers are connected to both facets of the optical fiber to monitor the transmittance during tapering process. Note that insertion loss due to couplers are typically $1 \sim 2$ dB. Then tapering process is started. We use a torch with $O_2$ and $C_3H_8$ gas. Tapering condition such as the heating time, swinging amplitude of torch and pulling rate are pre-set in pulling machine (Fig. 3.6(a)). Thus this process has high reproducibility[*d]. In particular, the swinging amplitude and the pulling rate are important because they directly relate to the length of tapering region. Optimization of shape of tapering region is the key for fabricating low-loss taper fiber. Local taper angle has to satisfy adiabatic condition[98] for obtaining low-loss taper fiber, as,

$$\left|\frac{\mathrm{d}r}{\mathrm{d}z}\right| \leq \frac{r(\beta_1 - \beta_2)}{2\pi}, \tag{3.10}$$

where $r$, $z$, $\beta_1$ and $\beta_2$ are the local taper radius at the position $z$, local propagation constants of $HE_{11}$ and $HE_{12}$. Failure of this condition result in additional loss due to the propagation loss of taper fiber. During tapering, a taper fiber exhibit multi mode propagation because core and cladding are mixed and they can be regarded as a core with large diameter. Figure 3.6(b) shows transmittance through the fiber while being tapered. As shown in the figure, large oscillation occurs in "multi-mode" region. This is due to interference between multiple optical modes in the optical fiber. Around 5 min. the oscillation disappears because the taper fiber returns to "single mode" regime. In this regime taper fiber is thin enough to support one fundamental mode and has a diameter of approximately 1 $\mu$m. I fabricate a taper fiber with a diameter of around 1 $\mu$m, which is a condition required for achieving high ideality,[73] by stopping tapering process when taper fiber become single mode again. After tapering, we move the taper fiber to our measurement system. Fiber holders which are used in the taper fiber fabrication system and measurement system are the same and we can attach it to the measurement system directly. This design is beneficial for avoiding rupture after fabrication. As shown in Fig. 3.6(b), the tapering loss is very small (5 %)[*e]. Therefore, it is possible to demonstrate switches with nearly no insertion loss optical switches by employing taper fiber.

[*c] Our setup for fabrication of taper fiber was originally developed by the author's colleague Y. Ogawa.

[*d] The tapering condition was optimized by the author's colleague T. Kato.

[*e] Note that this value excludes splice loss. In our setup, there is typically $1 \sim 2$ dB insertion loss depending on the splice condition. This loss is not problem because it can be eliminated by using fiber fusion splicing in practice

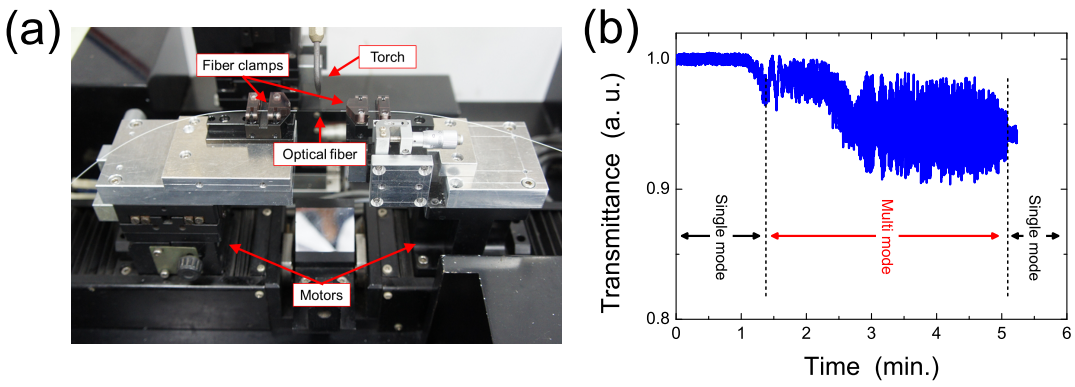


Fig. 3.6: (a) Picture of fiber tapering system. (b) Transmittance through the fiber while being tapered.

## 3.4 Measurement of a silica toroid microcavity

### 3.4.1 Measurement system

In this subsection, the system which is used for testing a silica toroid microcavity is described[*f]. The picture of the system is shown in Fig. 3.7(a). The system can be separated into four parts such as (1) the upper camera system, (2) the side camera system, (3) the device holding system and (4) the taper fiber holding system. (1) The upper camera is vertically attached to the base. It is on $xy$ manual stage and $z$ automatic stage with a resolution of 10 nm. This camera is used for recognizing the horizontal distance between a silica toroid microcavity and a taper fiber (Fig. 3.7(b). (2) The side camera is on a $xyz$ manual stage. This camera can capture the vertical distance between a silica toroid microcavity and a taper-fiber (Fig. 3.7(c)). (3) Device holding system is on $xyz$ automatic stage. As shown later, the distance between a microcavity and a taper fiber is very important for obtaining optimal coupling condition. A resolution of $< 100$ nm is required to adjust the coupling accurately. Thus our stage has a resolution of 10 nm. (4) Taper-fiber holding system is composed of fiber holder (as mentioned in 3.3), $x$ manual stage and a gonio stage. The fiber holder is removable, and it can also be attached to a taper-fiber fabrication system. The $x$ manual stage is used to adjust the position along the fiber axis. Mobility in this direction is necessary for controlling the diameter of the taper-fiber coupled to a microcavity. The gonio stage is used for carefully aligning taper-fiber parallel to a chip. A silica toroid microcavity is only few-tens of $\mu$m high from a substrate. So taper-fiber will easily touch a substrate when I do not controll the inclination of taper-fiber. Finally, it should be noted that all the system is on the vibration-isolation stage, and it is covered by plastic case to block the air flow. This is because vibration and air flow result in unstable coupling condition.

[*f]Our measurement system was originally developed by my colleague Y. Ogawa and upgraded by other colleagues several times.

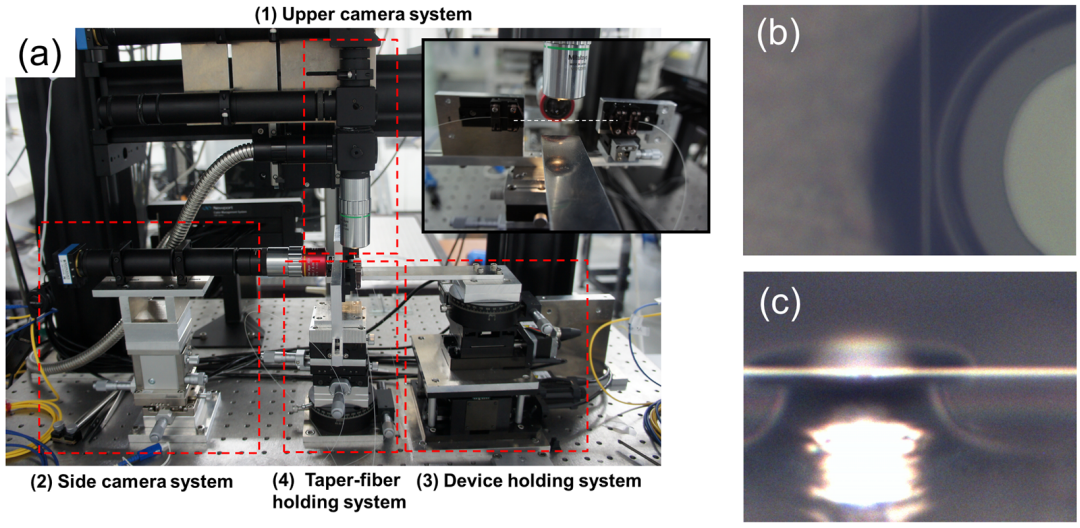


Fig. 3.7: (a) The system used for testing optical microcavity. The inset shows the side view of the system. Taper-fiber is indicated by the white dashed line. (b) and (c) are pictures taken by (b) the upper and the side camera, respectively.

### 3.4.2 Characterization of $Q$ factor

As mentioned in 1.3.1, $Q$ is very important to characterize an optical microcavity. According to Eqs. (1.7) and (1.8), $Q$ is calculated by using full-width half-maximum resonant spectra $\Delta\lambda_{\mathrm{FWHM}}$ and a photon lifetime $\tau_{\mathrm{load}}$. In this section, I discuss two experimental different experimental methods for characterizing $Q$.

#### Measurement based on a resonant spectra

According to Eq. (3.5), resonant spectrum has typically a Lorentz-shape[*g]. Hence by fitting resonant spectra by Lorentz function and measuring full-width half-maximum of the fitted curve, $Q$ of a microcavity is obtained.

Figure 3.8(a) is the experimental setup for measuring $Q$ of a silica toroid microcavity using a resonant spectrum. I sweep output wavelength of a tunable laser diode (TLD) and measure the transmittance by using power meter (PWM) simultaneously. When the output wavelength of TLD is the same as the resonant wavelength of microcavity, transmittance drops. In this way, I obtain resonant transmission spectra. It should be noted that resonant wavelength is different for input polarization (see Eq. (2.23)), thus controlling input polarization is very important for exciting a desired WGM. Considering this fact, polarization controller (PC) is placed before the device under testing (DUT) as shown in Fig. 3.8(a).

Figure 3.8(b) shows a typical resonant spectrum measured by experimental setup

[*g]If there is a nonlinear effect such as TO effect[99] or Fano resonance,[100] Lorentz-shape is deformed. Deformation based on TO effect will be discussed in D.

shown in Fig. 3.8(a). Black and red solid lines represent the measured and fitted curves. As a result of Lorentz fitting, I found that loaded $Q$ factor $Q_{\mathrm{load}}$ is obtained as $5.0 \times 10^6$. This spectrum doesn't seems to be measured in "critical coupling" condition because the transmittance minimum does not drop to zero. However, the reason why the minimum transmittance does not drop to zero is not improper coupling condition but it is the limited wavelength resolution of measurement system. As mentioned above, resonant spectra is obtained by sweeping wavelength of TLD. In this setup, wavelength resolution depends on wavelength sweep speed and response time of PWM. Our laser has slowest sweep speed of 1 nm/s and PWM has shortest response time of 100 $\mu$s. This allows me to measure with the wavelength resolution of down to 0.1 pm, which corresponds to $Q$ of $1.55 \times 10^7$. Thus, when I measure a resonant spectra with $Q$ of around $10^7$, there is a risk that a resonant spectra cannot be correctly measured. For accurate measurement of the $Q$ factor, it is necessary to employ ring down measurement which will be described in the next section[*h].

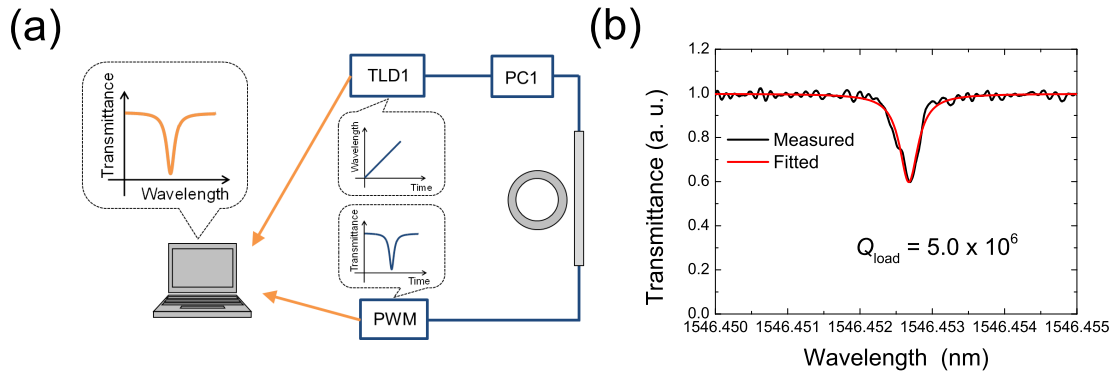


Fig. 3.8: (a) Experimental setup for measuring $Q$ of a silica toroid microcavity using a resonant spectra. (b) Typical resonant spectra of a silica toroid microcavity. Black and red solid lines are measured and fitted curves, respectively. Estimated $Q_{\mathrm{load}}$ is $5.0 \times 10^6$

### Measurement based on a ring down method

For accurately measuring $Q$ of an optical cavity, ring down method[60,101,38] is commonly employed. By using this method, cavity photon life time can be directly measured. Here I assume a cavity which is fully charged by input light to explain concept of ring down method. In this situation, the light energy in the cavity reaches static condition due to the continuously inputted light. When input light is suddenly turned off, the light energy in the cavity $U_{\mathrm{cavity}}$ decays in proportion to $\exp(-t/\tau_{\mathrm{load}})$, and then this decaying behavior is reflected on the output power from the cavity. Therefore, cavity photon lifetime $\tau_{\mathrm{load}}$ can be inferred by detecting output signal.

[*h]Besides ring down method, I can measure accurate $Q$ factor by fine tuning laser wavelength by applying external voltage to the piezo mounted end-mirror. See Fig. 3.5 in M. Pöllinger.[38]

Figure 3.9(a) shows the experimental setup for ring down method. CW signal is outputted from TLD, and is modulated by electro-optic modulator (EOM). Output signal is detected by optical sampling oscilloscope (OSO) and PWM. And then I can measure accurate $\tau_{\mathrm{load}}$ (i.e. $Q_{\mathrm{load}}$) by analyzing detected signal.

Figure 3.9(b) shows the typical signal obtained by ring down measurement. When input signal is turned off (at $t \approx 60$ ns), output signal quickly recovers to the input value. And then, output signal decays exponentially. By fitting this decaying curve, I can determine $Q_{\mathrm{load}}$ of $6.4 \times 10^6$. It should be noted that measured $Q_{\mathrm{load}}$ are similar to that in Fig. 3.8, but minimum transmittance is significantly different. This is due to the limitation of measurement based on a resonant spectra as described above. Therefore, I have to use ring down method for achieving accurate measurement of $Q$ and transmittance, we have to use ring down measurement.

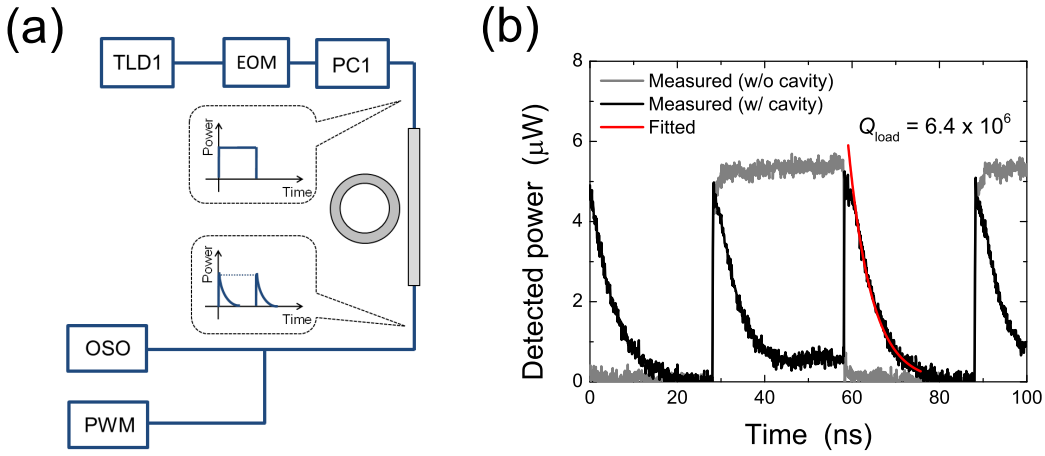


Fig. 3.9: (a) Experimental setup for ring down measurement. (b) Output signal obtained by the ring down method. Gray, black and red solid lines are measured signal with and without cavity and fitted curves, respectively. Estimated $Q_{\mathrm{load}}$ is $6.4 \times 10^6$.

### 3.4.3 Optimization of coupling

As mentioned in previous sections, I have to pay attention to the coupling condition for accurately measuring the performance of a microcavity. In general the coupling condition is determined by polarization of input wave and diameter of taper-fiber. So, here importance of these conditions are described by referring some experimental data.

#### Polarization

Polarization of input wave is important for observing zero-transmittance at the output. As shown in Eq. (2.23), different WGMs have different polarizations. Thus polarization of input wave has to be carefully controlled for exciting the desired WGM. If polarizations of input wave and WGM are matched, the waves transmitted from the taper-fiber and

outputted from the cavity are completely interfered. As a result transmittance drops to zero when the critical coupling condition is satisfied. On the other hand, if the polarizations are not matched, only a part of the transmitted wave and the outputted wave are interfered. This results that some power remains at the output even when the critical coupling condition is satisfied. Therefore, carefully controlling the polarization of input wave is important for obtaining zero-transmittance.

In reality, the polarization of the desired WGM is unknown and the input polarization is easily perturbed while propagating in the taper-fiber. As a result of these problems, it is necessary to adjust polarization of input wave monitoring the change of output power. When the input polarization is matched to that of the WGM of interest, the output disappears; this behavior tells us that the optimal polarization is obtained.

### Diameter of taper fiber

Diameter of taper fiber affects two important factors of the coupling such as "ideality[73]" and the propagation constant of the input wave. Ideality proposed in M. Spillane *et al.*[73] should be considered for optimizing coupling between a taper-fiber and a cavity. As mentioned in 3.3, when the diameter of tapered region of taper-fiber is thick, there are a fundamental mode and several higher-order modes in the tapered region (multi modes). In such a situation, the part of the light outputted from the cavity can couple into higher-order mode in a taper fiber. However higher-order mode cannot reach the output of the taper-fiber because only a fundamental mode can propagate though the single mode regime. Thus, the light coupled into the higher-order mode is dissipated during propagation in the single mode regime. If all the light outputted from the cavity couples to the fundamental mode in the taper fiber, ideality $I$ takes unity. This understanding can be verified by observing the transmittance in strongly over-coupling regime. If ideality is unity (diameter of taper-fiber is sufficiently thin), transmittance reach unity as shown in Fig. 3.2(b). However, if ideality is smaller than "1," transmittance does not recover to unity even in over-coupling regime because the light coupled to the higher-order mode is dissipated during the single mode region. So, I can confirm whether ideality is unity or not by measuring the transmittance in strongly over-coupling regime.

For exciting the desired WGM, obviously the input wavelength must be matched to the resonant wavelength (i.e. resonant condition). However, rigorously speaking, it is also necessary to match the propagation constant of input mode to that of the desired WGM (i.e. "Phase-matching condition[83]"). If phase-matching condition fails to be satisfied, WGM cannot be efficiently excited. Therefore, controlling propagation constant is the key to obtain efficient coupling between the cavity mode and input mode. In experiments, the propagation constant is usually controlled by the adjusting the diameter of the taper fiber. It is intuitive that the change of the diameter results in the changes in the length of evanescent field around taper-fiber, and then the propagation constant is modified.

The influence from phase-matching can be seen in the mode-selectivity and the transmittance in the strongly over-coupling regime. As mentioned in 2.2.1, different WGMs have different propagation constants. Hence only WGM whose propagation constant matches that of the input mode is excited, and it is possible to excite only the desired WGM by carefully adjusting the diameter of a taper fiber. In addition, the trans-

mittance does not recover to unity even under strongly over-coupling condition when phase-matching condition is not satisfied. If phase-matching condition is satisfied, the transmittance completely recovers as shown in Fig. 3.2(b) because the light outputted from cavity is much larger than that transmitted without coupling to the cavity under over-coupling condition. On the other hand, if phase-matching condition is not satisfied, the light outputted from the cavity is not large enough[*i] to dominate that transmitted without coupling, thus the transmittance cannot recover.

### Experimental verification

Here I experimentally confirm the understandings obtained above. First, for confirming the mode-selectivity depending on the diameter of taper-fiber, I measured resonant spectra for a different diameter of a taper fiber (i.e. different input propagation constants). Note that polarization is carefully adjusted before starting the measurement. The schematic of experimental procedure is shown in Fig. 3.10(a). The diameter of taper is dependent on $x$ position as shown in Fig. 3.10, thus we can control input propagation constant by changing the position of taper fiber which is coupled to a microcavity. The results are shown in Fig. 3.10(b). It should be noted that the distance between the cavity and the taper-fiber is fixed. Figure 3.10(b) clearly shows that measured resonant spectrum are changed depending on the diameter of the taper fiber. This is because each mode shown in the figure has different propagation constant. Therefore, it is necessary to choose the diameter of the taper-fiber carefully to excite a desired mode.

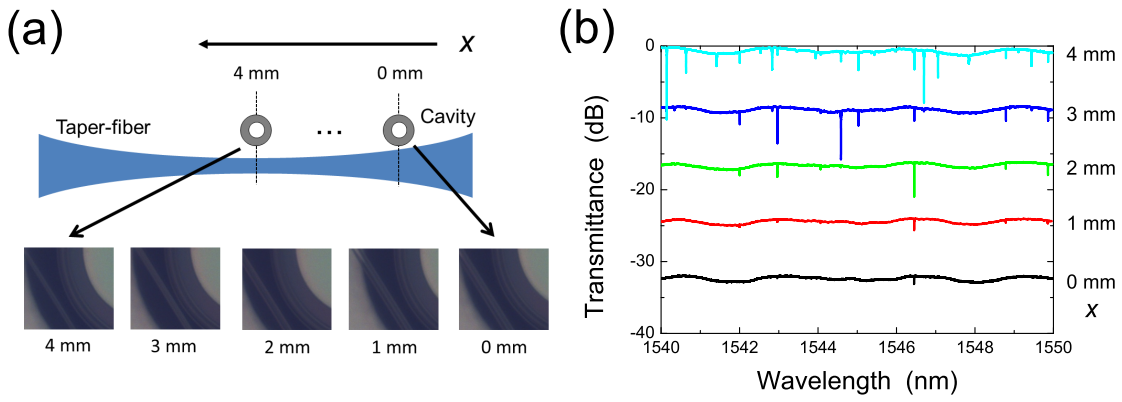


Fig. 3.10: (a) Method on adjusting the diameter of taper fiber which is coupled to a microcavity. (b) Measured resonant spectra as a function of a taper diameter. The distance between the cavity and the taper fiber is fixed at 700 nm for the all cases.

Next, I measure transmission spectrum for different distances between the cavity and the taper-fiber. The schematic of experiment is shown in Fig. 3.11(a). I measured resonant spectrum of a microcavity for a fixed taper-fiber diameter by changing the distance between the cavity and the taper-fiber from 1.6 $\mu$m to 0 $\mu$m. As shown in

[*i] This is because small part of the input light can couple into the cavity in this condition.

Fig. 3.2(b), the transmittance is minimum at a critical coupling point. In addition, the transmittance should recover to unity in strongly over-coupling regime if ideality is unity and phase-matching condition is satisfied. The results are shown in Fig. 3.11(b). Note that "$d$" is the distance between the cavity and the taper-fiber. When $d$ is around 1.6 $\mu$m, there is no excited mode because it is deeply under-coupled condition. When $d$ is smaller, several modes appear in the resonant spectra because it is closer to the critical coupling condition. And then these modes vanish when $d$ is further decreased; this is direct evidence that ideality is unity and phase-matching condition is satisfied. By the way, here as can be seen in Fig. 3.11, different modes have different coupling behavior. For example, the dips indicated by the black arrows recover to 1 before the fiber contact to the cavity. On the other hand, the dips indicated by the orange arrows do not recover to 1 even when the cavity and taper-fiber is contacted. This is due to the different phase-matching conditions as mentioned above. In addition, the modes indicated by the same color of arrows behave the same in respect ot the gap distance in Fig. 3.11(b). This indicates that these mode have similar propagation constants (i.e. similar $l$ and $m$ numbers). Therefore, for characterizing the mode number, it is effective to measure the dependency of the transmittance on the cavity-fiber distance.

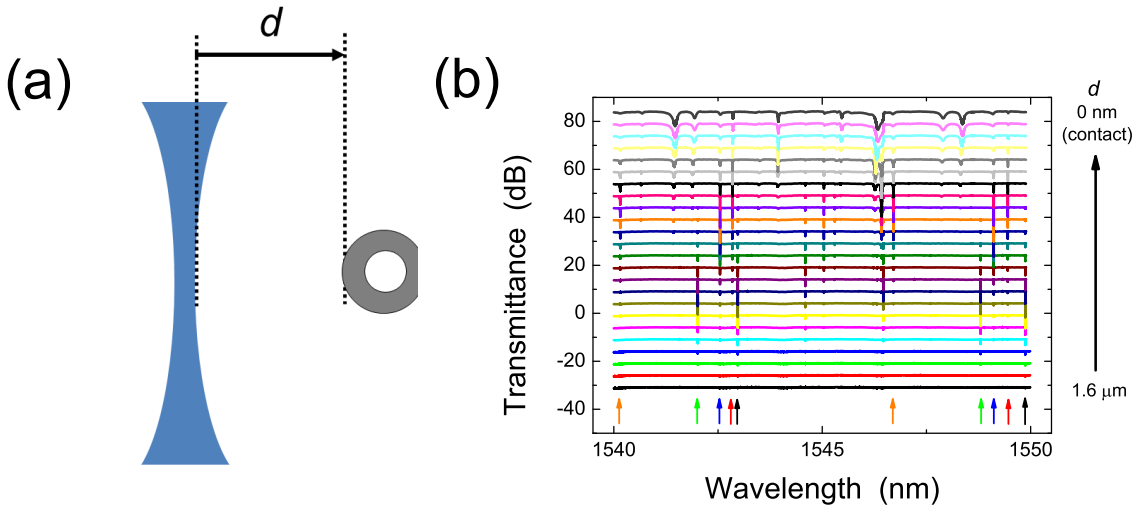


Fig. 3.11: (a) Schematic illustration on how I adjust the distance between cavity and taper fiber. (b) Measured resonant spectra as a function of distance between the cavity and the taper fiber.

In summary, I showed that the dependency of the transmittance on (1) the diameter of the taper-fiber and (2) the polarization need to be carefully adjusted for optimizing the cavity-fiber coupling.

# Chapter 4

# Optical Kerr switch in a side-coupled system

In this section, results on optical switching operation with a side-coupled system is described. This is the one of the main parts of this thesis. First, two-wavelength scheme is described, which is used in this section. Next, results on optical switch based on TO effect are shown. Then, result of optical switch based on Kerr effect are presented. Finally, I summarize the result obtained by switching experiment in a side-coupled system.

## 4.1 Principle of microcavity-based switch - "two-wavelength" scheme

### 4.1.1 Qualitative understanding

Before entering the part of optical switch, here I explain principle of microcavity-based switch (two-wavelength scheme). As mentioned in 1.3.2, optical switching is induced by wavelength shifting based on the refractive index change. However, principle of the microcavity-based switches is a little more complicated than that.

For achieving optical switch in a microcavity, usually two-wavelength scheme is employed. Schematic image of two-wavelength scheme is shown in Fig. 4.1. I use two light such as "control" and "signal" lights as such shown in Fig. 1.1. Control light is the light that "modulates" signal light, on the other hand, signal is the light that "is modulates" by control light. As shown in the upper graph of Fig. 4.1, wavelengths of control and signal light are set to different resonances, which are named as a control mode and a signal modes, respectively. In general, control light is very weak, thus it does not induce any nonlinearities in a microcavity. On the other hand, control light is strong enough to induce nonlinearity, thus it changes refractive index and eventually the resonant wavelength is shifted as shown in the lower graph of Fig. 4.1. In this situation, refractive index $n$ is shared by both control and signal modes (i.e. XPM), thus probe mode also experience the refractive index change induced by control light, and then it is also shifted. As a result, signal light is switched due to the shift of signal mode induced by control light. Eventually control light switches probe light. This is the two-wavelength scheme

which is used in microcavity-based switch. It should be noted that output control light is filtered out to measure only signal light after switching.

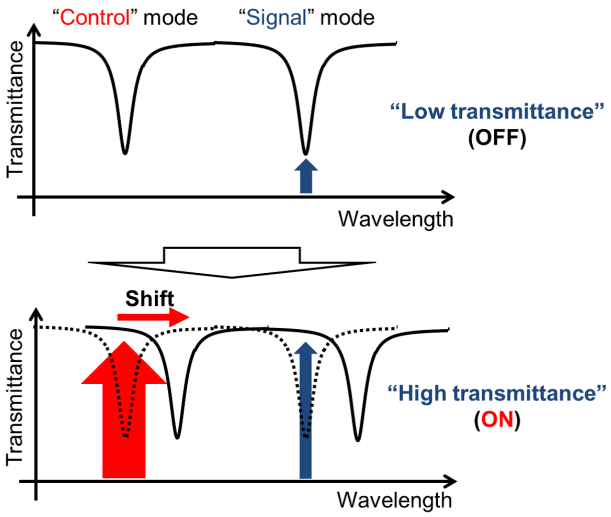


Fig. 4.1: Schematic illustration of two-wavelength scheme.

### 4.1.2 Quantitative understanding

Here, the principle of "two-wavelength" scheme is qualitatively discussed. First, I obtain the resonant wavelength shift of a control mode. Regardless of which effects (TO or Kerr) are used, the resonant wavelength shift is caused by the light energy stored in the microcavity. The relation between the light energy in the cavity $U_{\mathrm{cavity}}$ and the input control power $P_{\mathrm{in}}^{\mathrm{cont}*\mathrm{a}}$ is calculated by using Eq. (3.2), as,

$$U_{\mathrm{cavity}} = \frac{\lambda_0 Q_{\mathrm{load}}^{\mathrm{cont}}}{\pi c} P_{\mathrm{in}}^{\mathrm{cont}}. \tag{4.1}$$

It should be noted that I assume the critical coupling condition ($Tr_{\mathrm{min}} = 0$) at resonance ($\lambda = \lambda_0$). However, rigorously speaking, Eq. (4.1) should consider the effect of the polarization. Every WGMs have their own polarizations, thus I need to control the input polarization to them. However, in reality, it is difficult to match both polarizations, thus a part of the input light cannot be coupled whose polarization do not match to that of the WGM; this results non-zero finite transmittance even if the critical coupling condition is satisfied. Thus, $P_{\mathrm{in}}^{\mathrm{cont}}$ in Eq. (4.1) is replaced by using the relation $P_{\mathrm{in,match}}^{\mathrm{cont}} = P_{\mathrm{in}}^{\mathrm{cont}} - P_{\mathrm{in,unmatch}}^{\mathrm{cont}}$ where $P_{\mathrm{in,match}}^{\mathrm{cont}}$ and $P_{\mathrm{in,unmatch}}^{\mathrm{cont}}$ are the input control powers which is

[*a] The light energy induced by the signal light is ignored because the input signal power is much lower than the input control light.

coupled and is not coupled to the desired WGM, as,

$$U_{\mathrm{cavity}} = \frac{\lambda_0 Q_{\mathrm{load}}^{\mathrm{cont}}}{\pi c}\left(1 - Tr_{\mathrm{min}}^{\mathrm{cont}}\right) P_{\mathrm{in}}^{\mathrm{cont}}. \tag{4.2}$$

Note that $P_{\mathrm{in,unmatch}}^{\mathrm{cont}}$ can be written as $Tr_{\mathrm{min}}^{\mathrm{cont}} P_{\mathrm{in}}^{\mathrm{cont}}$ under the critical coupling condition.

Next, I show that the resonant wavelength shift of control mode induced by the TO and Kerr effects ($\delta\lambda_{\mathrm{cont}}^{\mathrm{TO}}$, $\delta\lambda_{\mathrm{cont}}^{\mathrm{Kerr}}$) is calculated by the light energy $U_{\mathrm{cavity}}$. By using Eq. (1.11), the resonant wavelength shift induced by TO effect $\delta\lambda_{\mathrm{cont}}^{\mathrm{TO}}$ is written, as,

$$\delta\lambda_{\mathrm{cont}}^{\mathrm{TO}} = \lambda_0 \frac{\Delta n_{\mathrm{TO}}}{n} = \lambda_0 \xi \Delta T, \tag{4.3}$$

where $\Delta T$ is the temperature change of the microcavity. In addition, $\Delta T$ is in proportion to the thermal energy accumulated in the microcavity $U_{\mathrm{thermal}}$ as,

$$\Delta T = \frac{U_{\mathrm{thermal}}}{C\rho V}, \tag{4.4}$$

where $C$, $\rho$ and $V$ are the heat capacity, the density of the material and the volume of the cavity, respectively. Here I assume that $U_{\mathrm{thermal}}$ can be expressed by using the following differential equation, given as,

$$\frac{\mathrm{d}U_{\mathrm{thermal}}}{\mathrm{d}t} = -\frac{1}{\tau_{\mathrm{relax}}} U_{\mathrm{thermal}} + \frac{1}{\tau_{\mathrm{abs}}} U_{\mathrm{cavity}}, \tag{4.5}$$

where $\tau_{\mathrm{diff}}$ is the thermal relaxation time. Equation (4.5) describes that the heat $U_{\mathrm{thermal}}$ is generated by absorbing $U_{\mathrm{cavity}}$ at a rate of $\tau_{\mathrm{abs}}^{-1}$ but is dissipated due to relaxation with the rate of $\tau_{\mathrm{relax}}^{-1}$. Under the static condition ($U_{\mathrm{cavity}}$ is constant and $\frac{\mathrm{d}U_{\mathrm{thermal}}}{\mathrm{d}t} = 0$), the relation between $\Delta T$ and $U_{\mathrm{cavity}}$ is written by using Eqs. (4.4) and (4.5), as,

$$\begin{aligned} \Delta T &= \frac{\tau_{\mathrm{relax}}}{C\rho V \tau_{\mathrm{abs}}} U_{\mathrm{cavity}} = \frac{C_{\mathrm{heat}}}{\tau_{\mathrm{abs}}} U_{\mathrm{cavity}}, \\ C_{\mathrm{heat}} &= \frac{\tau_{\mathrm{relax}}}{C\rho V}. \end{aligned} \tag{4.6}$$

Therefore, by using Eqs. (4.1), (4.3) and (4.6), I can estimate the resonant wavelength shift induced by TO effect $\delta\lambda_{\mathrm{cont}}^{\mathrm{TO}}$ by using $P_{\mathrm{in}}^{\mathrm{cont}}$, as,

$$\delta\lambda_{\mathrm{cont}}^{\mathrm{TO}} = \frac{2\lambda_0 \xi C_{\mathrm{heat}} Q_{\mathrm{load}}^{\mathrm{cont}}}{Q_{\mathrm{abs}}}\left(1 - Tr_{\mathrm{min}}^{\mathrm{cont}}\right) P_{\mathrm{in}}^{\mathrm{cont}}. \tag{4.7}$$

By using Eq. (4.7), I can obtain the resonant wavelength shift induced by TO effect.

Next, I derive the equation, that will give relation between the resonant wavelength shift induced by Kerr effect $\delta\lambda_{\mathrm{cont}}^{\mathrm{Kerr}}$ and the input control input power $P_{\mathrm{in}}^{\mathrm{cont}}$. According to Eq. (1.13), (4.3) and W. Yoshiki and T. Tanabe,[35] $\delta\lambda_{\mathrm{cont}}^{\mathrm{Kerr}}$ is written, as,

$$\delta\lambda_{\mathrm{cont}}^{\mathrm{Kerr}} = \frac{\lambda_0}{n_0}\Delta n_{\mathrm{Kerr}} = \frac{\lambda_0}{n_0}\iint \Delta n_{\mathrm{Kerr}}(r,z)\tilde{I}(r,z)dS, \tag{4.8}$$

where $\Delta n_{\mathrm{Kerr}}(r,z)$, $\tilde{I}(r,z)$ are the distributions of refractive index change induced by Kerr effect and normalized[*b] WGM intensity. Eq. (4.8) considers spatial overlap between the distributions of the refractive index change and the WGM. In addition, $\Delta n_{\mathrm{Kerr}}(r,z)$ is calculated by the following equation, given as,

$$\Delta n_{\mathrm{Kerr}}(r,z) = \frac{2n_2 c}{n_0} u_{\mathrm{cavity}}(r,z) = \frac{n_2 c}{n_0 \pi R} U_{\mathrm{cavity}} \tilde{I}(r,z), \tag{4.9}$$

where $u_{\mathrm{cavity}}(r,z) = U_{\mathrm{cavity}}/(2\pi R) \cdot \tilde{I}(r,z)$ is the light energy distribution in the cross-section of the cavity.[35] Therefore, by combining Eqs. (4.2), (4.8) and (4.9), I derive an equation on $\delta\lambda_{\mathrm{cont}}^{\mathrm{Kerr}}$, as,

$$\delta\lambda_{\mathrm{cont}}^{\mathrm{Kerr}} = \frac{\lambda_0^2 n_2 Q_{\mathrm{load}}}{n_0^2 \pi R} \left(1 - Tr_{\mathrm{min}}^{\mathrm{cont}}\right) P_{\mathrm{in}}^{\mathrm{cont}} \iint \tilde{I}^2(r,z) \mathrm{d}S. \tag{4.10}$$

Here, I obtain the change in the transmittance of the signal light induced by the control light. As described before, the wavelength shift of the control mode reflects on the wavelength shift of the signal mode, thus the wavelength shift of signal mode$\delta\lambda_{\mathrm{probe}}$ is written, as,

$$\delta\lambda_{\mathrm{sig}} = \delta\lambda_{\mathrm{cont}}^{\mathrm{TO}} + 2\delta\lambda_{\mathrm{cont}}^{\mathrm{Kerr}}. \tag{4.11}$$

I multiplied $\delta\lambda_{\mathrm{cont}}^{\mathrm{Kerr}}$ by "2" because this is an XPM modulation as described in 2.3. According to Eq. (3.4) and considering the polarization, output signal power $P_{\mathrm{out}}^{\mathrm{signal}}$ is described by the following equation, given as,

$$\begin{aligned} P_{\mathrm{out}}^{\mathrm{sig}} &= \frac{4\pi^2 c^2 \left(\frac{1}{\lambda_0+\delta\lambda_{\mathrm{sig}}} - \frac{1}{\lambda_0}\right)^2}{4\pi^2 c^2 \left(\frac{1}{\lambda_0+\delta\lambda_{\mathrm{sig}}} - \frac{1}{\lambda_0}\right)^2 + \left(\frac{\pi c}{\lambda_0 Q_{\mathrm{load}}^{\mathrm{sig}}}\right)^2} P_{\mathrm{in,match}}^{\mathrm{sig}} + P_{\mathrm{in,unmatch}}^{\mathrm{sig}}, \\ P_{\mathrm{in}}^{\mathrm{sig}} &= P_{\mathrm{in,match}}^{\mathrm{sig}} + P_{\mathrm{in,unmatch}}^{\mathrm{sig}}. \end{aligned} \tag{4.12}$$

Note that I assume the critical coupling condition is satisfied and the initial input control wavelength is tuned to the resonance. Eq. (4.12) shows that if wavelength of signal mode is shifted ($\delta\lambda_{\mathrm{sig}} > 0$), the signal output $P_{\mathrm{out}}^{\mathrm{signal}}$ is also changed. As a result, the signal output is modulated by the control input. Therefore, Eq. (4.12) describes the switching operation induced by Kerr and TO effects. Here, by using the relation $P_{\mathrm{in,match}}^{\mathrm{sig}} = (1 - Tr_{\mathrm{min}}^{\mathrm{sig}}) P_{\mathrm{in}}^{\mathrm{sig}}$ and $P_{\mathrm{in,unmatch}}^{\mathrm{sig}} = Tr_{\mathrm{min}}^{\mathrm{sig}} P_{\mathrm{in}}^{\mathrm{sig}}$, I obtain the switching contrast $\eta = Tr^{\mathrm{sig}} - Tr_{\mathrm{min}}^{\mathrm{sig}} = P_{\mathrm{out}}^{\mathrm{sig}}/P_{\mathrm{in}}^{\mathrm{sig}} - Tr_{\mathrm{min}}^{\mathrm{sig}}$, give as,

$$\eta = \frac{4\pi^2 c^2 \left(\frac{1}{\lambda_0+\delta\lambda_{\mathrm{sig}}} - \frac{1}{\lambda_0}\right)^2}{4\pi^2 c^2 \left(\frac{1}{\lambda_0+\delta\lambda_{\mathrm{sig}}} - \frac{1}{\lambda_0}\right)^2 + \left(\frac{\pi c}{\lambda_0 Q_{\mathrm{load}}^{\mathrm{sig}}}\right)^2} (1 - Tr_{\mathrm{min}}^{\mathrm{sig}}). \tag{4.13}$$

This equation is used later to compare the measured data with theory.

[*b] $\iint \tilde{I}(r,z) dS = 1$

## 4.2 Optical TO switch

Before performing optical Kerr switching, I perform optical switching experiment by using TO effect. As mentioned before, TO effect has much slower response time but can induce larger refractive index than Kerr effect.[102,35,39] As a result, observation of TO effect is easier than that of Kerr effect. In this section, I show the result of optical TO switching operation as a preparation for optical Kerr switching operation.

### 4.2.1 Experimental setup

In this subsection, the result of optical TO switching is shown. Figure 4.2 shows the experimental setup[*c]. Signal light is modulated by an electro-optical modulator (EOM) driven by a pulse pattern generator (PPG). Then the control light is amplified by an erbium-doped fiber amplifier (EDFA). Band pass filter (BPF) is inserted before it is mixed with signal light to eliminate amplified spontaneous emission (ASE) noise from EDFA. After two lights are outputted from DUT, it is split into two fibers via a fiber coupler. The one output of the coupler is connected to BPF to cut control light, and the light transmitted from BPF is detected by an optical sampling oscilloscope (OSO) and a power meter (PWM). The other light is detected by OSO without BPF. I use this signal to monitor the control output.

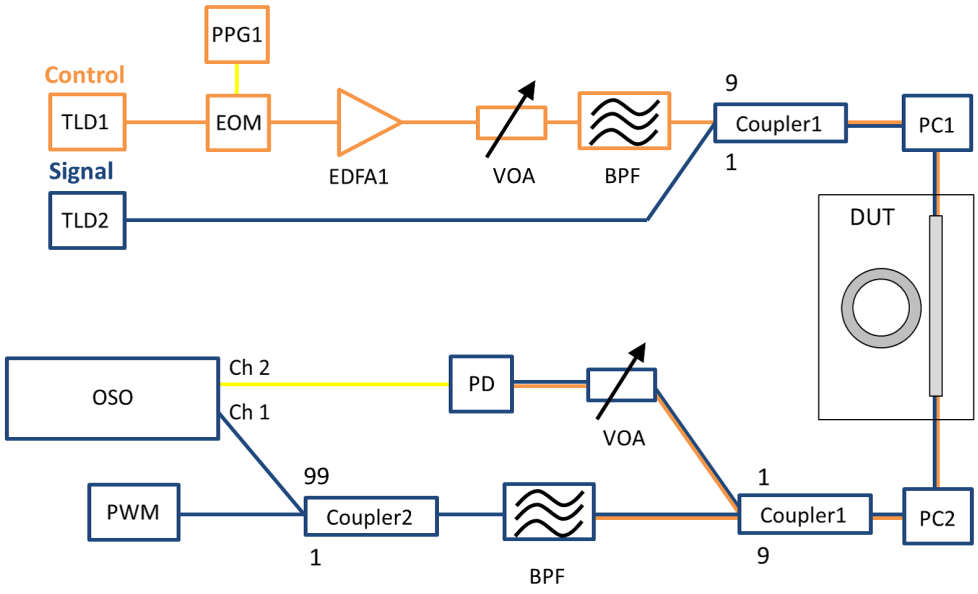


Fig. 4.2: Experimental setup for optical TO switch.

[*c]Model numbers of equipments and instruments used in the experiments are shown in A

### 4.2.2 Switching operation

The modes used for the experiment are shown in Fig. 4.3(a). The signal mode has wavelength of $\lambda_{\mathrm{sig}} = 1563.042$ nm and $Q$ of $Q_{\mathrm{sig}} = 9.6 \times 10^5$, and the control mode has wavelength of $\lambda_{\mathrm{cont}} = 1542.165$ nm and $Q$ of $Q_{\mathrm{cont}} = 8.5 \times 10^5$. Figure 4.3(b) shows observed TO switching operation. Signal output (the blue solid line) is successfully modulated by control signal (indicated by gray area) as can be seen in the figure. Therefore, we can conclude that we could achieve TO switch in silica toroid microcavity[*d]. The relaxation time $\tau_{\mathrm{relax}}$ is in the order of few hundreds of $\mu$s. It is longer than the optical TO switch based on silicon microring resonator.[17] This is because silicon has much higher thermal conductivity (1.422 W/(cm $\cdot$ K)[103]) than silica (1.36 W/(m $\cdot$ K)[104]) and silica toroid microcavity is thermally isolated by surrounding air. Longer thermal relaxation time is usually unwanted because it disturbs fast operation. However, longer relaxation diffusion time is preferred for optical Kerr switching because it makes discrimination between Kerr and TO effect easy due to large difference in response speeds of them as described later.

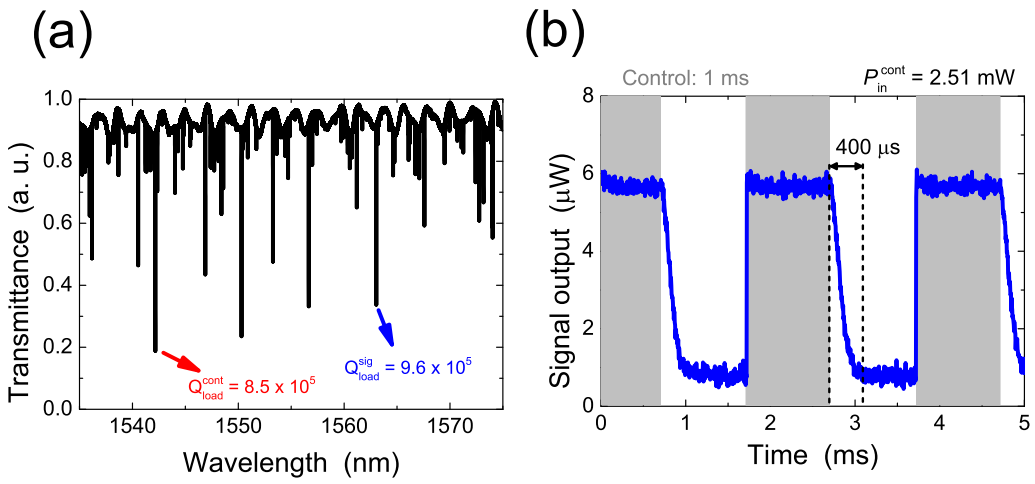


Fig. 4.3: (a) Modes used for the experiment. (b) TO switching operation. Blue solid line represent measured signal output power and gray area indicates that control light is inputted. The input control peak power $P_{\mathrm{in}}^{\mathrm{cont}}$ is 2.51 mW (rectangular shape).

Here, I evaluate input power dependency of TO switching. I observed TO switching operation for different input control powers as shown in Fig. 4.4(a). From the figure, I found that the switching contrast is higher as input control power $P_{\mathrm{in}}^{\mathrm{cont}}$ is larger. Figure 4.4(b) describes the relationship between the switching contrast and the input control power. Red dots represents experimental data. When $P_{\mathrm{in}}^{\mathrm{cont}}$ is lower than 1.6 mW[*e], switching contrast increases nearly in proportion to input control power. However when $P_{\mathrm{in}}^{\mathrm{cont}}$ is larger than 1.6 mW, switching contrast is saturated. This is because when

[*d] I confirmed that there was no leakage of control pulses from BPF. Thus the output shown in Fig. 4.3(b) is purely signal light

[*e] This power does not include taper facet loss.

resonant wavelength shift induced by control light is larger than linewidth of the control mode. As a result the coupling efficiency between control light and control mode is lower. As can be seen, $3-$dB switching is obtainable by input control power of $P_{\rm in}^{\rm control} = 1$ mW. For qualitatively analyzing results shown in Fig. 4.4(b), I draw the fitting curve shown as black solid line by using Eq. (4.7) and (4.13). It should be noted that most of constants in Eqs. (4.7) and (4.13) was determined by the experiment or taken from the literature. However, value of $Q_{\rm abs}$ and $C_{\rm heat}$ could not be experimentally obtained. $C_{\rm heat}$ is calculated by FEM using COMSOL multiphysics. Equation (4.6) indicates that the temperature change of the cavity $\Delta T$ is in proportion to the heat source $Qs_{\rm heat} = U_{\rm cavity}/\tau_{\rm abs}$ (i.e. absorbed light energy), thus $C_{\rm heat}$ was obtained by calculating the relation between $\Delta T$ and $Qs_{\rm heat}$. COMSOL multiphysics can model the heat diffusion by using FEM, thus I could calculate $C_{\rm heat}$. On the other hand, $Q_{\rm abs}$ is difficult to calculate. As mentioned in 1.2.4, the material absorption of silica is extremely small and it was reported as $Q_{\rm abs} = 2 \times 10^{11}$.[22] However, in practice, absorption of a silica-based microcavity is larger due to water layers and contaminants on its surface. Value of $Q_{\rm abs}$ of a silica-based microcavity reported in the previous papers are in the range from $10^{10}$ to $10^{7}$ due to uncertainty of thickness of surface absorber.[105,106,107] Therefore I drew several theoretical lines for different $Q_{\rm abs}$. As a result, I found that the use of $Q_{\rm abs} = 1.5 \times 10^{8}$ gave good agreement between the experimental and theoretical values as shown in Fig. 4.4(b). I would like to emphasize that $Q_{\rm abs}$ is the only fitting parameter I used. Hence, I confirmed that the switching operations shown in Figs. 4.3 and 4.4 are truly due to the TO effect (with negligible Kerr effect).

In this section, I confirmed that optical TO switching is obtained in a silica toroid microcavity. This is an important step for achieving optical Kerr switching.

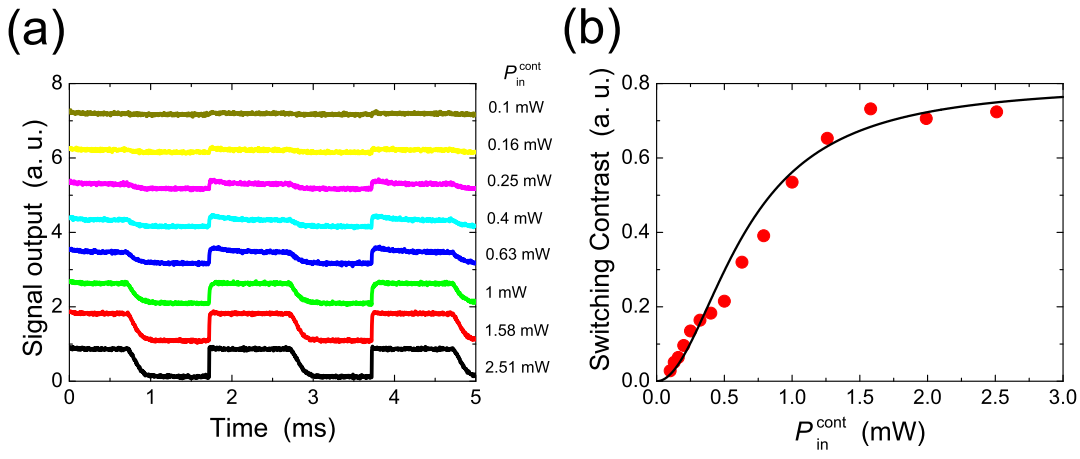


Fig. 4.4: (a) TO switching operation for different input pump power. (b) Resonant wavelength shift for different input pump power.

## 4.3 Optical Kerr switch

Here, I show results of optical Kerr switching experiments. First, experiments with one-wavelength scheme is described. These experiments were conducted to confirm the presence of Kerr effect without using complicated experimental setup. Second, results of two-wavelength experiments (Kerr switching experiments) are shown. Finally, I discuss and analyze the results.

### 4.3.1 Observation of Kerr effect

Purpose of this section is to experimentally confirm the presence of Kerr effect. For this, we developed an experimental setup as shown in Fig. 4.5(a). In Fig. 4.5(a), two EDFAs are placed after EOM. Maximum output power of EDFA2 in Fig. 4.5(a) is 30 dBm which is sufficiently high to induce Kerr effect in the microcavity. However, there is an interlock safety in EDFA2 that automatically turns the excitation laser diode off when average input power is smaller than 3 mW. The average light power passed through EOM is greatly attenuated due to the modulation and the insertion loss of EO modulator. Thus, I pre-amplify control light by using EDFA1 before inputting it into EDFA2 as shown in Fig. 4.5(a). In addition, variable optical attenuator (VOA) attenuates the output light before the detection to avoid the damage of OSO and PWM.

The principle of one-wavelength experiment is shown in Fig. 4.5(b). When input wavelength is carefully tuned to the resonant wavelength of the microcavity and set input power sufficiently low enough to avoid Kerr effect, transmitted signal power gradually drops as shown in the blue solid line in the right figure of 4.5(b). This is due to the interference between the transmitted light in the taper fiber and the light outputted from the microcavity. However, if input power exceeds the threshold power, Kerr effect appears and resonant wavelength is shifted. This wavelength shift is in proportion to the light energy stored in the microcavity, thus the output power is recovered in the middle of dropping (the red solid line in the right of Fig. 4.5(b)). As a result, output power does not drop to low. Observation of this recovery allows us to conclude that Kerr effect is present.

I used the microcavity which has a major radius of 35 $\mu$m and a minor radius of 2.3 $\mu$m. And $Q_{\mathrm{load}}$ is $3.5 \times 10^6$ for the mode I used. I conducted same experiments for different input powers of 31 $\mu$W, 314 $\mu$W, 992 $\mu$W, 3.1 mW, 9.9 mW, 31.4 mW and 99.2 mW. I employed rectangular pump pulses which have a width of 32 ns and duty cycle of 50 %. When input power is enough high to induce Kerr effect, the output power will recover as shown in Fig. 4.5(b). The experimental results are shown in Fig. 4.6(a). When input power is lower than 1 mW, output powers clearly drop to zero due to the interference. This is because input power is too low to cause Kerr effect as mentioned above. On the other hand, when input power is 3.1 mW, output power slightly recovers. Finally, when input power is 99.2 mW, the output power close to the same level of input power. This recovery is much faster than the thermal response time of 400 $\mu$s shown in 4.2.2. Hence I conclude that these phenomena are due to Kerr effect. To verify this understanding, we conducted numerical calculation based on CMT.[35] Result on

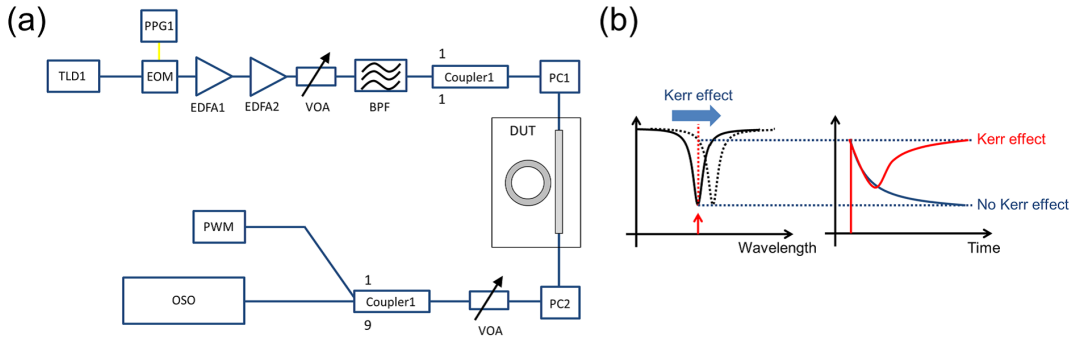


Fig. 4.5: (a) Block diagram of the experimental setup. (b) Schematic illustration of the operation principle.

numerical calculation is shown in Fig. 4.5(b)[*f]. Identical parameters as the experiment were used in the calculation and I found that the recovering behavior is well explained by the numerical calculations. Therefore, I conclude that there is Kerr effect in a silica toroid microcavity and it can be induced by inputting moderate input power of around 100 mW. This result is an important step towards to achieve optical Kerr switching operation.

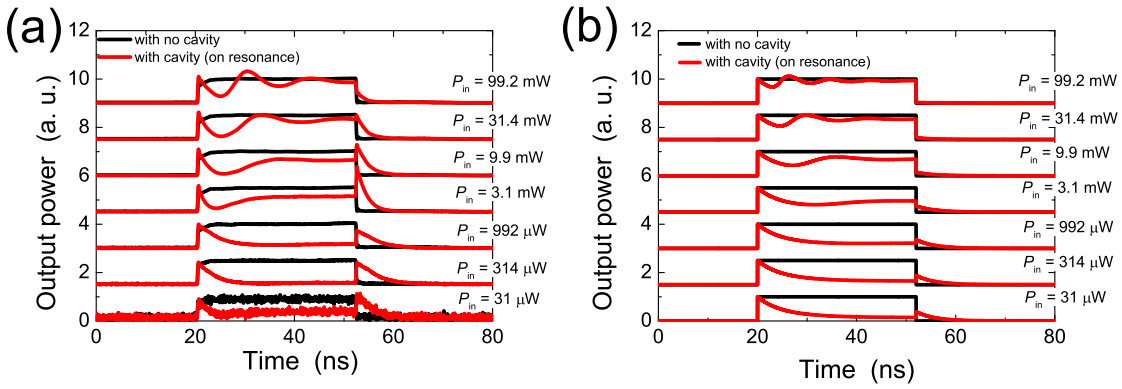


Fig. 4.6: (a) Experimental and (b) numerical results of probe-probe scheme. The red and black lines represent output powers with and without microcavity.

Close observation reveals that there are oscillations in the output in Fig. 4.6(a) and (b). I found that these oscillations were originating from the interference between the input mode and the cavity mode. A simple description on the origin of these oscillations is shown in Fig. 4.7(a). First, I assume that there is no coupling between the cavity and the taper fiber. I employed narrow linewidth laser ($< 500$ kHz corresponding 4 fm), which is

[*f]The calculation model is described in B in detail.

much smaller than cavity resonance (1 pm); thus it can be regarded as single wavelength. However, when the signal rising and falling, linewidth broadens due to the discontinuity of the signal. This is easily explained from the viewpoint of Fourier transformation. This is the origin of the oscillations shown in Fig. 4.6. Next, I assume that the taper fiber is coupled to microcavity and the input wavelength is detuned far from the cavity resonance. In this situation, most of the light does not couple to microcavity because input wavelength is detuned far from the resonance. However, when the input signal rising, the spectra is broadened due to the discontinuity of the signal. This allows small part of the light whose wavelength is equal to the cavity resonance to couple into the microcavity as shown in the lower of Fig. 4.7(b). After signal reaches to steady state, the spectrum recovers to single wavelength, and there are only two different light such as the input light and the light outputted from the cavity in a waveguide. As a result interference between these two lights creates the oscillation shown in Fig. 4.6.

To verify this prediction, I conducted similar experiments with different detunings of input wavelength. I employed rectangular pulses which have a duration of 32 ns, a duty cycle of 50 % and peak power of 134 $\mu$W, which is much smaller than Kerr threshold. I swept input wavelength from shorter to longer wavelength towards cavity resonance, and recorded output signal of each detuning values. The results are shown in Fig. 4.7(b). This figure clearly shows that there are oscillations when detuning is large. In addition, as can be seen in the graph, the oscillation frequency is higher as detuning is smaller. This is because the frequency is determined by the difference between input mode and cavity mode frequencies. Moreover, it is worth noting that the cause of oscillations in Fig. 4.6(a) is just the detuning between the input and cavity modes. In those cases, the detuning is originating from the resonant wavelength shift due to Kerr effect. However, it is not necessary to use nonlinear effect to create oscillations if there is the detuning. From these results, I found that such oscillations are originating from interference between input and cavity modes.

### 4.3.2 Switching operation

In the previous subsection, I showed that Kerr effect was present in the silica toroid microcavity at a moderate input power. In this section, I demonstrate results of optical switch using Kerr effect.

#### Experimental setup

Figure 4.8 shows the experimental setup for demonstrating optical Kerr switch. I use is two-wavelength scheme as described in 4.1, thus it is necessary to use two lasers for generating control and signal lights. There are two differences between the setups for Kerr and TO switching experiments such as (1) additional EDFA (EDFA2) which is inserted for generating high pump pulses and (2) alternative PPG (PPG2) which can generate high speed modulation signal ($>$ 3 ns) for generating short control pulses. To obtain large wavelength shift based on Kerr effect, it is necessary to efficiently couple the control light into the resonance. Thus we simultaneously monitored control and signal output by employing two channels of OSO to verify whether control pulse is efficiently

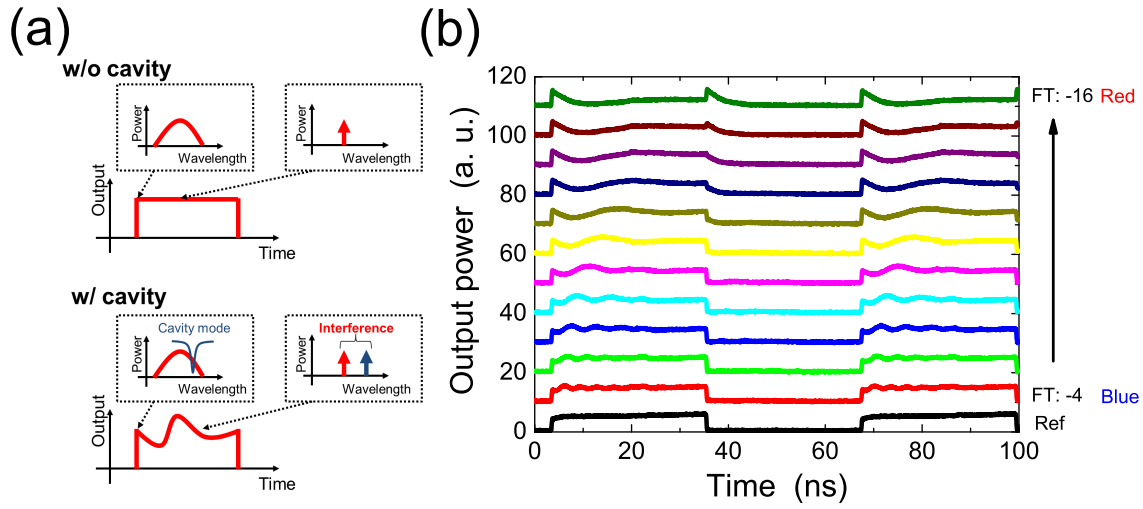


Fig. 4.7: (a) Description of the cause of the oscillations. (b) Output probe signal for different detuning value. Different lines represent output power for different detunings. "FT" indicate "fine tuning", which corresponds to the frequency (smaller FT value corresponds to longer wavelength). Black line is the output power when there is no cavity.

coupled or not. When control light is coupled well, I ought to observe the control output whose waveform is similar to Fig. 3.9(b). Moreover, if Kerr effect is induced by pump pulse, the control waveform like Fig. 4.6(a) must be observed.

I observed an oscillatory behavior when the control pulse with high peak power is inputted. The origin of the oscillation is due to the coupling between the optical and the mechanical modes in the microcavity, which are now intensively studied as "optomechanics.[62]" T. Carmon *et al.*[108] reported that the threshold of optomechanically motion was lower than that of nonlinear optical processes, such as Raman, parametric oscillation and erbium lasing. It interfere the observation of Kerr nonlinearity; this makes observation of Kerr switching operation difficult. To suppress the optomechanical motion, I employed a silica toroid microcavity with short beam length $L_{\mathrm{beam}}$. As a result, I was able to eliminate the oscillation such phenomenon even when a control pulse with high peak power was inputted.

### Switching operation with low-duty-cycle control pulses

As I described, silica has an extremely small absorption coefficient.[22] However, I found that resonant wavelength was drifted toward longer wavelength as input wavelength was approaching to resonant wavelength during the experiments in 4.3.1. Such "thermal drift" makes the experiment complicated, thus it is better to suppress the generation of heat. For this, I first employed control pulse trains which have low-duty-cycle in order to have small average power. This will result in suppression of thermal drift of resonant wavelength. Therefore, in this section, the result of experiments with low-duty-cycle

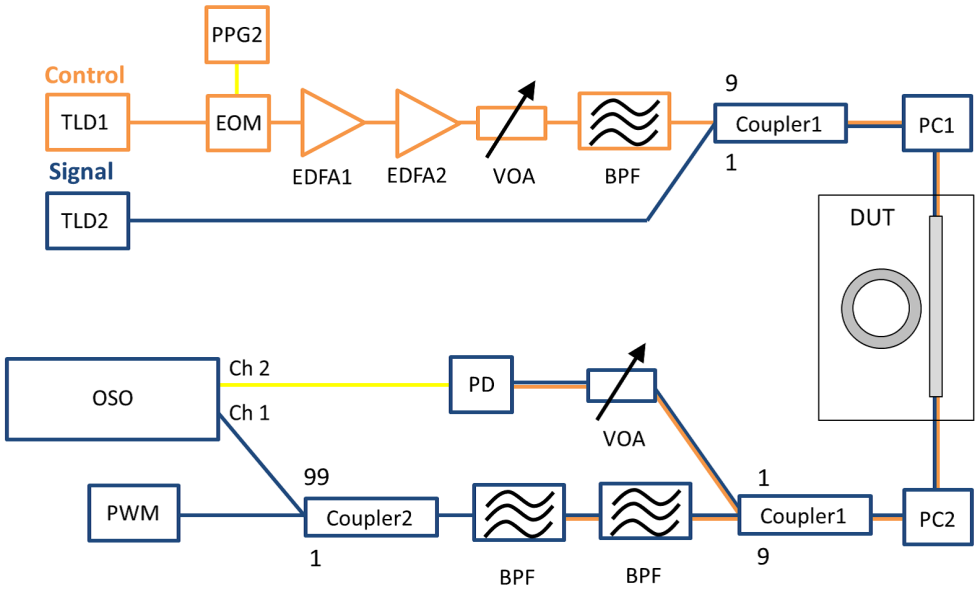


Fig. 4.8: Experimental setup for optical Kerr switching experiment.

pulses is described.

Figure 4.9(a) shows switched signal output for different input control powers when $Q_{\mathrm{load}}^{\mathrm{control}}$ of $3.3\times10^6$ and a probe mode with $Q_{\mathrm{load}}^{\mathrm{signal}}$ of $9\times10^6$ were employed. Each control pulses have a fixed duration of 32 ns and a cycle of 2048 ns. When control pulses are inputted (indicated by gray area), the signal output (blue solid lines) rises. In addition, probe output drops when control pulses are turned off. This behaviors of signal output are the clear evidence that probe signals are switched by control light. Therefore, I conclude that optical switching is achieved by using low-duty-cycle pulses. However, the remaining question here is whether these switching operations are really induced by purely Kerr effect or not. To answer this question, the magnified graph of the switched signal output for $P_{\mathrm{in}}^{\mathrm{pump}} = 13$ mW is shown in Fig. 4.9(b). In this graph, signal power drops within 20 ns after the control pulse is switched off. This fast switching is originating from Kerr effect. On the other hand, even when the control pulse is completely switched off, signal output does not return to initial value (in this case 0.2). This is because large TO effect occurs together with Kerr effect. TO effect has slow relaxation of $> \mu$s and its effect stays fro a long time even after control pulse was switched off. So for obtaining optical switching operation purely by Kerr effect, TO effect must be suppressed..

### Switching operation with high-duty-cycle control pulses

I decided to use high-duty-cycle pump pulses to suppress influence of TO effect. By using such pulses, I expects that thermal saturation is caused, and then influence from TO effect is suppressed. The basic idea of this strategy is explained in Fig. 4.10. When

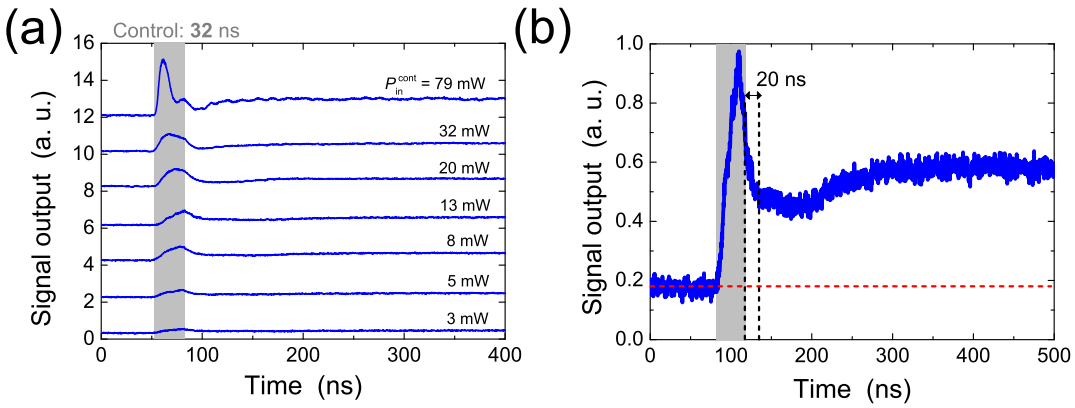


Fig. 4.9: (a) Switched signal output for different input control power. Gray area means that control pulse is inputted. It should be noted that signal output is normalized by signal output power without cavity and each line is offseted by 2. (b) Magnified graph of the switched signal output for $P_{\mathrm{in}}^{\mathrm{control}} = 13$ mW.

control pulses with low-duty cycle are employed, there is sufficient time to relax TO effect as shown in Fig. 4.10(a). In this condition, wavelength shift is caused by both Kerr and TO effect. On the other hand, when pulse train have high-duty-cycle, microcavity is thermally saturated and there is no time for heat to relax. With this condition, only Kerr effect will respond to fast pulses Kerr switching will be achieved by employing based on thermal saturation. Eventually, it is expected that Kerr effect can be discriminated from TO effect by using high-duty-cycle pulses[*g].

Figure 4.11(a) shows results on switching operation with high-duty-cycle control pulses. I inputted control pulses with a duration of 64 ns and a duty cycle of 50 %. A cavity with $Q_{\mathrm{load}}^{\mathrm{cont}} = 5.1 \times 10^6$ and $Q_{\mathrm{load}}^{\mathrm{sig}} = 3.3 \times 10^6$ were employed. As shown in Fig. 4.11(a), signal output is switched off when control pulse is inputted. In addition, switching time is a few-tens of ns, which is much shorter than the TO switching time of 400 $\mu$s shown in 4.2.2. Signal output returns to the initial value when control light is switched off. This is an indirect evidence proving that switching was based on Kerr effect[*h].

### 4.3.3 Discussions

#### Discrimination of Kerr and TO effects

Here, I discuss the result of optical Kerr switching. First, I investigate whether or not the optical switch is based purely on Kerr effect in detail. As some references pointed out,[74,18] response times of Kerr and TO effect are greatly different. When the modulation frequency of control light is much higher than the thermal response frequency, the Kerr

[*g] As mentioned in 4.3.2, high-duty-cycle pulses inevitably induce thermally drift. Although it makes experiments complicated, it is possible to conduct experiments in the presence of thermal drift.

[*h] Detailed confirmation of Kerr switching will be given in later.

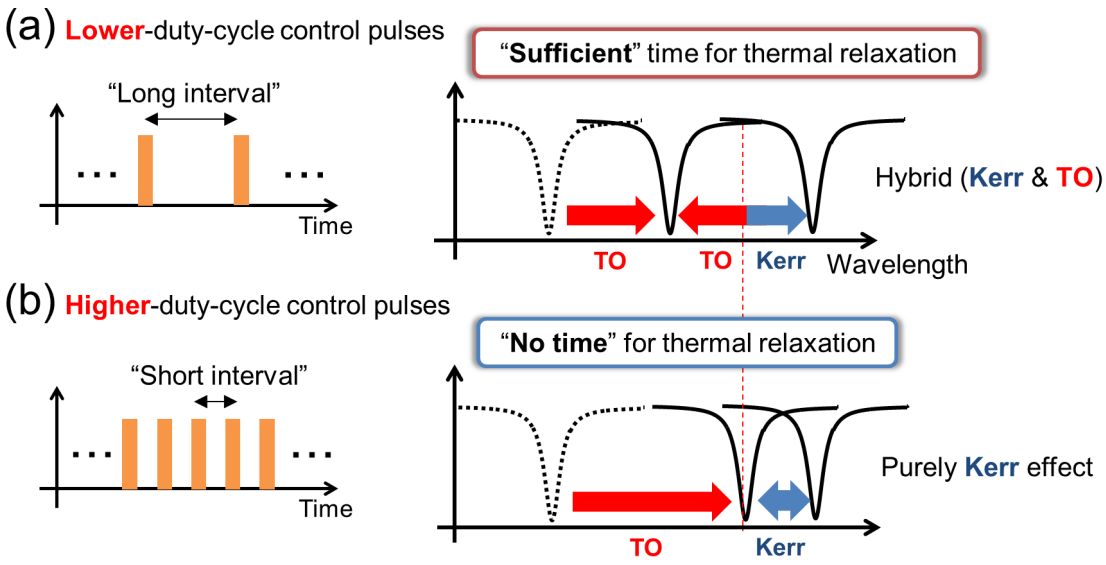


Fig. 4.10: Explanation of use of thermal saturation. Case for (a) low-duty-cycle pulses and (b) high-duty-cycle pulses.

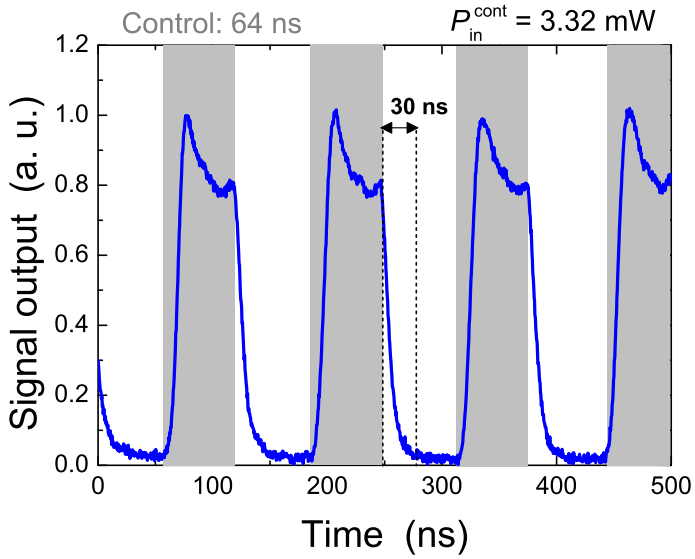


Fig. 4.11: Signal output switched by high-duty-cycle control pulses.

effect dominates the TO effect because TO effect cannot respond to the modulation frequency of the control light. On the other hand when the modulation frequency of the control pulse is close to the frequency that the thermal effect can respond, TO effect becomes apparent. With this condition, there are two switching slope which are caused by Kerr and TO effects at output. So, I employed some control pulses which have different modulation frequency to discriminate Kerr and TO effects. When there is only one switching slope, I am able to qualitatively confirm that the switching is based on the Kerr effect. Moreover, to evaluate influence of the TO effect accurately, I considered two cases: Signal wavelength (1) is set on-resonance and (2) is detuned from a resonance. The value of $\mathrm{d}Tr/\mathrm{d}\lambda$ is significantly different depending on the detuning between the input wavelength and the cavity resonance (see Fig. 3.2(a)). When I set detuning $\delta\lambda = 0$, small wavelength shift does not reflect on the change of transmittance due to small value of $\mathrm{d}Tr/\mathrm{d}\lambda$. Thus there is a risk that such small wavelength shift is not possible to observe in this condition. To avoid to miss the small wavelength shift, I collected data considering two cases described above.

Figure 4.12(a)-(d) show signal outputs for different control modulation frequency. In Fig. 4.12(a) and (b), there are only fast switching slopes and response is flat independently to the detuning. Hence, Kerr effect is dominant in these regimes. On the other hand, in Fig. 4.12(c) there are two switching slopes in the case of on-resonance. The faster one and slower one are originating from Kerr and TO effects, respectively. This indicates that switchings in Fig. 4.12(c) are based on hybrid effect; Thus pure Kerr switching cannot be achieved. Finally, Fig. 4.12(d) shows only slow switching slope. At this condition, switching is dominated by TO effect. Therefore from Fig. 4.12(a)-(d), I found that I extract Kerr effect by using control pulses which have high modulation frequency. In addition, these results show that there is no TO effect when control pulse cycle $T_{\mathrm{cycle}}$ is smaller than 256 ns. Considering this fact, I conclude that switching operations shown in Fig. 4.11 are based on Kerr effect because $T_{\mathrm{cycle}}$ is 128 ns, which is much smaller than 256 ns.

Next, I quantitatively discuss that the switching operation shown in Fig. 4.11 is based on Kerr effect. For this, I performed several optical switch experiments and obtained the switching contrast by using different control input power. And then, I compared them with the theory described in 4.1.2. The results are shown in Fig. 4.13(a). The red dots in the figure represent the data obtained by the experiments. As can be seen in Fig. 4.13(a), switching contrast increases when input control power is increased. To compare the experimental data with the theory, I draw theoretical curves as shown in Fig. 4.13(a) by using Eqs. (4.10) and (4.13). As described in Eq. (4.10), the induced resonant wavelength shift depends on the distribution of the excited WGM (i.e. $\tilde{I}(r, z)$), but it was difficult to experimentally determine the mode that was was excited. Thus, I assumed three WGMs ( $(q, l, m) = (0, 0, 205)$, $(0, 1, 205)$ and $(1, 0, 205)$) and compared them with the experimental data. It should be noted that $\tilde{I}(r, z)$ was calculated by the FEM solver (COMSOL multiphysics).[109] Black solid, dashed and dotted curves in the figure assume WGMs with $(q, l, m) = (0, 0, 205)$, $(0, 1, 205)$ and $(1, 0, 205)$, respectively. $m = 205$ corresponds to $\lambda_{\mathrm{sig}} \approx 1559$ nm. Figure 4.13(b) shows a curve with $(0, 1, 205)$ that has good agreement with the experimental data. In addition, when we assume that both Kerr and TO effects (blue solid line in Fig. 4.13(b)), the theoretical curve is

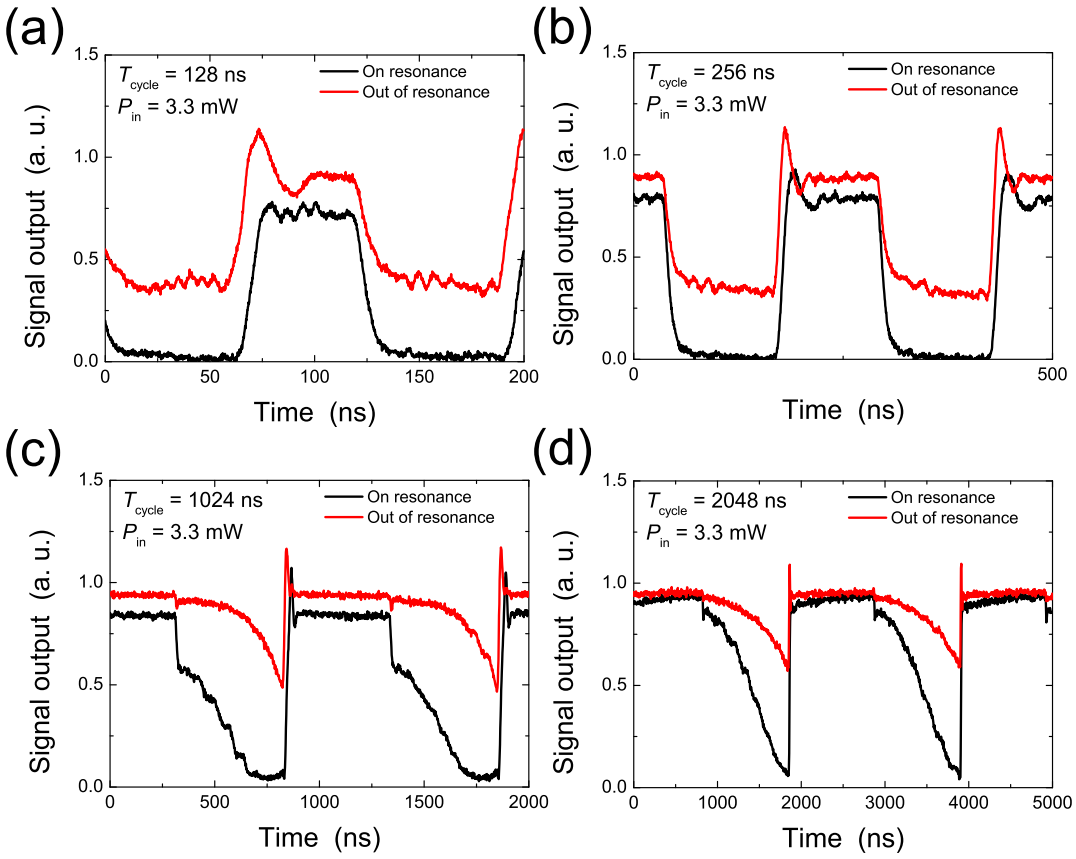


Fig. 4.12: Signal output for different modulation control frequency. Black and red solid lines represent signal output when control wavelength is on-resonance and is detuned from the resonance. Control power of 3.3 mW was inputted. (a) $T_{\text{cycle}} = 128$ ns (b) $T_{\text{cycle}} = 256$ ns (c) $T_{\text{cycle}} = 1024$ ns (d) $T_{\text{cycle}} = 2056$ ns

much larger than the experimental data. Thus there is no TO effect in this situation. In summary, I qualitatively confirmed that optical switching operation described in this section were based solely on Kerr effect.

### Discussions on required power

Finally, I discuss the control power of experimental data shown in Fig. 4.13(a). When I input control power of 5.26 mW, large switching contrast of 84 % was achieved. When I reduce control peak power was reduced to 834 $\mu$W, switching operation is still observed. In the previous studies, GaInP photonic crystal Fabry-Perot resonator,[21] nonlinear Mach Zehnder switch[15] and hydrogenated amorphous silicon microring resonator[67] required input control power of 200 mW, 63 mW and 1.1 W for switching, respectively. But there is no on-chip Kerr switch that can be driven by the input pump power of less than 1 mW to the best of my knowledge. Therefore, the required input control power of 834 $\mu$W is the smallest value among the previous on-chip optical Kerr switches. Furthermore, obviously this switch has low insertion loss because there is only tapering loss of 5 % as shown in Fig. 3.6[*i]

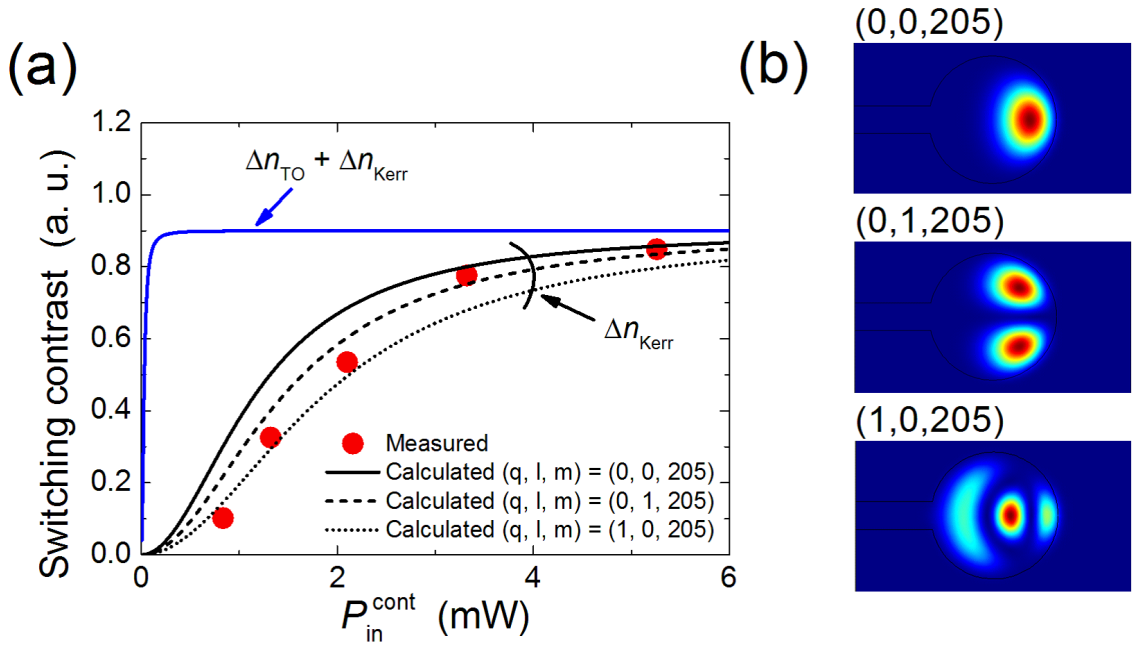


Fig. 4.13: (a) The relationship between the switching contrast $\eta$ and the input pump peak power $P_{\rm in}^{\rm pump}$. Black solid, dashed and dotted curves in the figure are for WGMs with $(q, l, m) = (0, 0, 205)$, $(0, 1, 205)$ and $(1, 0, 205)$, respectively. Blue solid line considers Kerr and TO effects.(b) Distributions of WGMs calculated by COMSOL multiphysics.

[*i]It should be noted that this value does not include fiber splice loss and loss due to BPFs. The former is typically 1 $\sim$ 2 dB, but can be eliminating by using fusion splicing in practice. In addition, the latter is common for optical switches which are based on "two-wavelength" scheme, thus it should not be considered.

## 4.4 Summary

In this chapter, I showed the results on optical switch experiments in a side-coupled system. First, I showed the result of TO switching, and experimentally confirmed basic principle of microcavity-based switch. After that the result of optical Kerr switching was shown. Through several experiments, I concluded that optical Kerr switch is achieved in a side-coupled silica toroid microcavity system. Required input control power of 834 $\mu$W was the smallest among previously demonstrated on-chip optical Kerr switches.

By using silica toroid microcavity, I demonstrated microcavity-based switch with low-insertion loss on a chip. Some previous studies demonstrated low-insertion loss optical switch as introduced in 1.4.1, but no studies demonstrated optical switch on a chip. In addition, I showed that a much faster speed of 30 ns is possible with Kerr effect in contrast to 400 $\mu$s with TO effect. Low insertion loss, fast switching and capability of on-chip fabrication is essential for practical optical switch. In particular, low insertion loss is important to switch few-photon level optical signal, that is the building block of few-photon level optical telecommunication. Thus I believe this study paves the way to develop future few-photon optical telecommunication.

# Chapter 5

# Optical Kerr switch in an add-drop system

In the previous chapter, I showed switching experiment in a side-coupled system. Although I was able to show ON/OFF modulation of the signal light, often routing of the light is required for optical switches in an actual optical communication system. For this, in this chapter, switching experiment in an add-drop system is demonstrated. First, I overview design and strategy to achieve an add-drop system. Next, I characterize transmittance of an add-drop system. Finally, I show the results of switching operation using an add-drop system.

## 5.1 Development of an add-drop system

In this section, I show the setup of an add-drop system built for switching experiments. First, basic strategy for developing an add-drop system is described. Next, a bent taper fiber is explained, which is the key component for developing an add-drop system. Especially, I focus on the fabrication of a bent taper fiber and the bending loss. Finally, I describe the stage system holding a bent taper fiber.

### 5.1.1 Design and strategy

In this subsection, I introduce the design and strategy to demonstrate an optical Kerr switching in an add-drop system. To the present add-drop systems were developed in a silica bottle microcavity,[18] a microsphere[76] and a silica toroid microcavity.[28,77] It is easy to achieve an add-drop system for a bottle microcavity, because bus and drop fibers is vertically separated (see Fig. 3.4 in the reference[38]). On the other hand, it is necessary to place bus and drop fibers in parallel with separation of a diameter of a cavity ($< 100$ $\mu$m) for a microsphere and a silica toroid microcavity. There are two previous studies reporting on the development of an add-drop system. However, in H. Rokhsari and K. Vahala,[28] the bus fiber touches with a microcavity probably due to tight spatial constraint; this inevitably results in large reduction of $Q_{\mathrm{load}}$. High-$Q$ is preferred for achieving Kerr switching, thus the contact should be avoided. On the the hand, in

F. Monifi *et al.*,[77] robust coupling was achieved by placing bus and drop fiber on a silica sidewall. However, they controlled the position of taper fibers by using an additional fiber tip. Thus it seems to be difficult to precisely control the positions of bus and drop fibers independently. As described in 3.1.2, the coupling condition of bus and drop fibers is critical to optimize the transmittance and $Q_{\mathrm{load}}$ in an add-drop system, hence the controllability of two fibers are desired. Therefore, the development of an add-drop measurement system of a silica toroid microcavity that has the controllability and allows the bus fiber approach the cavity without contacting with it seems to be a difficult but necessary challenge.

Figure 5.1(a) shows schematic illustration of an add-drop system consists of two straight taper fibers. In general, a single mode fiber has a diameter of 125 $\mu$m and our microcavity has a diameter of smaller than 100 $\mu$m. When we place two fibers on both sides of a cavity, they will interference each other at their non-tapered regions. As a result, an add-drop system based on "two straight taper fiber scheme" is difficult in a silica toroid microcavity.

To avoid the interference of bus and drop fibers, I use "bent taper fiber" as a drop fiber, which was originally used by Painter's group to couple light into PhC.[110] As shown in Fig. 5.1(b), by bending a drop fiber, I expect that I can avoid interference between bus and drop fibers. Therefore, I design an add-drop system employing a bend taper fiber.

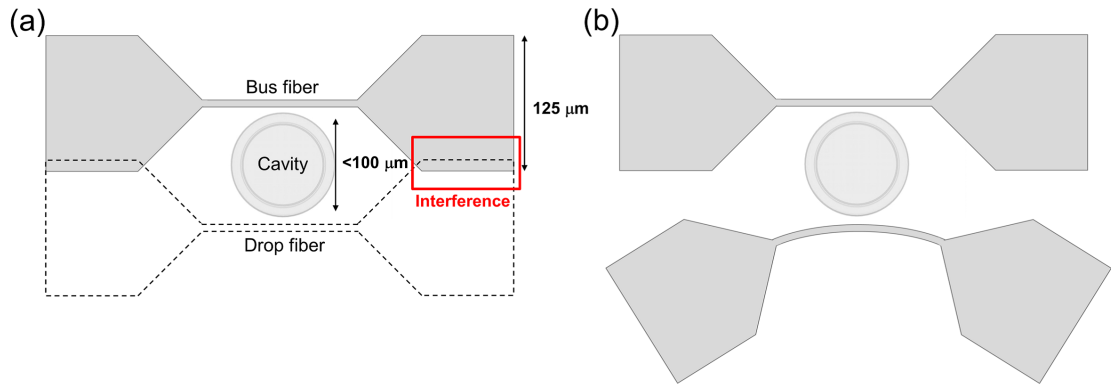


Fig. 5.1: (a) Add-drop system based on "two straight taper fiber" scheme. (b) Add-drop system with a bend drop fiber.

Here I discuss the expected transmittance of my add-drop system. Previous studies reported transmittance of 93 % in a silica toroid microcavity[28] and 90 % in a silica bottle microcavity.[18] According to these studies, it appears that I do not have to consider loss of an add-drop system. However, as described before, an add-drop setup in this study is significantly different from the previous studies. First, I use a bent taper fiber instead of a straight fiber. It is well-known that bending an optical fiber will increase bending loss, thus there is possibility that additional loss due to bending will be caused in a bent drop fiber. Second, in the former study for a silica toroid microcavity, a bus fiber is

contacted to a cavity. In general the contact significantly reduce $Q_{\mathrm{load}}$ of microcavity. In fact, $Q_{\mathrm{load}}$ got 30 times smaller than $Q_{\mathrm{int}}$ due to the contact in the previous study.[28] Thus the contact between a drop fiber and a cavity is not preferred because switching contrast induced by Kerr effect scales with $Q_{\mathrm{load}}^2$. Considering this fact, I decided to place the drop fiber without contacting with the cavity. However, contact-less condition may result in low transmittance from bus fiber to drop fiber due to insufficient coupling strength. Therefore, it is necessary for me to carefully evaluate the transmittance of my add-drop system for achieving optical switch using an add-drop system.

### 5.1.2 Fabrication of a bent taper fiber

As mentioned above, I decided to employ a bent taper fiber as a drop fiber. Therefore, in this subsection, I explain how I fabricate a bent taper fiber and the characterized bending loss.

The fabrication process of a bent fiber is the almost same as that of a straight taper fiber as shown in Fig. 3.3. The difference between them is just the post-fabrication process. In the case of a straight taper fiber, I move it directly to the measurement system without detaching it from a fiber holder after tapering. On the other hand, in a case of a bent taper fiber, I have to detach it and bend it by hand. Taper fiber is strong enough to endure a manual bending procedure. Then bent taper fiber is attached on two slide glasses with UV curable epoxy (ThorLabs/NOA81), which indurate by few-minutes UV irradiation. The reason why a bent taper fiber is attached to "two" slide glass is that a bent taper fiber has to be stretched. Figure 5.2(a) and (b) shows a schematic illustration and a picture of a bent fiber. Bent taper fiber is slackened after the attachment to two slide glasses, and this may cause vibration during optical measurement. Therefore, it is necessary to remove such slackening. For this, we increase the distance between two slide glass $d$ as shown in the lower of Fig. 5.2(a). After this process, slackening is removed, and then, positions of two slide glass is fixed by UV curable epoxy. Figure 5.2(b) is a picture of bent taper fiber I attached on two slide glasses.

Next, bending loss of a bent taper fiber is measured. Figure 5.3 shows typical bending loss of bent taper fiber. We measure the loss caused by bending for different $d$ values. For $d = 10$ mm, which is the initial value, there is no additional loss in comparison with loss of a taper fiber before bending. As long as $d$ is smaller than 20 mm, no bending loss is generated as shown in the graph. However, when $d$ exceeds 20 mm, bending loss suddenly increases. This is because curvature at transition of vertical and horizontal parts become too steep due to strong tension. Actually, in the lower right picture (bent fiber for $d = 40$ mm) in Fig. 5.3, vertical parts of taper fiber are drawn to the inner. This is an evidence that there is strong tension in bent taper fiber with large $d$.

Considering suppression of vibration due to slackening and bending loss, I used a bent taper with $d$ of around 20 mm.

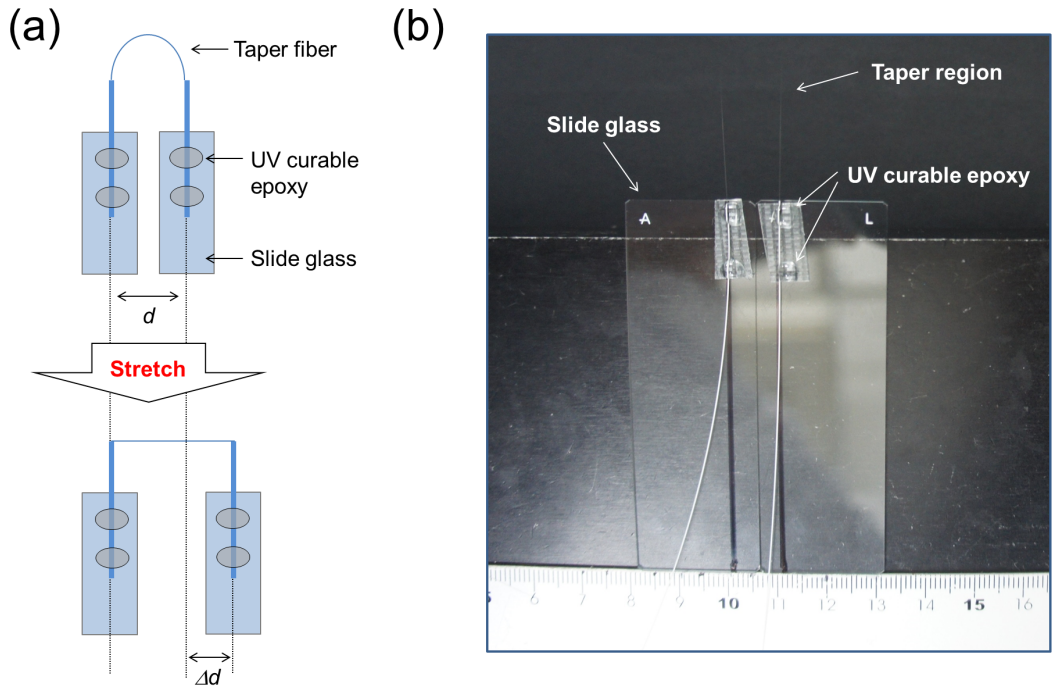


Fig. 5.2: (a) Schematic and (b) picture of bent taper fiber.

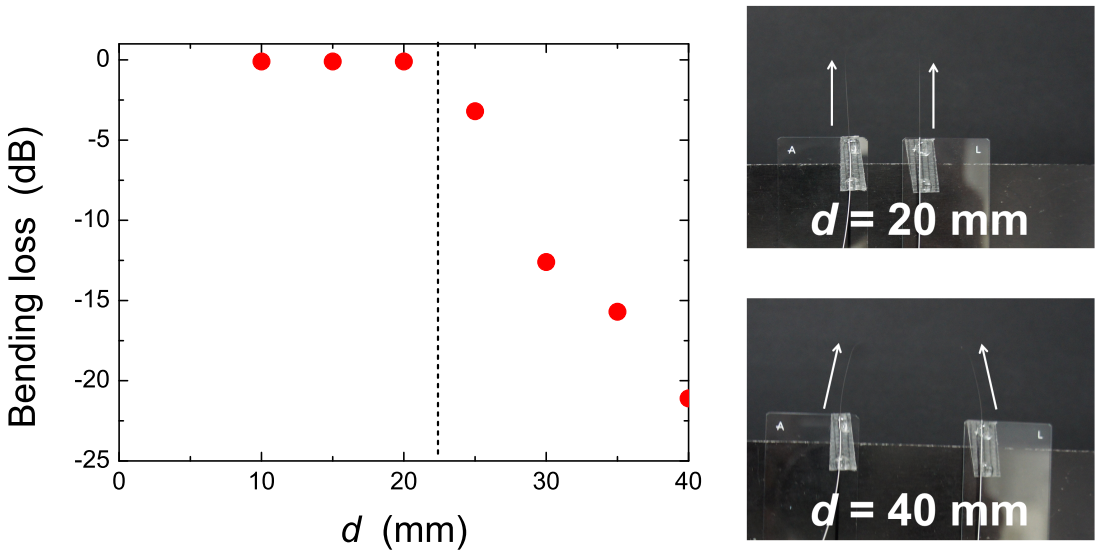


Fig. 5.3: Bending loss of fabricated bent taper fiber as a function of $d$.

### 5.1.3 Development of stage system for a drop fiber

Next, I built a stage system for a drop fiber[*a]. The picture of the stage system for a drop fiber is shown in Fig. 5.4. In the measurement system for a side-coupled configuration, the position of the taper fiber is fixed and the position of chip is controlled by automatic $xyz$ stage. For putting bus and drop fibers close to the cavity simultaneously, the position of a drop fiber has to be carefully adjusted. Therefore, this system requires $xyz$ automatic stage. In addition, for carefully controlling the inclination of a drop fiber, manual gonio stage is used. Moreover, to make a drop fiber accurately parallel to a bus fiber, a manual rotation stage is also used.

It should be noted that the slide glasses which hold a bent (drop) taper fiber is attached to the stage system by the clamp. I placed the stage system close to the chip holder and tried to make the aluminum pole as short as possible to suppress the vibration.

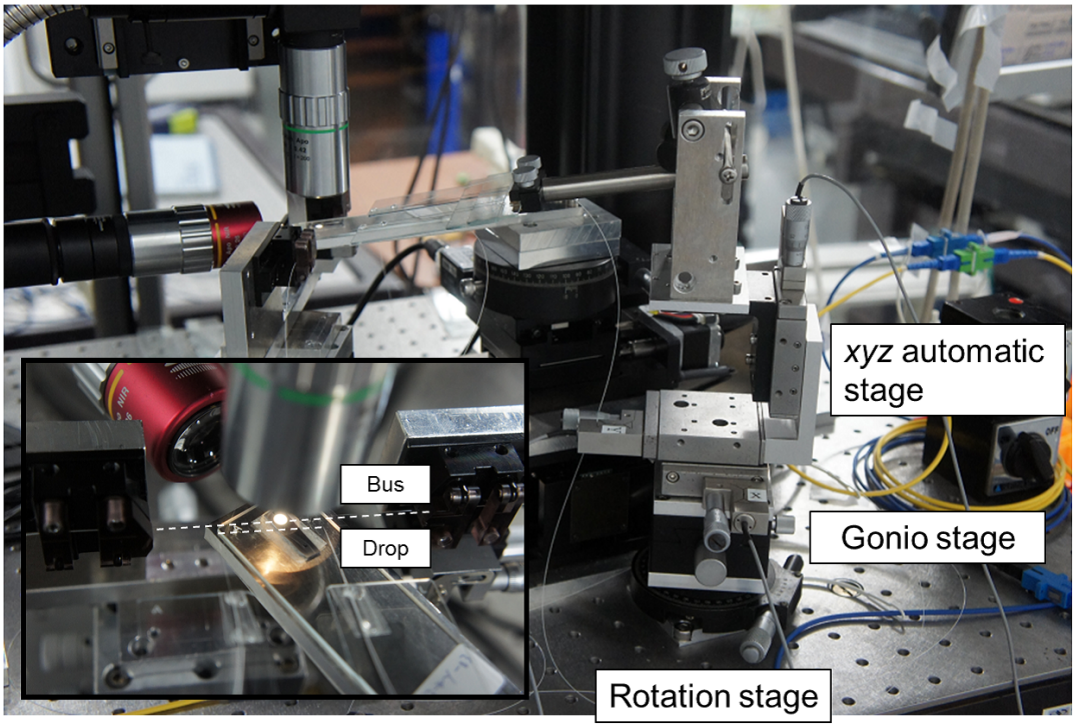


Fig. 5.4: The picture of the stage system for a drop fiber. The inset shows bus and drop fibers.

[*a]This was designed by the author and his colleague Y. Yakushiji

## 5.2 Switching operation in an add-drop system

Here, I describe the experimental results conducted with an add-drop system is described. First, I measured the signal transmission to a drop fiber from a bus fiber without inputting control signal. By carefully adjusting the coupling to bus and drop fibers, high transmittance is expected to be obtained. After that, the results on optical switch in an add-drop system is shown.

### 5.2.1 Signal transmission of an add-drop system

Before starting optical switch experiments, I confirmed the signal transmission from a bus fiber to a drop fiber. For obtaining high transmittance from a bus (straight) fiber to a drop (bent) fiber, they are placed in over-coupled regime as shown in Fig. 3.4(a) and (b). As mentioned in 3.4.3, the phase-matching condition need to be satisfied to achieve the over-coupled condition. Thus, I first confirm that modes in bus and drop fibers are phase-matched to the cavity mode individually.

For this, I conducted a similar experiment described in 3.11 for different taper-fiber diameters. If a WGM of interest is sufficiently phase-matched to a mode in a taper-fiber, minimum transmittance $Tr$ (i.e. transmittance on resonance) recovers to the reference level when a taper-fiber is closely placed with a cavity. However, here I focus on a particular mode that will be used in the switching experiment. Figure 5.5(a) shows the minimum transmittance in function on the cavity-fiber distance $d$ for a bus fiber. Note that $x$ indicates the position of taper fiber which is coupled to a microcavity as shown Fig. 3.10(a). When $x \leq 0.5$ mm, the fiber reaches to the contact point with the cavity before $Tr_{\mathrm{min}}$ increases. On the other hand, when $x \geq 1$ mm, $Tr_{\mathrm{min}}$ begins to recover, and then $Tr_{\mathrm{min}}$ at the contact point is maximum when $x$ is 2 mm. Thus phase-matching condition is satisfied when $x = 2$ mm. In addition, the critical-coupling was observed around $d = 900$ nm. Note that the non-zero transmittance around critical coupling was due to the input polarization, which is not optimized. Moreover, it is intuitive that $Tr_{\mathrm{min}}$ at the contact point dropped again when $x \geq 2$ mm because phase-matching condition was failed to satisfied as same as the case of $x < 2$ mm. I conducted same experiments for a drop fiber and almost identical result was obtained as shown in Fig. 5.5(b).

Next, transmittance of an add-drop system is measured. The experimental setup is shown in Fig. 5.6. I inputted into "port 1," and then the light transmitted to "port 2" and "port 3" were detected. The light signal inputted from port 1 propagates in clockwise (CW) direction in the microcavity, thus it outputs to port 3[*b]. Transmittance from port 1 to port 2 is defined as $Tr^{\mathrm{bus}}$ and that from port 1 and port 3 is defined as $Tr^{\mathrm{drop}}$. By using OSO and PWM, the transmission spectrum and transmitted signal are simultaneously measured.

Here I show the typical results of transmission spectrum of an add-drop system. I set the cavity-bus-fiber distance $d_{\mathrm{bus}}$ and the cavity-drop-fiber distance $d_{\mathrm{drop}}$ at 800 nm and 1.68 $\mu$m. It is shown in Fig. 5.7. As predicted in Fig. 3.3(b), transmission spectra of bus

[*b]There is light propagating in counter-clockwise (CCW) direction in a real microcavity. Such light is induced due to the Rayleigh scattering which is originating from the surface roughness[91] and could be measured at port 4.

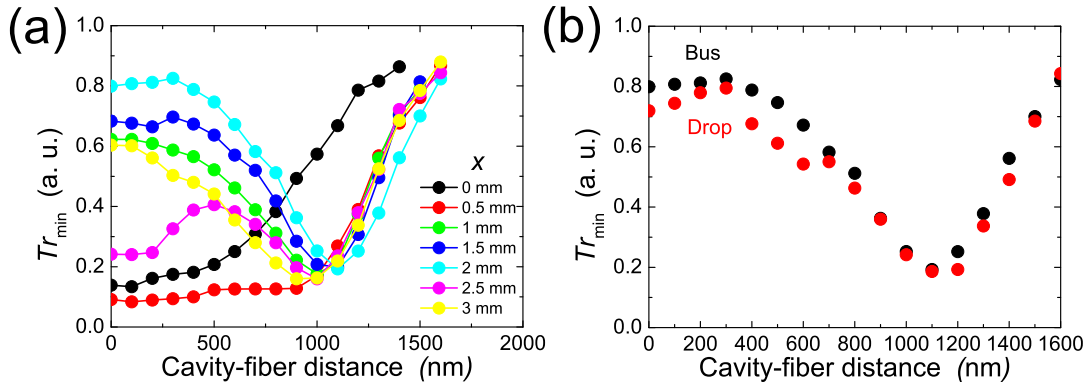


Fig. 5.5: (a) Minimum transmittance $Tr_{\min}$ for different cavity-fiber distance $d$. The different colors indicate different position $x$ of the taper fiber which we used to couple to a microcavity as shown Fig. 3.10(a). (b) Comparison of minimum transmittance between for a bus and a drop fibers. Black and red dots are for bus and drop fibers.

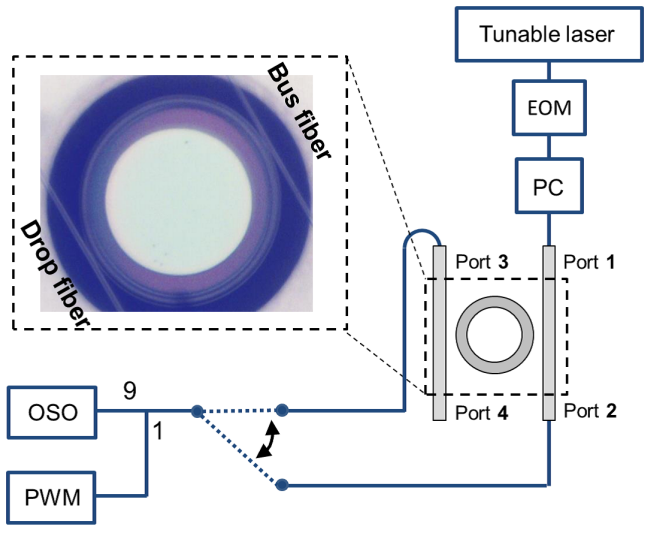


Fig. 5.6: Experimental setup to measure signal transmission of an add-drop system.

and drop fiber have inverse shapes. This behavior is explained as follows: When the input light resonates with the cavity, the light energy will be stored in the microcavity; Thus the power outputted to the drop fiber is increased. As for a bus fiber the output power from the cavity also increases, and then the light from cavity and the light transmitted from port 1 destructively interfere. As a result $Tr^{\mathrm{bus}}$ drops.

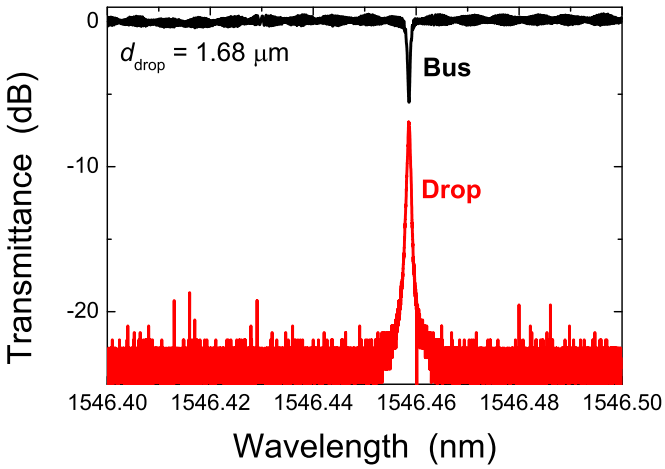


Fig. 5.7: Transmission spectrum from bus (black solid line) and drop (red solid line) fibers when $d_{\mathrm{bus}} = 800$ nm and $d_{\mathrm{drop}} = 1.68$ $\mu$m.

According to Eq. (3.8) and (3.9), the transmittance from bus and drop fiber on resonance ($Tr^{\mathrm{bus}}_{\mathrm{min}}$ and $Tr^{\mathrm{drop}}_{\mathrm{max}}$) should be dependent on $\tau_{\mathrm{bus}}$ (i.e. $d_{\mathrm{bus}}$) and $\tau_{\mathrm{drop}}$ (i.e. $d_{\mathrm{drop}}$). So, I next examine the dependency of $Tr^{\mathrm{bus}}_{\mathrm{min}}$ and $Tr^{\mathrm{drop}}_{\mathrm{max}}$ on the cavity-fiber distance $d_{\mathrm{bus}}$ and $d_{\mathrm{drop}}$. Figures 5.8(a) and (b) show $Tr^{\mathrm{bus}}_{\mathrm{min}}$ and $Tr^{\mathrm{drop}}_{\mathrm{max}}$ for different $d_{\mathrm{drop}}$[*c]. $d_{\mathrm{bus}}$ is set at 800 nm and 600 nm in Fig. 5.8(a) and (b). Figure 5.5(b) show that $d_{\mathrm{bus}} = 800$ nm and $d_{\mathrm{bus}} = 600$ nm are weakly and strongly over-coupled conditions. Figure 5.8(a) shows that $Tr^{\mathrm{bus}}_{\mathrm{min}}$ dropped when $d_{\mathrm{drop}}$ was reduced. This is because the bus fiber was placed in over-coupling ($\tau_{\mathrm{bus}} < (\tau_{\mathrm{int}}^{-1} + \tau_{\mathrm{drop}}^{-1})^{-1}$) regime in the beginning, but it is closer at a critical-coupling ($\tau_{\mathrm{bus}} \approx (\tau_{\mathrm{int}}^{-1} + \tau_{\mathrm{drop}}^{-1})^{-1}$) regime when $d_{\mathrm{drop}}$ (i.e. $\tau_{\mathrm{drop}}$) is smaller. When we further decrease $d_{\mathrm{drop}}$, the coupling is in under-coupling regime ($\tau_{\mathrm{bus}} > (\tau_{\mathrm{int}}^{-1} + \tau_{\mathrm{drop}}^{-1})^{-1}$)) thus, $Tr^{\mathrm{bus}}_{\mathrm{min}}$ drops again. As for $Tr^{\mathrm{drop}}_{\mathrm{max}}$, it was increased when $d_{\mathrm{drop}}$ was decreased because the coupling between the cavity and the drop fiber was strengthened. And then, $Tr^{\mathrm{drop}}_{\mathrm{max}}$ exhibit its maximum value of 60 % at $d_{\mathrm{drop}} = 0.56$ nm. Figure 5.8(b) also shows similar behaviors of the coupling to that shown in Fig. 5.8(a), but it is slightly different. In this case the cavity and bus fiber were strongly over-coupled, thus $d_{\mathrm{drop}}$ had to be set at very close to the cavity for satisfying critical coupling condition of the bus fiber. As a result, the drop fiber contacted to the cavity before $Tr^{\mathrm{bus}}_{\mathrm{min}}$ took its minimum value. In addition, the bus and the drop fibers could be more strongly over-coupled to the

[*c]The results were normalized by the transmittance from the bus fiber when there was no coupling to the cavity. This means that splice loss of optical fiber was excluded. At that time it was 1.3 dB.

cavity in this situation than the situation in Fig. 5.8(a). Hence $Tr_{\max}^{\mathrm{drop}}$ reaches to 68 %. However, as described in 3.1.2, stronger over-coupling inevitably results in reduction of $Q_{\mathrm{load}}$. Figure 5.8(c) shows that $Q_{\mathrm{load}}$ depends on $d_{\mathrm{drop}}$. Red and black dots were obtained from estimated by the spetctra of $Tr^{\mathrm{bus}}$ and $Tr^{\mathrm{drop}}$, respectively. The graph clearly shows that the coupling is stronger (i.e. $d_{\mathrm{drop}}$ reduced) when $Q_{\mathrm{load}}$ became lower. In addition, $Q_{\mathrm{load}}$ was much larger at $d_{\mathrm{bus}} = 800$ nm than at $d_{\mathrm{bus}} = 600$ nm. $Q_{\mathrm{load}}$s at the point where $Tr_{\max}^{\mathrm{drop}}$ is maximum are $1.8 \times 10^6$ ($d_{\mathrm{drop}} = 800$ nm) and $9 \times 10^4$ ($d_{\mathrm{drop}} = 600$ nm). Thus, as predicted in 3.1.2, I couclude that there are trade-off between $Q_{\mathrm{load}}$ and $Tr_{\max}^{\mathrm{drop}}$.

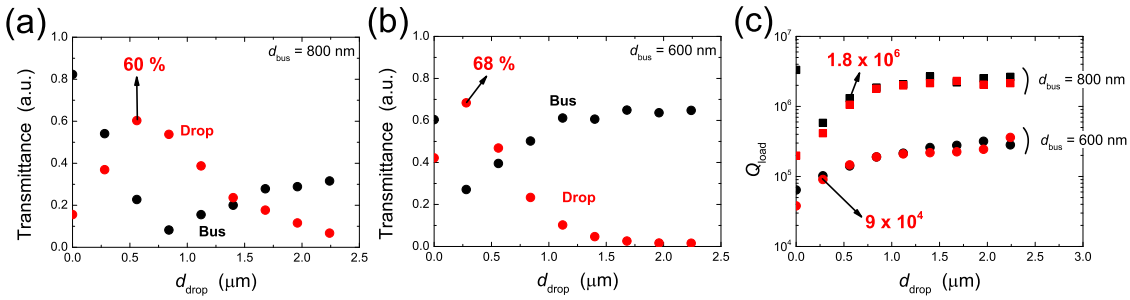


Fig. 5.8: $Tr_{\min}^{\mathrm{bus}}$ and $Tr_{\max}^{\mathrm{drop}}$ ((a) and (b)), and $Q_{\mathrm{load}}$ (c) for different $d_{\mathrm{drop}}$ values. $d_{\mathrm{bus}}$ was set at (a) 800 nm and (b) 600 nm. Black and red dots represent bus and drop, respectively.

Finally,I show the signal transmitted from the bus and drop fibers in the time regime in Fig. 5.9. When the signal from bus fiber drops (around 120 ns), the signal from drop fiber rises. In addition, $Tr_{\max}^{\mathrm{drop}}$ of 44 % and 65 % were obtained for $d_{\mathrm{bus}}$ of 800 nm and 600 nm.

The transmittance obtained here is lower than those reported in an add-drop system based on bottle microcavity[18] and silica toroid microcavity,[28] which reached over 90 %. The reason on this is due to the loss of the drop fiber. The loss of a drop fiber was 3 dB, which I believe is due to the splice loss and the contaminants on its surface. This is because there was no loss originated from bending loss as shown in Fig. 5.3. Therefore, by improving taper-fiber fabrication process, transmittance should improve. In fact, the transmittance of a straight taper fiber of 99.4 % was achieved by optimizing taper fiber fabrication in the previous study.[98]

### 5.2.2 Switching operation in an add-drop system

Here, the results of switching experiments with an add-drop system is described. Figure 5.10 shows the experimental setup for an add-drop system. This setup is similar to the setup shown in Fig. 4.8. However, there are some differences. First, L-band EDFA is placed to amplify signal light. Second, there is only one set of PWM and OSO in our lab, thus I switch the connection manually for observing the signal from bus and drop fibers in turn.

Figure 5.11 shows the switching operation in an add-drop system. The wavelength of the probe light was initially tuned to the resonance in Fig. 5.11. $Q_{\mathrm{load}}^{\mathrm{cont}} = 3.4 \times 10^6$

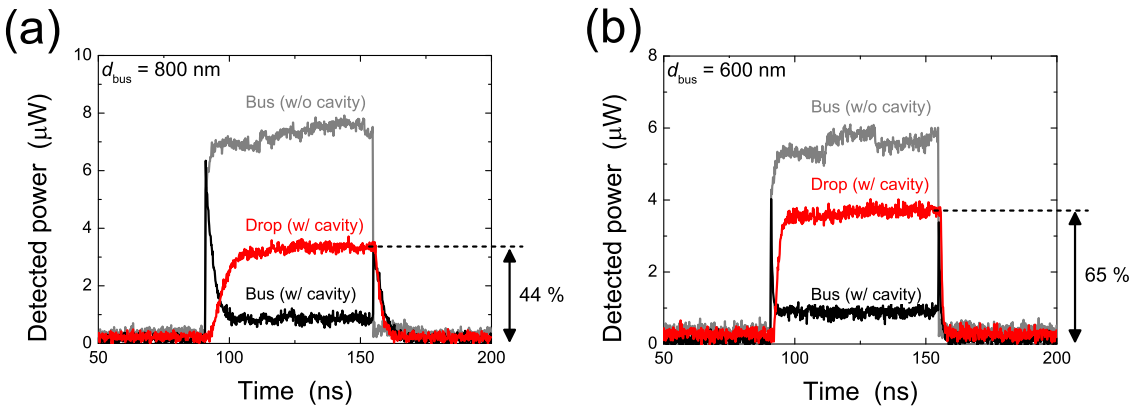


Fig. 5.9: Signal transmitted from the bus and drop fibers for (a) $d_{\text{bus}} = 800$ nm and (b) $d_{\text{drop}} = 600$ nm. Gray, black and red solid lines represent the signal transmitted from the bus fiber without and with the cavity, and the signal transmitted from the drop fiber with the cavity.

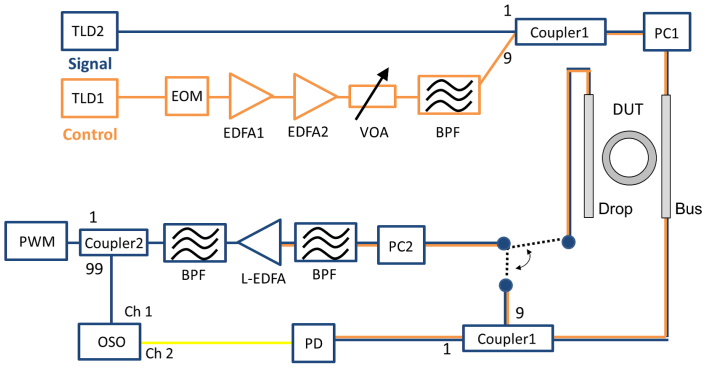


Fig. 5.10: Experimental setup for optical switch in an add-drop system.

($\lambda_{\rm cont}$ = 1546.448 nm) and $Q^{\rm sig}_{\rm load} = 3.2\times10^6$ ($\lambda_{\rm sig}$ = 1560.207 nm) were used. Peak power of pulse was 63 mW and control pulse cycle $T_{\rm cycle}$ was 64 ns. Black and red solid lines in the figure indicate the transmitted signal light from a bus and a drop fibers, respectively. Both lights from bus and drop fibers were amplified by L-band EDFA.

Figure 5.11 clearly shows successful switching of two signals. When bus signal is "high," drop signal drops to "low" state. This is because signal wavelength is tuned near the cavity resonance. When control pulse is not inputted, the transmittance of bus fiber is low because the cavity is at the resonance. As for bus fiber, the transmittance becomes high because energy is stored in the cavity. On the other hand, when control pulse is inputted and the cavity resonant wavelength is shifted, the transmittance of bus fiber recovers because the signal wavelength do not longer is at the resonant wavelength. This deceases transmittance of the drop fiber, because light energy is barely stored in the microcavity in this situation. Therefore, transmission from drop fiber has an inverted waveform in comparison with that from the bus fiber.

Next, I confirmed that switching behavior shown in Fig. 5.10 was due to Kerr effect. This because the modulation cycle of the control light is sufficiently small. As shown in Fig. 4.12, TO effect does not dominate Kerr effect when $T_{\rm cycle}$ is smaller than 256 ns. The experiments I conducted here employ $T_{\rm cycle}$ of 64 ns, TO effect is sufficiently small in this situation. Note that presence of an drop waveguide does not contribute to the absorption according to Eq. (3.6). It just introduces additional coupling term $\tau_{\rm drop}$. Hence, situation related to the absorption in an add-drop system is not different from that in an side-coupled system. Considering the discussion above, I conclude that switching shown in this section is purely due to the Kerr effect. It is worth mentioning that this is the first demonstration of an optical path switch that is driven by Kerr effect and is based on microcavity fabricated on a chip.

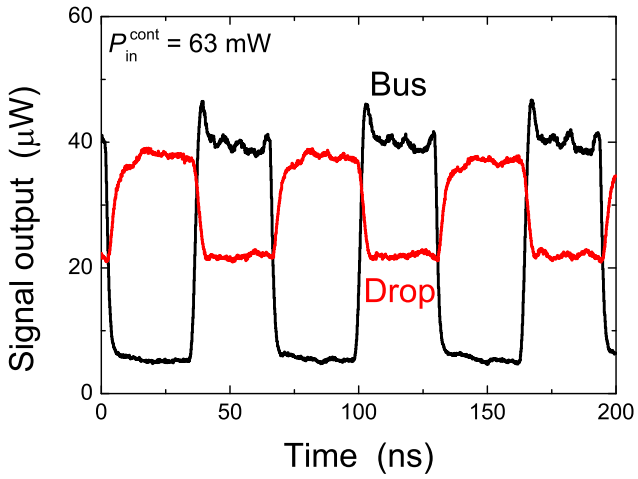


Fig. 5.11: Switched signal light transmitted from the bus and drop fibers. The black and red solid lines represent the light from the bus and the drop fibers.

## 5.3 Summary

In this chapter, study on optical switch using an add-drop system was described. First, the strategy for developing an add-drop system was shown. I explained that a bent taper is necessary as a drop fiber to avoid the interference between the bus and the drop fibers. Second, I described how I fabricated the bent taper fiber. Bent taper fiber was easy to fabricate by bending by hand. In addition, I showed that bending loss was negligible. Third, an stage system for add-drop system was designed and developed. Finally, I showed the results of switching operation using an add-drop system. By carefully adjusting the position and the diameter of the bus and the drop fibers, I achieved transmission of 60 % and $Q_{\mathrm{load}}$ of $1.8 \times 10^6$. In addition, I successfully demonstrated optical switch in an add-drop system and I showed that switching was purely based on the Kerr effect.

As mentioned in 1.4.2, there are different optical switches, which have negligible insertion loss,[65,12] but they do not have a function of optical path switching (i.e. add-drop system). Moreover, to the best of my knowledge, there is only one optical add-drop switch with negligible insertion loss,[18] but it is difficult to be integrated on a chip. Therefore, my optical switch is advantageous in terms of optical path switching on-a-chip fabrication. This study will provide an important step for achieving all-optical few-photon level telecommunication.

# Chapter 6

# Conclusion

In this thesis, I demonstrated an all-optical on-chip switch based on Kerr nonlinearity in a silica toroid microcavity. By using a silica toroid microcavity, I achieved microcavity-based switch with low insertion loss. Silica toroid microcavity couples to a taper fiber with negligible loss and the transmittance of the fabricated taper fiber reached 95 %. Eventually, optical switch demonstrated in this study had very low insertion loss. Moreover, it should be emphasized that optical switch in this study was fabricated on a semiconductor substrate. This characteristic is very important for integrating optical switches in the future. In addition, by suppressing the influence from TO effect, I was able to employ Kerr effect. As a result, I obtained optical switching with high switching speed thanks to instantaneous response of Kerr effect. Furthermore, my optical switch drives with switching power of approximately 800 $\mu$W, which is the lowest among [all optical Kerr switches fabricated on a chip. Low switching power is essential for reducing the power consumption of optical network. Finally, I developed an add-drop system and demonstrated optical path switching. This is first time to demonstrate optical path switching driven by Kerr effect using microcavity fabricated on a chip. Optical path switching function is necessary to place optical switch into all-optical router in a practical optical network.

There are some optical switches with negligible insertion loss, which are based on an a-Si:H cavity,[65] a silica bottle cavity[18] and a highly nonlinear fiber.[12] However, they are difficult to fabricate on a chip. On the other hand, some on-chip optical switches using Kerr effect were previously reported,[15,67,21] but they suffer from the coupling loss between them and fiber and require switching power of over 10 mW In addition, although add-drop system based on a silica toroid microcavity has already been developed,[77,28] they exhibit only a passive operation (i.e. add-drop filter). Therefore, to the best of my knowledge, there have been no optical switch which satisfies the characteristics that my optical switch achieved. I believe that optical switch studied in this thesis will contribute to the reduction of energy consumption in a optical telecommunication and future development of a few-photons-based optical telecommunication network.

# Appendix A

# Equipments and instruments used for experiments

- TLD1 (Tunable laser diode #1): TSL-510 (Santec)
- TLD2 (Tunable laser diode #2): TSL-710 (Santec)
- EOM (Electro-optical modulator): - (PriTel)
- EDFA1 (Erbium-doped fiber amplifier #1): LNHP-PMFA-20 (PriTel)
- EDFA2 (Erbium-doped fiber amplifier #2): FA-30-IO (PriTel)
- L-band EDFA (L-band erbium-doped fiber amplifier): LNHP-PMFA-18-L (PriTel)
- PPG1 (Pulse pattern generator #1): WF1947 (NF)
- PPG2 (Pulse pattern generator #2): 81134A (Agilent)
- Coupler1 (10:90 coupler): WSCJ10B252210S (Alnair Labs)
- Coupler2 (1:99 coupler): WSCJ10B292210S (Alnair Labs)
- PC1 (Polarization controller #1): FPC560 (Thorlabs)
- PC2 (Polarization controller #2): MLC-15-PQH-SM-SS (Alnair Labs)
- BPF (Band pass filter): TFF-15-1-PL-L-100-SS (Alnair Labs)
- VOA (Variable optical attenuator): DA-100-3A-1550-8/125-P-60 (OZoptics)
- OSO (Optical sampling oscilloscope): 86100A (Agilent)
- PWM (Power meter): 8163B (Agilent)
- PD (Photo Detector): 1411-50 (New Focus)
- ESA (Electrical spectrum analyzer): R3265A (Advantest)

# Appendix B

# Calculation model of optical Kerr switch

Here, calculation model for an optical Kerr switch is described. The model shown in this section is similar to that described in W. Yoshiki and T. Tanabe.[35] I assume a side-coupled system for simplicity but it can be easily applied for an add-drop system.

As mentioned before, the mode amplitude $a$ in the microcavity is expressed by Eq. (3.1). I employ slow varying envelope (SVE) approximation for simply expressing the temporal behavior of $a$, given as,

$$a(t) = A(t)\exp(j\omega t), \tag{B.1}$$
$$s_{\mathrm{in}} = S_{\mathrm{in}}(t)\exp(j\omega t). \tag{B.2}$$

By substituting Eqs. (B.1) and (B.2), Eq. (3.1) is rewritten as,

$$\begin{aligned}\frac{\mathrm{d}A(t)}{\mathrm{d}t} &= \left[j(\omega_0-\omega)-\frac{1}{2\tau_{\mathrm{load}}}\right]A(t)+\sqrt{\frac{1}{\tau_{\mathrm{coup}}}}\exp(j\theta)S_{\mathrm{in}}(t).\\ &= \left[j2\pi c(\frac{1}{\lambda_0}-\frac{1}{\lambda})-\frac{1}{2\tau_{\mathrm{load}}}\right]A(t)+\sqrt{\frac{1}{\tau_{\mathrm{coup}}}}\exp(j\theta)S_{\mathrm{in}}(t).\end{aligned} \tag{B.3}$$

Note that $A(t)$ do not oscillate at an angular frequency $\omega$, thus I can use time step $\Delta t$ which is much longer than $2\pi/\omega_0$. This allows us to reduce the calculation time. For taking the nonlinear effect (i.e. influence from $\Delta n_{\mathrm{Kerr}}$) into account, I replace $\lambda_0$ by $\lambda_0' = \frac{n_0+\delta n_{\mathrm{Kerr}}}{n_0}\lambda_0$. $\lambda_0'$ considers the wavelength shift due to the refractive index change induced by the Kerr effect. Hence we can model the nonlinear behavior by replacing $\lambda_0$ by $\lambda_0'$ with Eq. (B.3).

Equation (B.3) can be directly used to model the one-wavelength scheme as shown in 4.3.1. However, for using Eq. (B.3) for modeling the two-wavelength scheme, it is necessary to consider both signal and control mode amplitudes ($A_{\mathrm{sig}}$, $A_{\mathrm{cont}}$). According

to Eq. (B.3), equations for $A_{\rm sig}$ and $A_{\rm cont}$ is written as follows;

$$\frac{{\rm d}A_{\rm sig}(t)}{{\rm d}t} = \left[ j2\pi c(\frac{1}{\lambda_0+\delta\lambda_{\rm sig}} - \frac{1}{\lambda_{\rm sig}}) - \frac{1}{2\tau^{\rm sig}_{\rm load}} \right] A_{\rm sig}(t) + \sqrt{\frac{1}{\tau^{\rm sig}_{\rm coup}}} \exp(j\theta) S^{\rm sig}_{\rm in}(t), \tag{B.4}$$

$$\frac{{\rm d}A_{\rm cont}(t)}{{\rm d}t} = \left[ j2\pi c(\frac{1}{\lambda_0+\delta\lambda_{\rm cont}} - \frac{1}{\lambda_{\rm cont}}) - \frac{1}{2\tau^{\rm cont}_{\rm load}} \right] A_{\rm cont}(t) + \sqrt{\frac{1}{\tau^{\rm cont}_{\rm coup}}} \exp(j\theta) S^{\rm cont}_{\rm in}(t). \tag{B.5}$$

These equations are independent each other in the linear regime, but are not in the nonlinear regime; they are connected by $\delta\lambda_{\rm sig}$ and $\delta\lambda_{\rm cont}$. If cross-sectional distributions of control and signal modes are the same, $\delta\lambda_{\rm cont}$ is equal to $\delta\lambda_{\rm sig}$. However, if their spatial distribution are same, it is necessary to consider spatial overlap of these two WGMs. By taking the overlap into account and using Eq. (4.9), the signal wavelength shift $\delta\lambda_{\rm probe}$ is written, as[*a],

$$\begin{aligned} \delta\lambda_{\rm sig} &= \iint \Delta n^{\rm cont}_{\rm Kerr}(r,z)\tilde{I}_{\rm sig}(r,z){\rm d}S \\ &= \frac{n_2 c}{n_0 \pi R} U^{\rm cont}_{\rm cavity} \iint I_{\rm cont}(r,z) I_{\rm sig}(r,z){\rm d}S. \end{aligned} \tag{B.6}$$

By employing Eqs. (B.4)- (B.6), I can numerically describe the switching operation.

[*a] Usually the signal light is much weaker than the control light. Thus, the influence of the signal light on the nonlinear wavelength shift is negligible.

# Appendix C

# Optomechanically-induced oscillation

During the Kerr switching experiment, I found that the output light suddenly began to oscillate when high input power was inputted into a cavity. In this section, I investigate what this oscillation is originating from by performing some experiments.

First, I show the oscillatory behavior observed during experiments. Figure C.1(a) shows that output signal when I inputted different powers into the microcavity. The black and red lines represent the output powers when the input wavelength is detuned from the resonance and tuned on the resonance. This graph clearly shows that when input power exceeds around 1.23 mW, the output signal began to oscillate. Thus it is obvious that these oscillations have obvious threshold. In addition, when the input wavelength was equal to the resonance, oscillatory behavior does not occur. So, it is necessary to detune the input wavelength from the resonance for observing oscillatory behavior. For further analyzing, I measured the output signal for different detunings. The result is shown in Fig. C.1(b). When the input wavelength is blue-detuned far from the resonance (FT = 11), no oscillation is not observed. On the other hand, when FT is smaller than 7 the output powers show oscillatory behavior. And then, when FT = $-7$ there is no oscillation as same as the case of FT = 11. The dependency on the detuning in Fig. C.1(b) is coincidence with the result in Fig. C.1(a).

Considering the obtained data, here I analyze the origin of this oscillatory behavior. Firstly, I doubted that the origin was FWM. There was a possibility that interference between the signal wave and the wave generated by the FWM creates oscillation. However, at that time input power was much smaller than the threshold of FWM.[31] Thus the origin did not seem to be FWM. Secondly, I thought that chaotic behavior based on optical bistability[111] was the cause of the oscillation. However, the input wavelength was blue-detuned, which is out of the bistable regime. Thus it is clear that the oscillatory behavior was not originating from the chaos based on optical bistability. Finally, I reached to the conclusion that the oscillatory behavior is due to the mechanical motion induced by the radiation pressure of the light energy in the cavity, which is now intensively being studied as "optomechanics.[62,112]" In the microcavity with high $Q$ factor, photon density is largely enhanced. As a result, radiation pressure of the circulating light become very large, and then it deforms and shakes the structure of the microcavity.

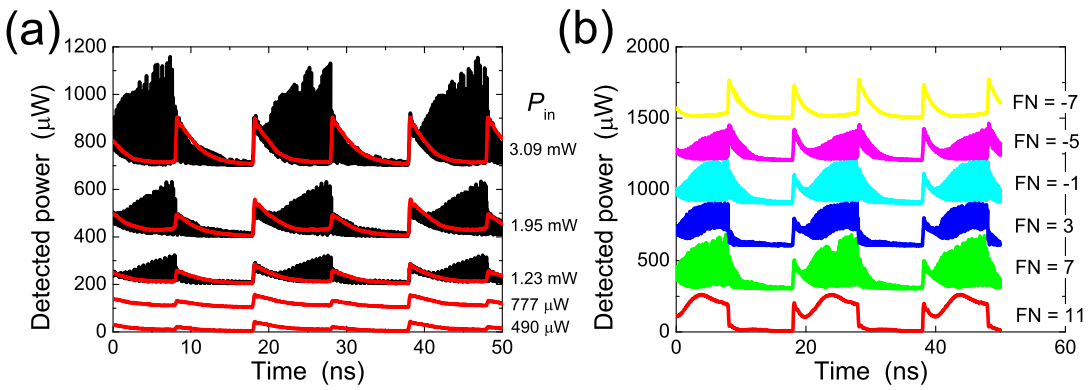


Fig. C.1: Oscillatory behaviors in output signals for (a) different input powers and (b) different detunings. Black line represents output signal when there is no cavity. Note that "FT" stands for "fine tuning" which corresponds to the wavelength (Smaller FT corresponds to longer wavelength).

This deformation changes the optical path length in the microcavity. The change of the optical path reflects on the change of the wavelength of the light which circulates in the microcavity.[108] The light with modulated wavelength interferes to the light with initial wavelength in the waveguide, then oscillation occurs[*a]. T. Carmon *et al.*[108] reported that the threshold of the mechanical motion was smaller than that of the other nonlinear process. This is the same behavior of the data shown in C.2(a) and (b). In addition, the behavior of optomechanical coupling changes depending on the detuning.[112] As a result of the thermal vibration of the cavity structure, the frequency of cavity mode $\omega$ is modulated by the mechanical frequency $\omega_m$. This creates anti-stokes ($\omega_{\mathrm{AS}} = \omega + \omega_m$) and stokes sidebands ($\omega_{\mathrm{S}} = \omega - \omega_m$). When the input frequency is blue-tuned (i.e. $\omega > \omega_0$), stokes field is on near resonance while anti-stokes field is far off resonance [*b]. As a result, the stokes light is strengthened by the resonance, but the anti-stokes light is weakened because it does not resonates with the cavity. According to the equation of photon energy $\hbar\omega$, the light energy in the cavity is reduced in this situation because amplitude of stokes light (having smaller energy) is much larger than that of anti-stokes light (having larger energy). This situation violates energy conservation law, thus it reduced optical energy must be converted into mechanical energy. Therefore, when input is blue-tuned the mechanical vibration is amplified("amplification"). On the other hand, obviously, mechanical vibration is suppressed when input is red-tuned ("cooling"). This physics coincident with the result shown in Fig. C.1(b), where the oscillations occurs when the input wavelength is detuned from the resonance.

For confirming whether or not oscillatory behavior is originating from the optomechanical motion, I decided to analyze the frequency of the oscillation in the output. As reported in T. Kippenberg *et al.*,[113] the signal outputted from the cavity has frequencies

[*a] In general Optomechanically-induced oscillation oscillates periodically.[108] However the results shown in Fig. C.1(a) and (b) look like chaotic because these results were obtained by using OSO.

[*b] I assume that $\omega_m$ is smaller than the cavity resonance linewidth.

in RF regime that correspond to mechanical eigenfrequencies of the cavity structure. On the other hand, when the input power increases and exceeds a threshold, the RF spectrum becomes continuous (see Fig. 2 in T. Carmon *et al.*[114]). Thus I examined whether or not same behavior was observed in my microcavity. Figure C.2(a) shows the experimental setup for measuring RF spectrum of the light outputted from the cavity system. I obtained RF spectrum by using electrical spectrum analyzer (ESA). OSO was used to confirm that the input light was efficiently coupled to the microcavity. I swept input power and record the RF spectra. I started from the input power of smaller than 1 $\mu$W, which was too low to be directly detected by the detectors. Thus, I placed EDFA at the output and kept the output power constant during the experiments. The silica toroid microcavity was carefully fabricated to have a thin Si pillar (Fig. C.2(b)) and $Q_{\mathrm{load}} = 4.3 \times 10^7$ was used for lowering the threshold of the optical-mechanical coupling.

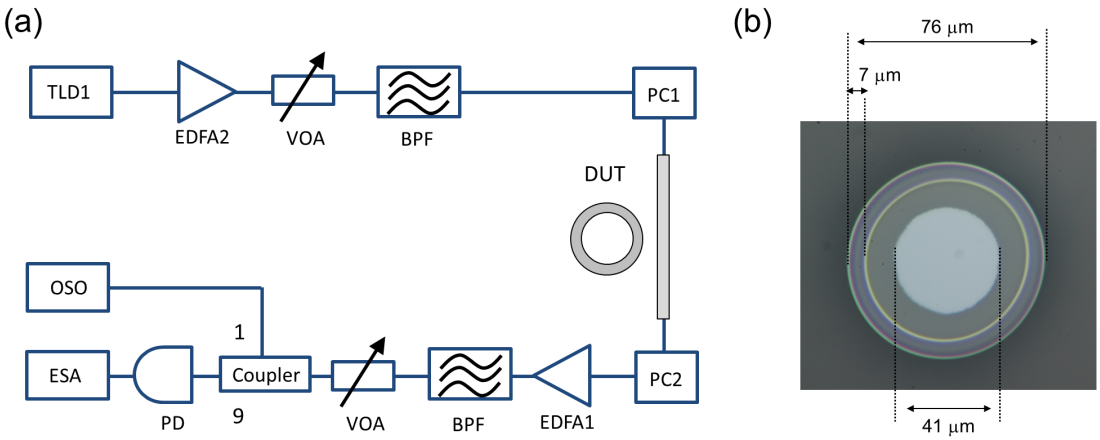


Fig. C.2: (a) Experimental setup for analyzing RF spectrum of the output light. (b) The picture of silica toroid microcavity I used for the experiment.

Figure C.3(a) and (b) show the measured output power and the RF spectra. As can be seen in Fig. C.3(a), the output signal begins to oscillate when the input power is higher than 20 $\mu$W[*c]. This behavior is coincidence with Fig. C.3(b). When the input power is lower than 10 $\mu$W, there is a few number of peaks which correspond to the mechanical eigenfrequencies of the structure. These peaks in the RF spectra are independent on the input power, thus input power does not exceed the threshold for optical-mechanical coupling. On the other hand, the mode with the frequency of 5 MHz is amplified and its harmonics[113] is observed when the input power exceeds 20 $\mu$W. Moreover, the spectrum

[*c]The output signal seems to oscillate slowly even when the input power is smaller than 10 $\mu$W. This oscillation is originating from the instability of the measurement condition. In this experiments I used a microcavity with $Q_{\mathrm{load}} \approx 4 \times 10^7$, that corresponding extremely narrow resonance of 40 fm. As a result, the output signal is very sensitive to the experimental noises such as instability of TLD's frequency, thermal noises and the vibration from the environment.

reaches continuous when the input power is 5.0 mW. This behavior is similar to that reported in T. Carmon *et al.*[114] Thus I conclude that optomechanical oscillation occurs in my system when input power is higher than 20 $\mu$W. It is worth noting that the threshold of optomechanical oscillation is greatly depending on the cavity structure. This allows us to suppress the optomechanical oscillation by carefully controlling the size of the silica toroid microcavity.

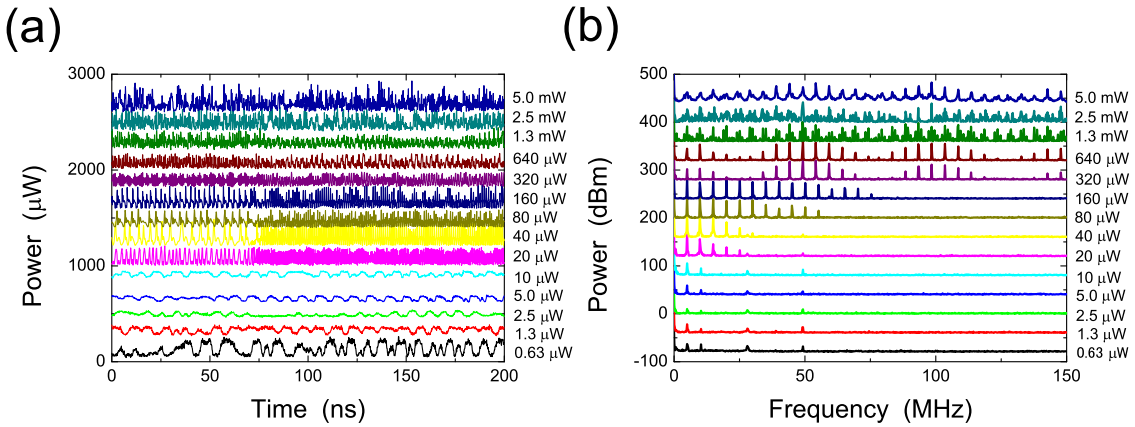


Fig. C.3: Measured (a) output signal and (b) RF spectra for different input power.

# Appendix D

# Experimental estimation of an absorption coefficient

Ideally, absorption coefficient of silica is extremely small,[3,22] thus TO effect is negligible.[35] However, as shown in Fig. 4.9(b), influence from TO effect is found; this result indicates that actual absorption coefficient is much larger than the value in the bulk material. To the present some papers experimentally revealed that absorption loss is enhanced due to surface water layer or surface contaminants.[80,58] So, I characterize the photon lifetime related to the absorption loss $\tau_{\mathrm{abs}}$ (corresponding to absorption coefficient $\alpha$) for further analyzing influence of TO effect.

According to Eq. (4.6), $\Delta T$ is calculated by multiplying $U_{\mathrm{cavity}}$ by$C_{\mathrm{heat}}/\tau_{\mathrm{abs}}$. In addition, Eq. (4.6) also indicates that I can calculate $C_{\mathrm{heat}}$ by obtaining relation between $\Delta T$ and $Qs = U_{\mathrm{cavity}}/\tau_{\mathrm{abs}}$. Thus, I can estimate $\tau_{\mathrm{abs}}$ by dividing the obtained $C_{\mathrm{heat}}$ by the obtained $C_{\mathrm{heat}}/\tau_{\mathrm{abs}}$.

I investigate static resonant wavelength shift induced by TO effect for obtaining $\Delta T$ and $U_{\mathrm{cavity}}$ as shown in Fig. D.1(a). I scanned wavelength over resonance around 1544.08 nm several times by using different input power $P_{\mathrm{in}}$ from 11.9 $\mu$W to 376 $\mu$W. As input power $P_{\mathrm{in}}$ increases, wavelength shift $\delta\lambda$ is larger and the shape of resonance exhibits deformation. This is because $U_{\mathrm{cavity}}$ is build up and resonance shift is enhanced as input wavelength approaches to the resonance.[99] From this graph, I can calculate $\Delta T$ by using Eq. (4.3). In addition, $U_{\mathrm{cavity}}$ is calculated by using Eq. (4.2). Figure D.1(b) shows the relation between $U_{\mathrm{cavity}}$ and $\Delta T$. As predicted in Eq. (4.6), $\Delta T$ is almost in proportion to $U_{\mathrm{cavity}}$. By using least-squares method, $C_{\mathrm{heat}}/U_{\mathrm{cavity}} = 8.08 \times 10^{11}$ is obtained.

Next, I try to obtain $C_{\mathrm{heat}}$. For this I used COMSOL muiltiphysics, commercial FEM solver. The model used in the FEM solver is shown in Fig. D.2(a). By using this solver, I obtain $\Delta T$ by inputting the heat source $Q_{\mathrm{heat}} = U_{\mathrm{cavity}}/\tau_{\mathrm{abs}}$ (Note that $\Delta T = C_{\mathrm{heat}}Q_{\mathrm{heat}}$). As a result, we calculate $C_{\mathrm{heat}}$ as 37288 by obtaining the relation between $\Delta T$ and $Q_{\mathrm{heat}}$ as shown in Fig. D.2(b). Here I calculate that $Q_{\mathrm{abs}} = \omega_0\tau_{\mathrm{abs}}$ is $5.6 \times 10^7$ by using obtained $U_{\mathrm{cavity}}/\tau_{\mathrm{abs}}$ and $C_{\mathrm{heat}}$, and thus values is much smaller than the value predicted by the material absorption $Q_{\mathrm{mat}} = 2 \times 10^{11}$[22][*a]. The main cause of

[*a]The calculated value is approximately three times smaller than that assumed in 4.2.2. This might

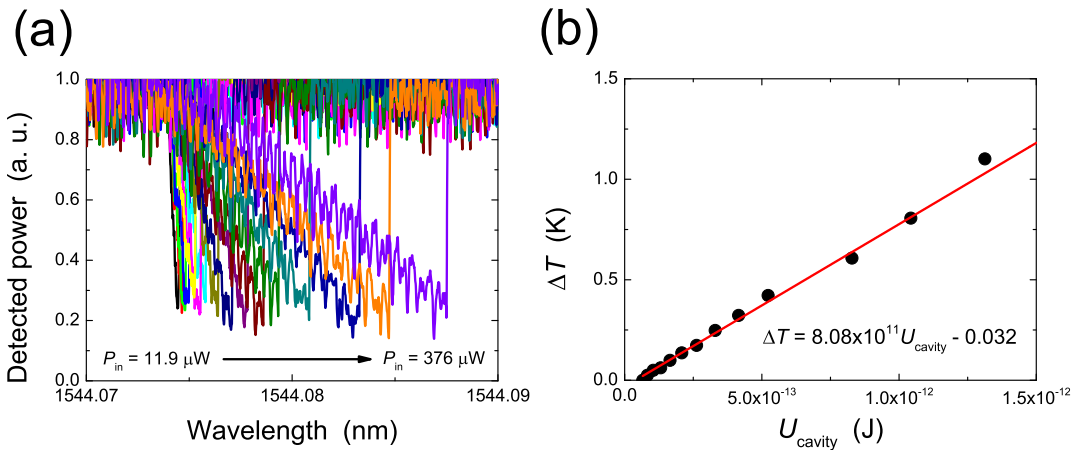


Fig. D.1: (a) Resonant wavelength shift induced by TO effect. The loaded $Q$ of the mode is $Q_{\mathrm{load}} = 8.62 \times 10^5$. (b) Relation between $U_{\mathrm{cavity}}$ and $\Delta T$. The black dots and the red solid curve are measured data and fitted curve, respectively.

this is, what I believe, due to the absorber on the cavity surface as pointed out in some references.[105,106,107] $Q_{\mathrm{abs}}$ shown in these references are spread from $10^7$ to $10^{10}$ due to uncertainty of thickness of surface absorber.[107] Thus I cannot accurately judge whether our calculated values are correct or not, but the value appears to be reasonable compared with the data in references. Such a low-$Q_{\mathrm{abs}}$ indicates that unwanted large TO effect is present during optical switching experiment, and this agrees with the result in 4.3.2.

be due to the due to the mode mismatch between the pump and probe light in Fig. 4.4.

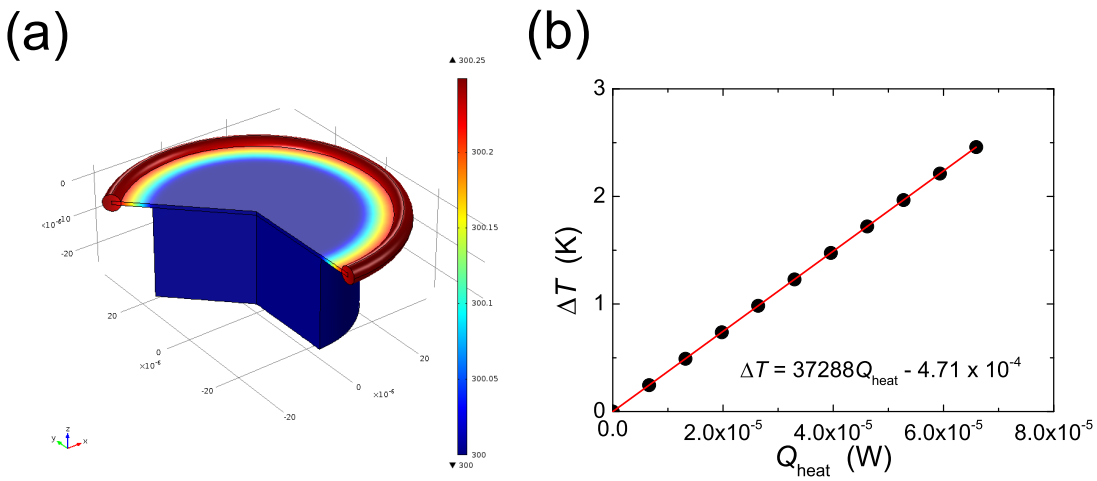


Fig. D.2: (a) The model used in the FEM solver. (b) Relation between $\Delta T$ and $Q_{\text{heat}}$ calculated by COMSOL muiltiphysics. The black dots and the red solid curve are calculated data and fitted curve, respectively.

# References


[1] Ministry of Internal Affairs and Communications of Japan, "2012 white paper information and communication in japan," (2012).

[2] R. Tucker, "A green internet," *in conference proceeding of 21st Annual Meeting of the IEEE Lasers and Electro-Optics Society(LEOS 2008)*, (Newport Beach, USA, 2008), pp. 4–5.

[3] T. Miya, Y. Terunuma, T. Hosaka, and T. Miyashita, "Ultimate low-loss single-mode fibre at 1.55 $\mu$m," Electron. Lett. **15**, 106–108 (1979).

[4] M. Fujiwara, M. Takeoka, J. Mizuno, and M. Sasaki, "Exceeding the classical capacity limit in a quantum optical channel," Phys. Rev. Lett. **90**, 167906 (2003).

[5] N. Gisin, G. Ribordy, W. Tittel, and H. Zbinden, "Quantum cryptography," Rev. Mod. Phys **74**, 145–195 (2002).

[6] J. L. O'Brien, "Optical quantum computing," Science **318**, 1567–1570 (2007).

[7] K. Shimizu, T. Honjo, M. Fujiwara, T. Ito, K. Tamaki, S. Miki, T. Yamashita, H. Terai, Z. Wang, and M. Sasaki, "Performance of long-distance quantum key distribution over 90-km optical links installed in a field environment of tokyo metropolitan area," J. Lightwave Technol. **32**, 141–151 (2014).

[8] G. W. Cong, R. Akimoto, K. Akita, T. Hasama, and H. Ishikawa, "Low-saturation-energy-driven ultrafast all-optical switching operation in (CdS/ZnSe)/BeTe intersubband transition," Opt. Express **15**, 12123–12130 (2007).

[9] K. Nishimura, R. Inohara, M. Tsurusawa, and M. Usami, "80 Gbit/s wavelength conversion using MQW electroabsorption modulator in delayed-interferometric configuration," Electron. Lett. **39**, 792–794 (2003).

[10] Y. Liu, E. Tangdiongga, Z. Li, S. Zhang, H. de Waardt, G. Khoe, and H. Dorren, "Error-free all-optical wavelength conversion at 160 Gb/s using a semiconductor optical amplifier and an optical bandpass filter," J. Lightwave Technol. **24**, 230–236 (2006).

[11] K. Stubkjaer, "Semiconductor optical amplifier-based all-optical gates for high-speed optical processing," IEEE J. Sel. Top. Quant. Electron. **6**, 1428–1435 (2000).

[12] P. A. Andrekson, H. Sunnerud, S. Oda, T. Nishitani, and J. Yang, "Ultrafast, atto-Joule switch using fiber-optic parametric amplifier operated in saturation," Opt. Express **16**, 10956–10961 (2008).

[13] K. Parameswaran, M. Fujimura, M. Chou, and M. Fejer, "Low-power all-optical gate based on sum frequency mixing in APE waveguides in PPLN," IEEE Photonics Technol. Lett. **12**, 654–656 (2000).

[14] H. Nakamura, Y. Sugimoto, K. Kanamoto, N. Ikeda, Y. Tanaka, Y. Nakamura, S. Ohkouchi, Y. Watanabe, K. Inoue, H. Ishikawa, and K. Asakawa, "Ultra-fast photonic crystal/quantum dot all-optical switch for future photonic networks," Opt. Express **12**, 6606–6614 (2004).

[15] C. Lacava, M. J. Strain, P. Minzioni, I. Cristiani, and M. Sorel, "Integrated nonlinear mach zehnder for 40 gbit/s all-optical switching," Opt. Express **21**, 21587–21595 (2013).

[16] K. Nozaki, T. Tanabe, A. Shinya, S. Matsuo, T. Sato, H. Taniyama, and M. Notomi, "Sub-femtojoule all-optical switching using a photonic-crystal nanocavity," Nat. Photonics **4**, 477–483 (2010).

[17] V. Almeida, C. Barrios, R. Panepucci, M. Lipson, M. Foster, D. Ouzounov, and A. Gaeta, "All-optical switching on a silicon chip," Opt. Lett. **29**, 2867–2869 (2004).

[18] M. Pöllinger and A. Rauschenbeutel, "All-optical signal processing at ultra-low powers in bottle microresonators using the Kerr effect," Opt. Express **18**, 17764–17775 (2010).

[19] J. Ford, V. Aksyuk, D. Bishop, and J. Walker, "Wavelength add-drop switching using tilting micromirrors," J. Lightwave Technol. **17**, 904–911 (1999).

[20] K. Ikeda and Y. Fainman, "Material and structural criteria for ultra-fast Kerr nonlinear switching in optical resonant cavities," Solid-State Electron. **51**, 1376–1380 (2007).

[21] V. Eckhouse, I. Cestier, G. Eisenstein, S. Combriè, G. Lehoucq, and A. D. Rossi, "Kerr-induced all-optical switching in a GaInP photonic crystal Fabry-Perot resonator," Opt. Express **20**, 8524–8534 (2012).

[22] A. Savchenkov, V. Ilchenko, A. Matsko, and L. Maleki, "Kilohertz optical resonances in dielectric crystal cavities," Phys. Rev. A **70**, 051804 (2004).

[23] J. C. F. Matthews, A. Politi, A. Stefanov, and J. L. O'Brien, "Manipulation of multiphoton entanglement in waveguide quantum circuits," Nat. Photonics **3**, 346–350 (2009).

[24] B. Dayan, A. S. Parkins, T. Aoki, E. P. Ostby, K. J. Vahala, and H. J. Kimble, "A photon turnstile dynamically regulated by one atom," Science **319**, 1062–1065 (2008).

[25] N. Matsuda, R. Shimizu, Y. Mitsumori, H. Kosaka, and K. Edamatsu, "Observation of optical-fibre Kerr nonlinearity at the single-photon level," Nat. Photonics **3**, 95–98 (2009).

[26] V. Ilchenko, A. Savchenkov, A. Matsko, and L. Maleki, "Whispering-gallery-mode electro-optic modulator and photonic microwave receiver," J. Opt. Soc. Am. B **20**, 333–342 (2003).

[27] K. Vahala, "Optical microcavities," Nature **424**, 839–846 (2003).

[28] H. Rokhsari and K. Vahala, "Ultralow loss, high Q, four port resonant couplers for quantum optics and photonics," Phys. Rev. Lett. **92**, 253905 (2004).

[29] K. Nozaki, A. Shinya, S. Matsuo, Y. Suzaki, T. Segawa, T. Sato, Y. Kawaguchi, R. Takahashi, and M. Notomi, "Ultralow-power all-optical RAM based on nanocavities," Nat. Photonics **6**, 248–252 (2012).

[30] T. J. Kippenberg, J. Kalkman, A. Polman, and K. J. Vahala, "Demonstration of an erbium-doped microdisk laser on a silicon chip," Phys. Rev. A **74**, 051802 (2006).

[31] T. Kippenberg, S. Spillane, and K. Vahala, "Kerr-nonlinearity optical parametric oscillation in an ultrahigh-Q toroid microcavity," Phys. Rev. Lett. **93** (2004).

[32] K. Takeda, T. Sato, A. Shinya, K. Nozaki, W. Kobayashi, H. Taniyama, M. Notomi, K. Hasebe, T. Kakitsuka, and S. Matsuo, "Few-fJ/bit data transmissions using directly modulated lambda-scale embedded active region photonic-crystal lasers," Nat. Photonics **7**, 569–575 (2013).

[33] M. Notomi, A. Shinya, K. Nozaki, T. Tanabe, S. Matsuo, E. Kuramochi, T. Sato, H. Taniyama, and H. Sumikura, "Low-power nanophotonic devices based on photonic crystals towards dense photonic network on chip," IET Circuits Devices Syst. **5**, 84–93 (2011).

[34] A. Yariv and P. Yeh, *Optical waves in crystals : propagation and control of laser radiation* (John Wiley & Sons, 2003).

[35] W. Yoshiki and T. Tanabe, "Analysis of bistable memory in silica toroid microcavity," J. Opt. Soc. Am. B **29**, 3335–3343 (2012).

[36] F. Morichetti, A. Melloni, C. Ferrari, and M. Martinelli, "Error-free continuously-tunable delay at 10 Gbit/s in a reconfigurable on-chip delay-line," Opt. Express **16**, 8395–8405 (2008).

[37] R. W. Boyd, *Nonlinear Optics* (Academic Press, 2008).

[38] M. Pöllinger, "Bottle microresonators for applications in quantum optics and all-optical signal processing," Ph.D. thesis, Johannes Gutenberg-Universit ¨ at Mainz (2010).

[39] P. Barclay, K. Srinivasan, and O. Painter, "Nonlinear response of silicon photonic crystal microresonators excited via an integrated waveguide and fiber taper," Opt. Express **13**, 801–820 (2005).

[40] Q. Xu, S. Manipatruni, B. Schmidt, J. Shakya, and M. Lipson, "12.5 Gbit/s carrier-injection-based silicon micro-ring silicon modulators," Opt. Express **15**, 430–436 (2007).

[41] V. Almeida and M. Lipson, "Optical bistability on a silicon chip," Opt. Lett. **29**, 2387–2389 (2004).

[42] Q. Xu and M. Lipson, "Carrier-induced optical bistability in silicon ring resonators," Opt. Lett. **31**, 341–343 (2006).

[43] F. Xia, L. Sekaric, and Y. Vlasov, "Ultracompact optical buffers on a silicon chip," Nat. Photonics **1**, 65–71 (2007).

[44] Y. Okawachi, K. Saha, J. S. Levy, Y. H. Wen, M. Lipson, and A. L. Gaeta, "Octave-spanning frequency comb generation in a silicon nitride chip," Opt. Lett. **36**, 3398–3400 (2011).

[45] B. B. C. Kyotoku, L. Chen, and M. Lipson, "Sub-nm resolution cavity enhanced microspectrometer," Opt. Express **18**, 102–107 (2010).

[46] B. Schmidt, V. Almeida, C. Manolatou, S. Preble, and M. Lipson, "Nanocavity in a silicon waveguide for ultrasensitive nanoparticle detection," Appl. Phys. Lett. **85**, 4854–4856 (2004).

[47] T. A. Ibrahim, V. Van, and P.-T. Ho, "All-optical time-division demultiplexing and spatial pulse routing with a gaas/algaas microring resonator," Opt. Lett. **27**, 803–805 (2002).

[48] P. Rabiei, W. Steier, C. Zhang, and L. Dalton, "Polymer micro-ring filters and modulators," J. Lightwave Technol. **20**, 1968–1975 (2002).

[49] K. Luke, A. Dutt, C. B. Poitras, and M. Lipson, "Overcoming Si3N4 film stress limitations for high quality factor ring resonators," Opt. Express **21**, 22829–22833 (2013).

[50] V. Almeida, R. Panepucci, and M. Lipson, "Nanotaper for compact mode conversion," Opt. Lett. **28**, 1302–1304 (2003).

[51] T. Shoji, T. Tsuchizawa, T. Watanabe, K. Yamada, and H. Morita, "Low loss mode size converter from 0.3 mu m square Si wire waveguides to singlemode fibres," Electron. Lett. **38**, 1669–1670 (2002).

[52] T. Baba, "Slow light in photonic crystals," Nat. Photonics **2**, 465–473 (2008).

[53] H. Kosaka, T. Kawashima, A. Tomita, M. Notomi, T. Tamamura, T. Sato, and S. Kawakami, "Superprism phenomena in photonic crystals: Toward microscale lightwave circuits," J. Lightwave Technol. **17**, 2032–2038 (1999).

[54] A. Berrier, M. Mulot, M. Swillo, M. Qiu, L. Thylen, A. Talneau, and S. Anand, "Negative refraction at infrared wavelengths in a two-dimensional photonic crystal," Phys. Rev. Lett. **93**, 073902 (2004).

[55] B. Redding, S. F. Liew, R. Sarma, and H. Cao, "Compact spectrometer based on a disordered photonic chip," Nat. Photonics **7**, 746–751 (2013).

[56] A. Badolato, K. Hennessy, M. Atature, J. Dreiser, E. Hu, P. Petroff, and A. Imamoglu, "Deterministic coupling of single quantum dots to single nanocavity modes," Science **308**, 1158–1161 (2005).

[57] A. Oraevsky, "Whispering-gallery waves," Quant. Electron. **32**, 377–400 (2002).

[58] M. Gorodetsky, A. Savchenkov, and V. Ilchenko, "Ultimate Q of optical microsphere resonators," Opt. Lett. **21**, 453–455 (1996).

[59] I. Razdolskiy, S. Berneschi, G. N. Conti, S. Pelli, T. V. Murzina, G. C. Righini, and S. Soria, "Hybrid microspheres for nonlinear Kerr switching devices," Opt. Express **19**, 9523–9528 (2011).

[60] D. Armani, T. Kippenberg, S. Spillane, and K. Vahala, "Ultra-high-Q toroid microcavity on a chip," Nature **421**, 925–928 (2003).

[61] T. Aoki, B. Dayan, E. Wilcut, W. P. Bowen, A. S. Parkins, T. J. Kippenberg, K. J. Vahala, and H. J. Kimble, "Observation of strong coupling between one atom and a monolithic microresonator," Nature **443**, 671–674 (2006).

[62] T. J. Kippenberg and K. J. Vahala, "Cavity optomechanics: Back-action at the mesoscale," Science **321**, 1172–1176 (2008).

[63] T. J. Kippenberg, R. Holzwarth, and S. A. Diddams, "Microresonator-Based Optical Frequency Combs," Science **332**, 555–559 (2011).

[64] A. Armani and K. Vahala, "Heavy water detection using ultra-high-Q microcavities," Opt. Lett. **31**, 1896–1898 (2006).

[65] N. Vukovic, N. Healy, F. H. Suhailin, P. Mehta, T. D. Day, J. V. Badding, and A. C. Peacock, "Ultrafast optical control using the Kerr nonlinearity in hydrogenated amorphous silicon microcylindrical resonators," Sci. Rep. **3**, 2885 (2013).

[66] N. Vukovic, N. Healy, P. Horak, J. R. Sparks, P. J. A. Sazio, J. V. Badding, and A. C. Peacock, "Ultra-smooth microcylindrical resonators fabricated from the silicon optical fiber platform," Appl. Phys. Lett. **99**, 031117 (2011).

[67] J. S. Pelc, K. Rivoire, S. Vo, C. Santori, D. A. Fattal, and R. G. Beausoleil, "Picosecond all-optical switching in hydrogenated amorphous silicon microring resonators," arXiv e-prints p. 1310.5756 (2013).

[68] H. Lee, T. Chen, J. Li, K. Y. Yang, S. Jeon, O. Painter, and K. J. Vahala, "Chemically etched ultrahigh-Q wedge-resonator on a silicon chip," Nat. Photonics **6**, 369–373 (2012).

[69] T. Carmon and K. J. Vahala, "Visible continuous emission from a silica microphotonic device by third-harmonic generation," Nat. Phys. **3**, 430–435 (2007).

[70] X.-F. Jiang, Y.-F. Xiao, Q.-F. Yang, L. Shao, W. R. Clements, and Q. Gong, "Free-space coupled, ultralow-threshold raman lasing from a silica microcavity," Appl. Phys. Lett. **103**, 101102 (2013).

[71] J. Zhu, S. K. Ozdemir, Y.-F. Xiao, L. Li, L. He, D.-R. Chen, and L. Yang, "On-chip single nanoparticle detection and sizing by mode splitting in an ultrahigh-Q microresonator," Nat. Photonics **4**, 46–49 (2010).

[72] A. Harker, S. Mehrabani, and A. M. Armani, "Ultraviolet light detection using an optical microcavity," Opt. Lett. **38**, 3422–3425 (2013).

[73] S. Spillane, T. Kippenberg, O. Painter, and K. Vahala, "Ideality in a fiber-taper-coupled microresonator system for application to cavity quantum electrodynamics," Phys. Rev. Lett. **91**, 043902 (2003).

[74] H. Rokhsari and K. Vahala, "Observation of Kerr nonlinearity in microcavities at room temperature," Opt. Lett. **30**, 427–429 (2005).

[75] M. Yanik, S. Fan, and M. Soljacic, "High-contrast all-optical bistable switching in photonic crystal microcavities," Appl. Phys. Lett. **83**, 2739–2741 (2003).

[76] M. Cai, G. Hunziker, and K. Vahala, "Fiber-optic add-drop device based on a silica microsphere-whispering gallery mode system," IEEE Photonics Technol. Lett. **11**, 686–687 (1999).

[77] F. Monifi, J. Friedlein, S. K. Oezdemir, and L. Yang, "A Robust and Tunable Add-Drop Filter Using Whispering Gallery Mode Microtoroid Resonator," J. Lightwave Technol. **30**, 3306–3315 (2012).

[78] T. J. Kippenberg, "Nonlinear Optics in Ultra-high-Q Whispering-Gallery Optical Microcavities," Ph.D. thesis, California Institute of Technology (2004).

[79] Yariv, *Optical electronics in modern communications* (Oxford University Press, 1997).

[80] E. P. Ostby, "Photonic whispering-gallery resonators in new environments," Ph.D. thesis, California Institute of Technology (2009).

[81] B. Little, J. Laine, and H. Haus, "Analytic theory of coupling from tapered fibers and half-blocks into microsphere resonators," J. Lightwave Technol. **17**, 704–715 (1999).

[82] G. Lin, B. Qian, F. Orucevic, Y. Candela, J. B. Jager, Z. Cai, V. Lefevre-Seguin, and J. Hare, "Excitation mapping of whispering gallery modes in silica microcavities," Opt. Lett. **35**, 583–585 (2010).

[83] J. Knight, G. Cheung, F. Jacques, and T. Birks, "Phase-matched excitation of whispering-gallery-mode resonances by a fiber taper," Opt. Lett. **22**, 1129–1131 (1997).

[84] B. Min, L. Yang, and K. Vahala, "Perturbative analytic theory of an ultrahigh-Q toroidal microcavity," Phys. Rev. A **76**, 013823 (2007).

[85] S. Garth, "Modes on a bent optical wave-guide," IEE Proc J, Optoelectron **134**, 221–229 (1987).

[86] M. Oxborrow, "Traceable 2-D finite-element simulation of the whispering-gallery modes of axisymmetric electromagnetic resonators," IEEE Trans. Microw. Theory Tech. **55**, 1209–1218 (2007).

[87] G. Agrawal, *Nonlinear fibre optics* (Academic Press, 1995).

[88] C. Manolatou, M. Khan, S. Fan, P. Villeneuve, H. Haus, and J. Joannopoulos, "Coupling of modes analysis of resonant channel add-drop filters," IEEE J. Quantum Electron. **35**, 1322–1331 (1999).

[89] H. A. Haus, *Waves and Fields in Optoelectronics* (Prentice Hall, 1984).

[90] B. Little, S. Chu, H. Haus, J. Foresi, and J. Laine, "Microring resonator channel dropping filters," J. Lightwave Technol. **15**, 998–1005 (1997).

[91] T. Kippenberg, S. Spillane, and K. Vahala, "Modal coupling in traveling-wave resonators," Opt. Lett. **27**, 1669–1671 (2002).

[92] M. Soljacic, M. Ibanescu, S. Johnson, Y. Fink, and J. Joannopoulos, "Optimal bistable switching in nonlinear photonic crystals," Phys. Rev. E **66**, 055601 (2002).

[93] M. Cai, O. Painter, and K. Vahala, "Observation of critical coupling in a fiber taper to a silica-microsphere whispering-gallery mode system," Phys. Rev. Lett. **85**, 74–77 (2000).

[94] A. Serpenguzel, S. Arnold, and G. Griffel, "Excitation of resonances of microspheres on an optical-fiber," Opt. Lett. **20**, 654–656 (1995).

[95] N. Dubreuil, J. Knight, D. Leventhal, V. Sandoghdar, J. Hare, and V. Lefevre, "Eroded monomode optical-fiber for whispering-gallery made excitation in fused-silica microspheres," Opt. Lett. **20**, 813–815 (1995).

[96] M. Gorodetsky and V. Ilchenko, "Optical microsphere resonators: optimal coupling to high-Q whispering-gallery modes," J. Opt. Soc. Am. B **16**, 147–154 (1999).

[97] M. Gorodetsky and V. Ilchenko, "High-Q optical whispering-gallery microresonators - precession approach for spherical mode analysis and emission patterns with prism couplers," Opt. Commun. **113**, 133–143 (1994).

[98] T. Aoki, "Fabrication of Ultralow-Loss Tapered Optical Fibers and Microtoroidal Resonators," Jpn. J. Appl. Phys. **49**, 118001 (2010).

[99] M. Borselli, T. J. Johnson, and O. Painter, "Accurate measurement of scattering and absorption loss in microphotonc devices," Opt. Lett. **32**, 2954–2956 (2007).

[100] B. Li, Y. Xiao, C. Zou, X. Jiang, Y. Liu, F. Sun, Y. Li, and Q. Gong, "Experimental controlling of Fano resonance in indirectly coupled whispering-gallery microresonators," Appl. Phys. Lett. **100**, 021116 (2012).

[101] T. Tanabe, M. Notomi, E. Kuramochi, A. Shinya, and H. Taniyama, "Trapping and delaying photons for one nanosecond in an ultrasmall high-Q photonic-crystal nanocavity," Nat. Photonics **1**, 49–52 (2007).

[102] T. Uesugi, B.-S. Song, T. Asano, and S. Noda, "Investigation of optical nonlinearities in an ultra-high-Q Si nanocavity in a two-dimensional photonic crystal slab," Opt. Express **14**, 377–386 (2006).

[103] H. Shanks, P. Sidles, P. Maycock, and G. Danielson, "Thermal conductivity of silicon from 300 to 1400 degrees k," Phys. Rev. **130**, 1743–1748 (1963).

[104] J. F. Shackelford and W. Alexander, eds., *CRC Materials Science and Engineering Handbook* (CRC Press, 2010).

[105] D. Vernooy, V. Ilchenko, H. Mabuchi, E. Streed, and H. Kimble, "High-Q measurements of fused-silica microspheres in the near infrared," Opt. Lett. **23**, 247–249 (1998).

[106] H. Rokhsari, S. Spillane, and K. Vahala, "Loss characterization in microcavities using the thermal bistability effect," Appl. Phys. Lett. **85**, 3029–3031 (2004).

[107] J. B. Jager, V. Calvo, E. Delamadeleine, E. Hadji, P. Noe, T. Ricart, D. Bucci, and A. Morand, "High-Q silica microcavities on a chip: From microtoroid to microsphere," Appl. Phys. Lett. **99**, 181123 (2011).

[108] T. Carmon, H. Rokhsari, L. Yang, T. Kippenberg, and K. Vahala, "Temporal behavior of radiation-pressure-induced vibrations of an optical microcavity phonon mode," Phys. Rev. Lett. **94**, 223902 (2005).

[109] M. Oxborrow, "Ex-house 2D finite-element simulation of the whispering-gallery modes of arbitrarily shaped axisymmetric electromagnetic resonators," arXiv e-prints (2006).

[110] P. Barclay, K. Srinivasan, M. Borselli, and O. Painter, "Probing the dispersive and spatial properties of photonic crystal waveguides via highly efficient coupling from fiber tapers," Appl. Phys. Lett. **85**, 4–6 (2004).

[111] H. Gibbs, F. Hopf, D. Kaplan, and R. Shoemaker, "Observation of chaos in optical bistability," Phys. Rev. Lett. **46**, 474–477 (1981).

[112] T. J. Kippenberg and K. J. Vahala, "Cavity opto-mechanics," Opt. Express **15**, 17172–17205 (2007).

[113] T. Kippenberg, H. Rokhsari, T. Carmon, A. Scherer, and K. Vahala, "Analysis of radiation-pressure induced mechanical oscillation of an optical microcavity," Phys. Rev. Lett. **95**, 033901 (2005).

[114] T. Carmon, M. C. Cross, and K. J. Vahala, "Chaotic quivering of micron-scaled on-chip resonators excited by centrifugal optical pressure," Phys. Rev. Lett. **98**, 167203 (2007).